Orbit Correction and Response Analysis at DELTA

Stephan-Robert Kötter

2022

Dissertation
zur Erlangung des Grades
Doktor der Naturwissenschaften

Fakultät Physik
Technische Universität Dortmund

Datum der Prüfung: 12.12.2022

Vorsitzender der Kommission: Prof. Dr. Cristoph Lange

Erstgutachter: Prof. Dr. Shaukat Khan

Zweitgutachter: Prof. Dr. Andreas Jankowiak

weiteres Mitglied der Kommission: Dr. Jörg Debus

Abstract

The DELTA facility is a synchrotron light source located in Dortmund, Germany. Here, the TU Dortmund University operates a 1.5 GeV storage ring supplying radiation ranging from the THz to the hard X-ray regime for experiments in chemistry, biochemistry, solid-state physics and materials science. The ring is equipped with a slow orbit feedback (SOFB) that corrects the transverse orbit position using a set of steerer magnets. The orbit correction software acts as the feedback's controller. Until 2021, the ring used a program based on a customized singular value decomposition (SVD) approach for calculating corrections. Its replacement, which is better integrated into the experimental physics and industrial control system (EPICS) and also capable of two methods of energy correction, was implemented and commissioned to routine operation within the scope of this work. Additionally, the closed-orbit bilinear-exponential analysis (COBEA) algorithm was generalized to accept combinations of orbit response matrix columns, so-called response sets, as input. This enables the new response set fit algorithm (RSFA) to extract the coupled beta functions and betatron phase advances as well as the scaled dispersion from orbit corrections. If it is integrated with the SOFB in an online fitting approach, the RSFA will supply non-invasive measurements of these optical functions. The new orbit correction software and algorithm are described and evaluated in simulations as well as experimental studies.

Kurzfassung

DELTA ist eine Synchrotronstrahlungsquelle in Dortmund, Deutschland. Hier betreibt die Technische Universität Dortmund einen 1.5 GeV-Elektronenspeicherring, der Strahlung vom THz- bis zum harten Röntgenbereich für Experimente in der Chemie, der Biochemie, der Festkörperphysik sowie den Materialwissenschaften zur Verfügung stellt. Der Ring ist mit einer langsamen Orbitkorrektur ausgestattet, um die transversale Orbitposition mit Hilfe von Steuermagneten zu korrigieren. Die Regelung wird durch das Orbitkorrekturprogramm gesteuert. Bis ins Jahr 2021 wurde ein auf der Methode der Singulärwertzerlegung (SVD) beruhender und auf DELTA angepasster Ansatz verwendet, um diese Korrekturen zu berechnen. Im Rahmen dieser Arbeit wurde ein neues Programm implementiert und in den Routinebetrieb übernommen, das besser in das *Experimental Physics and Industrial Control System* (EPICS) integriert ist und zwei Methoden zur Energiekorrektur bereitstellt. Zusätzlich wurde der *Closed-Orbit Bilinear-Exponential Analysis*-Algorithmus (COBEA-Algorithmus) verallgemeinert, um Linearkombinationen von Orbitkorrekturmatrizen, genannt *Response Sets*, als Eingangsdaten zu akzeptieren. Das ermöglicht dem neuen *Reponse Set Fit Algorithm* (RSFA) die gekoppelten Betafunktionen und Betatronphasenvorschübe sowie die skalierte Dispersion aus einem Satz Orbitkorrekturdaten zu extrahieren. Würde der Algorithmus mit der langsamen Orbitkorrektur in einem Online-Fitansatz integriert, könnten nicht-invasive Messungen der genannten optischen Funktionen durchgeführt werden. Das neue Orbitkorrekturprogramm und der RSFA werden beschrieben und aufgrund von Simulationen sowie experimenteller Studien evaluiert.

CONTENTS

Contents

1 INTRODUCTION

In 1946, a group of scientists observed a phenomenon [1] that had been theorized to exist since 1894 [2] following decades of research into J. C. Maxwell's theory of dynamical electromagnetism [3]: charged particles emit electromagnetic radiation when being deflected by the Lorentz force. The researchers had accelerated electrons in a particle accelerator, a 70 MeV synchrotron, in the labs of General Electric in Schenectady, New York. The radiation was consequently dubbed synchrotron radiation. It is characterized by a broad spectrum whose median energy is determined by the strength of the magnetic field and the energy of the particle beam [4], quantities which are exploitable for building potent sources of X-rays, a matter-penetrating electromagnetic radiation discovered by W. C. Röntgen in 1895 [5], useful for conducting experiments in various sciences. Today, many particle accelerators exist for the sole purpose of providing synchrotron radiation and assist in advancing humanity's understanding of matter on a microscopic scale. These synchrotron radiation facilities are based on energy-efficient electron storage rings which keep the beam on a closed orbit.

The electron beam in a typical GeV-range storage ring delivers kilowatts of power posing a problem for the safety of the machine if the beam drifts too far from its designated position. The vacuum chamber can then take damage from synchrotron radiation hitting uncooled surfaces. Other undesirable outcomes are drifts of beamline source points, reductions of the beam lifetime and beam losses. All impair ongoing experiments and the latter two also present possible radiation hazards. At most storage rings, orbit drifts are therefore suppressed by automated slow orbit feedbacks (SOFBs) [6] that are additionally useful for active orbit placement. They control small dipole magnets, called steerer magnets, to steer the orbit towards an orbit reference.

The electrons in a storage ring perform betatron oscillations around the closed orbit that are characterized by an amplitude and a phase function, referred to as the beta(tron) function and the betatron phase (function) [7], both named after the accelerator at which they were first discovered, the betatron [8]. In modern synchrotrons and storage rings, betatron oscillations are shaped via alternating gradient (AG) focusing that combines horizontally focusing and defocusing quadrupoles to achieve a net focusing effect in both planes [9]. AG focusing is useful to decrease the beam size and thereby increase the brilliance. The beta function and betatron phase are properties of the lattice, the sequence of the storage ring's dipole, quadrupole and higher-order magnets, and the modeling and measurement of these optical functions plays an important role in the operation and the design of synchrotron light sources.

The DELTA facility is a synchrotron radiation source operated by the TU Dortmund University in Germany. The facility's 1.5-GeV electron storage ring produces radiation ranging

from the THz to the hard-X-ray regime for international experiments in solid-state physics, chemistry, biochemistry and materials science. It is equipped with three insertion devices, a 7 T superconducting wiggler (SCW) [10] and two undulators [11]. The SOFB of the storage ring operates with 30 horizontal, 26 vertical steerer magnets and 54 beam position monitors (BPMs). Its controller is a singular-value-decomposition (SVD) based orbit correction software, which was commissioned in 2004 [12]. Optics analysis at the ring is done with a range of numerical models and measurement techniques. In 2016, the closed-orbit bilinear-exponential analysis (COBEA) algorithm became the newest entry to this list [13]. It fits the bilinear-exponential (BE) model to a measured orbit response matrix (ORM) decomposing it into coupled beta functions, betatron phase advances and scaled dispersion functions. COBEA was experimentally tested at three storage rings without transverse coupling (MLS, BESSY II and DELTA).

The goals of this work were to

- write a new orbit correction software that better integrates into the operating system of the storage ring at DELTA and adds new functionality,

- investigate embedding the BE model into an online fitting process fed with orbit response data from orbit corrections (BE online model) that will enable a measurement of optical functions without dedicated ORM measurement and

- test COBEA's approach of reconstructing optical functions for storage ring lattices with transverse coupling.

Chapter 2 introduces basic theoretical concepts of storage ring beam dynamics as well as the DELTA facility and hardware components of its storage ring. The following Ch. 3 outlines more advanced aspects of the linear theory of beam dynamics including transverse coupling that are necessary to understand this work. Chapter 4 explains important concepts of orbit correction in general and orbit correction methods used specifically at DELTA. The 5th Ch. outlines the approach of the new orbit correction software implemented to meet the first goal of this work. The new software features a mode for pure orbit correction and two modes for additional energy correction, one stabilizing the beam energy and one minimizing the orbit length for a given orbit reference. Chapter 6 presents a simulation-based proof of principle for the orbit-shortening mode. In Ch. 7, experimental results for all three modes are presented. The 8th Ch. explains the COBEA algorithm and Ch. 9 introduces a generalization, the response set fit algorithm (RSFA), meant for use in a BE online model, the second goal of this work. Focusing on the third goal of this work, Ch. 10 studies the capabilities of COBEA and the RSFA to extract optics information from simulated orbit response data in the presence of transverse coupling. In Ch. 11, a comparison of experimental RSFA results to other sources of optical function measurements as well as an RSFA-based analysis of the new superconducting wiggler on the optics of the storage ring are presented. The concluding Ch. 12 summarizes this work and gives an outlook.

2 Basic Concepts

2.1 Particle Motion in a Storage Ring

A storage ring confines moving charged particles by means of the Lorentz force. In linear beam dynamics, their trajectories can be described as betatron oscillations around a closed orbit. The closed orbit is the only trajectory that closes after a single turn. Its location is subject to change during operation. It is practical to describe all trajectories, be they betatron oscillations or closed orbits, relative to a moving frame of reference, the co-moving coordinate system [14] (see left schematic in Fig. 2.1). Its origin moves along the storage ring as an ideal particle would: with nominal energy on an ideal closed orbit. In most storage ring designs, the location of this orbit, the design orbit, is determined by the bending radii of the dipoles and the magnetic centers of most quadrupoles. The position of the coordinate frame along the design orbit is determined by a longitudinal coordinate s that increases from zero up to the length of the storage ring.
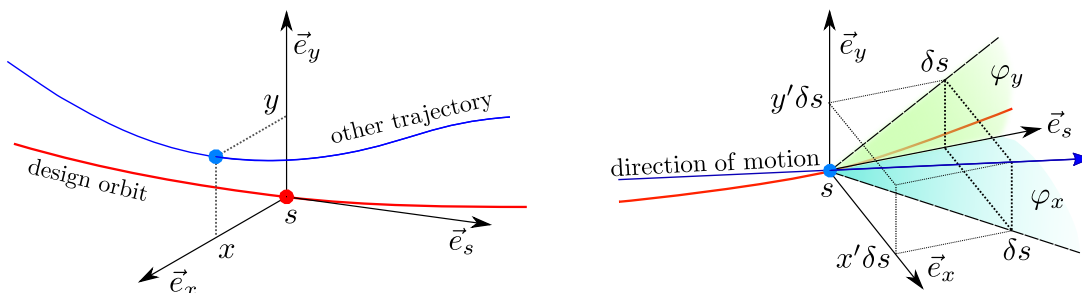
Figure 2.1: Position of a particle in the co-moving coordinate system (left) as well as relation of angles and transverse coordinate derivatives with respect to s (right). In the right schematic, the motion direction is a tangent to the real trajectory and δs is a small step in the direction of $\vec{e}_s$.

The position of a particle within the moving coordinate system is described by a horizontal coordinate x and a vertical coordinate y. The unit vectors of the horizontal coordinate $\vec{e}_x$ and the vertical coordinate $\vec{e}_y$ are perpendicular to the ideal particle's direction of motion $\vec{e}_s$ that itself is a tangent to the design orbit. Describing the complete motion state of a particle with relativistic mass m within the co-moving coordinate system requires three additional coordinates, the relativistic momenta $p_x = m\dot{x}$, $p_y = m\dot{y}$ and $p_s = m\dot{s}$. Together with the spatial coordinates, they determine the position of a particle in 6D phase space. In a synchrotron radiation source such as DELTA, the particles in the storage ring are electrons

and they move at velocities v close to the speed of light c. This is marked by the large Lorentz factor of the storage ring

$$\gamma = \frac{1}{\sqrt{1 - \frac{v^2}{c^2}}} \approx 3000. \tag{2.1}$$

In ultra-relativistic approximation $\dot{z} \approx c$ and under neglect of synchrotron radiation, the transverse momenta are approximately proportional to the derivatives of the transverse coordinates with respect to s

$$x' = \frac{\partial x}{\partial s} = \frac{\partial x}{\partial t}\frac{\partial t}{\partial s} \approx \frac{p_x}{mc} \qquad \text{and} \qquad y' = \frac{\partial y}{\partial s} = \frac{\partial y}{\partial t}\frac{\partial t}{\partial s} \approx \frac{p_y}{mc}. \tag{2.2}$$

The transverse phase space of a particle is therefore described by

$$\vec{z}^T = \left(x, x', y, y'\right)^T. \tag{2.3}$$

In a storage ring, the longitudinal momentum of a particle is many times larger than its transverse momenta. The possible angles are therefore in the mrad-range and the derivatives of the spatial coordinates can be interpreted as angles (see right schematic in Fig. 2.1)

$$\varphi_x \approx \tan(\varphi_x) = \frac{x'\delta s}{\delta s} = x' \qquad \text{and} \qquad \varphi_y \approx \tan(\varphi_y) = \frac{y'\delta s}{\delta s} = y'. \tag{2.4}$$

2.1.1 Betatron Oscillations

Keeping charged particles in a storage ring together, requires a focusing system. In modern storage rings, this role is commonly fulfilled by quadrupole magnets. Quadrupoles provide a magnetic flux density that increases proportional to the distance from the magnetic center of the magnet. While the design orbit passes the magnet at the center, all other trajectories pass it off-center. Particles on these trajectories are either bent towards the design orbit (focused) or bend away from it (defocused). The bending angle increases along the magnetic field strength with the distance from the magnetic center. A QF quadrupole, which focuses in the horizontal plane, defocuses in the vertical plane. For a QD quadrupole, it is the other way around. To achieve a net focusing effect, QF quadrupoles with positive horizontal gradient and QD quadrupoles with negative horizontal gradient can be combined. This is known as alternating gradient (AG) focusing and was proposed at the Brookhaven National Laboratory in 1952 [9]. Figure 2.2 displays a schematic of the focusing process in a quadrupole duplet.

In modern storage rings, the AG focusing as well as minor contributors such as weak focusing in sector-type dipoles and magnet fringe fields let particles, which are not on the design orbit, perform betatron oscillations around it [16]. An early comprehensive parameterization of betatron oscillations in AG synchrotrons is given in [7]. It is known as the Courant-Snyder
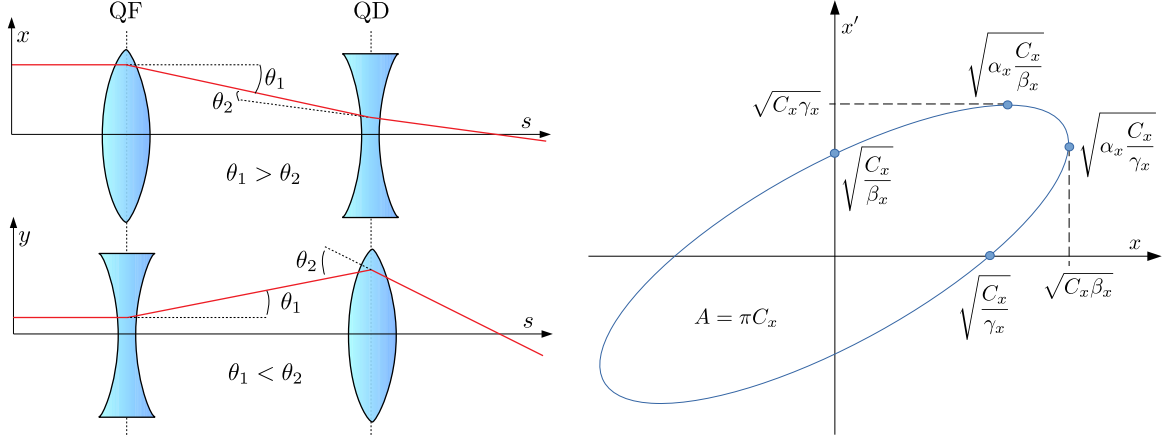
Figure 2.2: Focusing effect of a quadrupole duplet in both transverse planes [15] (left) and the phase space ellipse of a betatron oscillation [14] (right).

parameterization. Here, betatron oscillations refer to oscillations of the spatial coordinate and its longitudinal derivative [14]

$$x(s) = \sqrt{C_x \beta_x(s)} \cos\left(\Phi_x(s) + \Phi_x^{\text{init}}\right) \tag{2.5}$$

$$x'(s) = \sqrt{\frac{C_x}{\beta_x(s)}} \left[\alpha_x(s) \cos\left(\Phi_x(s) + \Phi_x^{\text{init}}\right) + \sin\left(\Phi_x(s) + \Phi_x^{\text{init}}\right)\right]. \tag{2.6}$$

The amplitude of the spatial oscillation is determined by a particle-specific constant C_x, the Courant-Snyder invariant, and the beta function $\beta_x(s)$ that is the same for all particles. The oscillation phase similarly consists of a particle-specific start phase Φ_x^{init} as well as a function part $\Phi_x(s)$, the betatron phase advance. The latter is the same for all particles. Both, beta function and betatron phase advance are properties of the lattice. The same applies to the alpha function that is the negative half-derivative of the beta function

$$\alpha_x(s) = -\frac{\beta_x'}{2}. \tag{2.7}$$

While the beta function is periodic with the length of the storage ring, the betatron phase advance is not. Particles enter each additional turn with a phase offset

$$\mu_x = \Phi_x(L) - \Phi_x(0) = 2\pi q_x, \tag{2.8}$$

where q_x is the tune. The trajectory of a betatron oscillation therefore changes from turn to turn moving the particle along a transverse phase space ellipse shown in Fig. 2.2. Similar to the spatial oscillation, the amplitude of the momentum oscillation $\sqrt{C_x \gamma_x(s)}$ is determined by the particle-specific Courant-Snyder invariant and a general part

$$\gamma_x(s) = \frac{\alpha_x^2(s) + 1}{\beta_x(s)}, \tag{2.9}$$

13

the gamma function. The Courant-Snyder invariant is related to the area of the ellipse $A = \pi C_x$. The phase space ellipses of all particles are concentric. For a gaussian transverse beam profile, the Courant-Snyder invariant of the particle whose spatial betatron oscillation amplitude matches the standard deviation of the beam profile is called emittance [14]. The same relations hold for the vertical plane.

The Courant-Snyder parameterization of betatron oscillations is an approximation for storage rings with little to no inter-plane coupling. The betatron oscillations of the horizontal and vertical plane then do not mix. This holds true for most storage rings in good approximation. A more general description of transversly coupled betatron oscillations is introduced in Ch. 3.1.

2.1.2 RF Frequency, Beam Energy and Dispersion

Charged particles emit synchrotron radiation when interacting with the electromagnetic fields of the storage ring via the Lorentz force [14]. The emitted photons carry some of the kinetic energy of the particles away. It is necessary to reaccelerate these particles. Otherwise they are lost. The acceleration is applied in a radiofrequency (RF) resonator containing an oscillating electric field with a longitudinal field-strength component E. The RF frequency of the resonator needs to be an integer multiple of the revolution frequency of the ideal particle to make it arrive at the same phase, the synchronous phase, and the same electric field strength E_0 every turn.
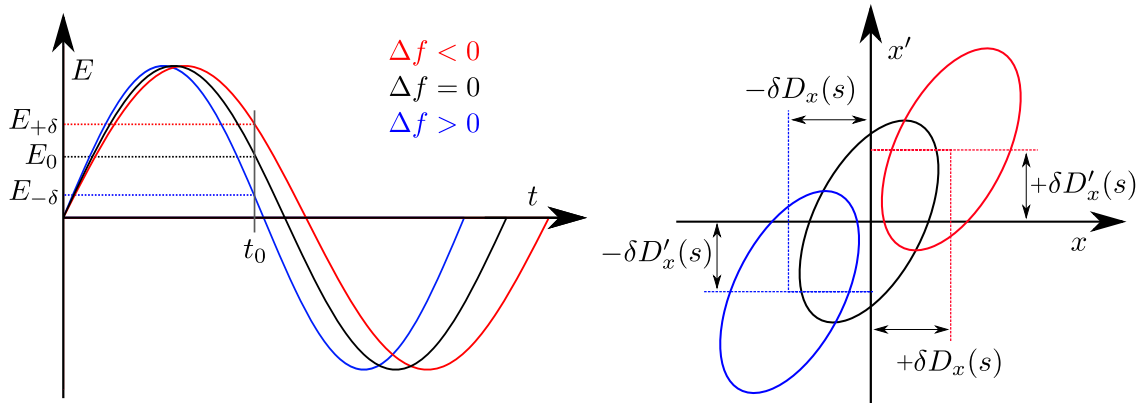
Figure 2.3: How a frequency shift alters the acceleration voltage experienced by the beam in the RF resonator (left) and the impact of the resulting energy shift on the position of betatron oscillations in transverse phase space in areas where dispersion is positive (right). The arrival time t_0 of the beam in the cavity is determined by the synchronous phase.

Beyond recovering the energy loss resulting from synchrotron radiation, the RF resonator is useful for adjusting the energy of the closed orbit, the beam energy, by altering the RF frequency. If the RF frequency f changes by Δf, the beam experiences a different electric field amplitude when passing the cavity the next time. A schematic of this is shown on the left in Fig. 2.3. An effect called phase focusing then makes the beam oscillate around a slightly different synchronous phase in subsequent turns. Here, it eventually comes to rest due to

synchrotron radiation damping. In this new equilibrium state, the beam energy has changed by δ. The relation of frequency shift and energy shift is [17]

$$\frac{f}{f + \Delta f} - 1 = \left(\alpha - \frac{1}{\gamma^2} \right) \delta \approx \alpha \delta, \qquad (2.10)$$

where the momentum compaction factor [14]

$$\alpha = \frac{\Delta L / L}{\delta} \qquad (2.11)$$

determines the orbit lengthing ΔL for particles deviating form the design energy relative to the length of the design orbit L. It is a property of the lattice. At DELTA, the $1/\gamma^2$-term can be neglected due to $\alpha >> 1/\gamma^2$ (see Tab. 2.1 and Eq. (2.1)). The orbit length is affected because the bending radii of the dipole magnets are dependent on the beam energy. The energy shift therefore pushes the beam to a new orbit where the revolution frequency is again an integer multiple of the RF frequency. The difference between the original and the new transverse orbit is $\delta D_x(s)$, where $D_x(s)$ is the horizontal dispersion function. Its longitudinal derivative $D_x'(s)$ similarly describes the change in transverse momenta via $\delta D_x'(s)$. With the closed orbit, the betatron oscillations are shifted, as well. A schematic of the effect is shown on the right in Fig. 2.3. The dispersion function is, similar to the beta function and the betatron phase advance, a property of the lattice. It is determined by the bending magnets of a storage ring and is therefore largely confined to the horizontal plane. If vertical dispersion is present, the same relations apply.

2.2 THE STORAGE RING AT DELTA

The Dortmund Elektronenspeicherring-Anlage (DELTA) is a combined synchrotron radiation source and accelerator research facility located in Dortmund, Germany. It is operated by the Center for Synchrotron Radiation of the TU Dortmund University. A schematic top-up view of the storage ring at DELTA and its injection chain is given in Fig. 2.4.

The electrons are emitted in a triode gun with 50 kV extraction voltage after which they pass a 3-cell $2\pi/3$-mode standing-wave buncher with a design gradient of 16 MV/m [19]. Both components are followed by a 6 m S-band linear accelerator that increases the electron energy to 75 MeV [20]. The transfer line T1 connects the linac exit to the booster synchrotron BoDo. BoDo is a 50.4 m long full-energy booster. Its magnet power supplies are current controlled and ramped via digital signal processors following programmable power arcs. BoDo can therefore be operated like a storage ring at constant energy ranging from 50 MeV to 1.50 GeV. In booster operation, the transfer line T2 transports the electrons to the injection septum of the storage ring.

The 115.2 m storage ring entered commissioning in 1996. Similar to BoDo, it can be ramped and operated at different energies. The maximum energy is 1.5 GeV. A summary of important parameters is given in Tab. 2.1. The layout of the storage ring, two 42.6 m half-circles con-
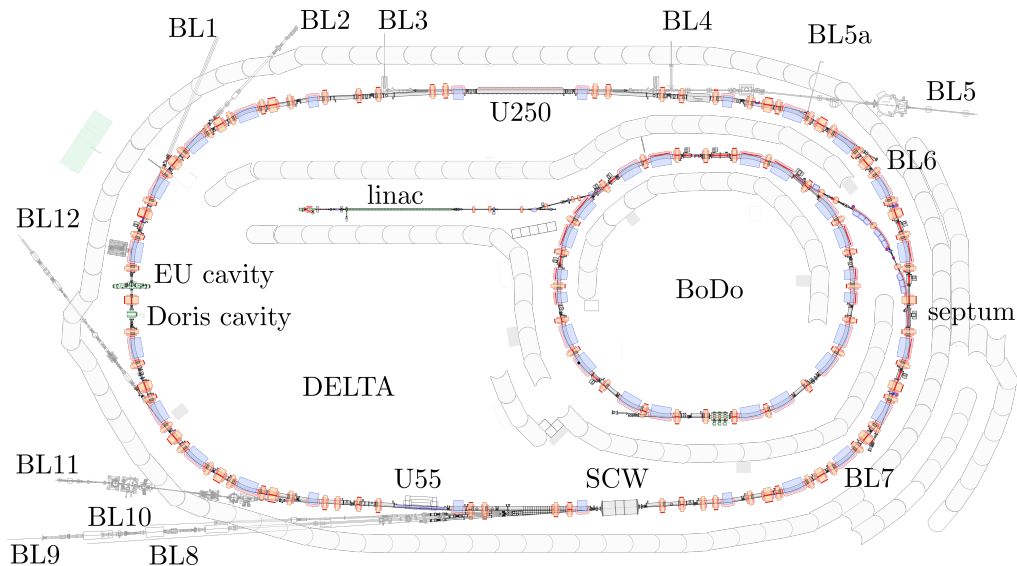
Figure 2.4: The accelerator complex at DELTA. Source: adapted from technical drawing [18].

nected by two 15 m straight sections for operation of insertion devices, reminds of a racetrack. The design achieves a horizontal emittance of 15 nm rad while still being compact [22]. The T2 connects to the storage ring half-way through the eastern arc. The two RF cavities of the ring are located on the opposite side. The first resonator, a DORIS-type cavity, is fed with up to 65 kW of forward power from a klystron. The second resonator, an EU-type cavity [23] fed with up to 75 kW of forward power from a solid state amplifier, was added in 2019 to prepare for the installation of the superconducting wiggler (SCW) [24].

The storage ring supplies synchrotron radiation ranging from the THz to the hard X-ray regime to several beamlines used for experiments in solid-state physics, chemistry, biochemistry and materials science. The northern straight section was initially designed to accommodate the low-gain free electron laser experiment FELICITA [25], an optical klystron. Since 2011 it has been replaced with the DELTA short pulse facility, a coherent harmonic generation (CHG) experiment using the U250 undulator [26]. The experiment produces coherent synchrotron radiation with pulse lengths in the femtosecond range at harmonics of a 800 nm titan-sapphire seeding laser for BL5 [27]. So far, this approach was demonstrated to work down to a wavelength of 133 nm, the 3rd harmonic of the frequency-doubled seeding laser. In the future, the CHG experiment will be replaced with a setup enabling echo-enabled harmonic generation (EEHG) to reach even smaller wavelengths [28]. The CHG setup is also used as part of a tunable narrow-bandwidth THz source [29]. The THz radiation is emitted in one of the dipoles following the U250 (BL5a). In the southern straight section, a wiggler and an undulator are installed. The SCW [10], a 7-T wiggler, supplies hard X-ray radiation of up to 30 keV to BL8, BL9 and BL10. In 2020, it replaced a 5-T wiggler, the superconducting asymmetric wiggler (SAW), which produced up to 10 keV X-rays [30]. The permanent-magnet undulator U55 produces radiation ranging from the vacuum UV spectrum to soft X-rays for BL11. The remaining beamlines are fed with synchrotron radiation from dipole magnets.

parameter	value
nominal beam energy	1.5 GeV
RF frequency f	499.834 MHz
ring length L	115.2 m
harmonic number	192
revolution frequency	2.603 MHz
revolution time	384 ns
bunch length (FWHM)	75 ps
horizontal emittance	15 nm rad
momentum compaction factor α	$5 \cdot 10^{-3}$
number of BPMs J	54
number of horizontal steerer magnets K_x	30
number of vertical steerer magnets K_y	26

Table 2.1: Parameters of the storage ring before installation of the SCW in 2020. Source: technical report [21].

Most hardware components are controlled via a distributed control system, the experimental physics and industrial control system (`EPICS`) [31]. It provides a software architecture to read out and set hardware parameters via Ethernet.
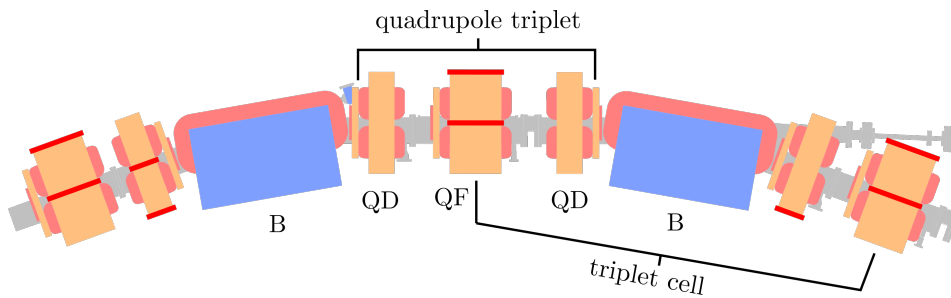
Figure 2.5: Quadrupole triplet and triplet cell after the northern straight. Source: adapted from technical drawing [18].

2.2.1 LATTICE

The lattice of the storage ring was initially designed in 1989 [32]. In 1999, the optics was modified to prepare for the installation of the SAW and the U55 [33]. Since then, the optics largely remained the same although the current optics includes minor changes such as altered quadrupole strengths resulting from modifications of the storage ring's nominal tunes and optics adaptions for the SCW. A plot of the optical functions according to the *del008.2001* (see Ch. 2.4 for model details) is given in Fig. 2.6.

The storage ring lattice is designed around the triplet cell, a bending magnet enclosed by alternating gradient lenses. This way, the horizontal dispersion rising in the dipoles is suppressed in the focusing quadrupoles whereby the horizontal emittance is kept small. The term triplet structure comes from the arrangement of the quadrupoles. Because the focusing quadrupoles
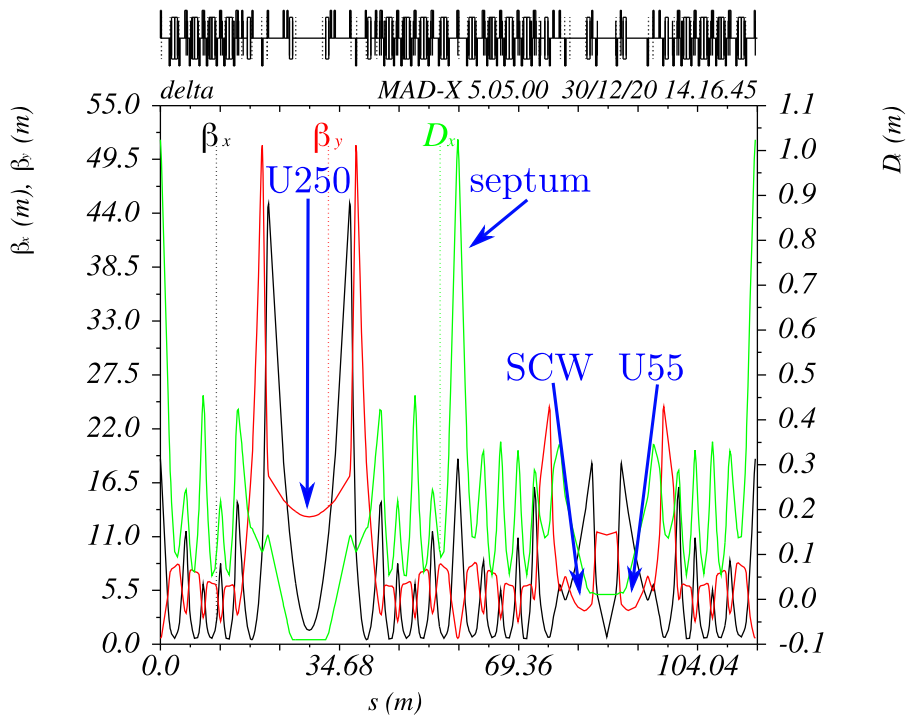
Figure 2.6: Optical functions of the storage ring in user operation but with turned-off SAW according to the *del008.2001* model [33][34].

of two adjacent cells are combined into a single quadrupole of double width, the space between bends is technically occupied by three quadrupoles, a triplet (see Fig. 2.5).

The injection area in the eastern arc accommodates the injection septum. For injection, the beam is brought close to the septum via a kicker bump to establish an overlap between the phase space ellipse of the injected beam and the phase space acceptance of the storage ring. The dispersion peak in that area is a drawback of the lattice design as it pushes off-energy particles coming from the booster onto a dispersive orbit. The other large dispersion peak on the opposite side of the storage ring, in the RF resonators, is another drawback as it leads to a coupling of synchrotron and betatron oscillations. The decision to built the storage ring this way was made because it allowed enlarging the straights in the north and south making room for the operation of insertion devices [34].

Matching quadrupoles decouple the optics of the straight sections from the optics of the arcs. The optics design of the southern straight is a trade-off between the requirement of a small vertical beta function in the SAW and a beam with small divergence in the U55. A small vertical beta function in the SAW ensures small betatron oscillation amplitudes fitting into the wiggler. Its 10 mm aperture is only a quarter of the aperture in the remaining storage ring. The small vertical beta function also minimizes the wiggler's unwanted edge focusing effect on the vertical tune. A small beta function comes with a large divergence. This is undesirable for the operation of the U55, which is installed in the second half of the southern

straight, as a large divergence makes any off-axis electrons pass the undulator at a large angle. The synchrotron light emitted by these electrons is red-shifted for the on-axis observer. This increases the spectral width of the undulator radiation. The U55 is therefore best operated with a large beta function that does not change much along the length of the insertion device. The optics design of the northern straight predates the commissioning of the CHG experiment and concentrated on providing a suitable environment for its predecessor, the FELICITA optical klystron. Similar to the U55, the undulator-based FELICITA experiment was best operated with a beam with small divergence. Additionally, the experiment required a small dispersion function. Both design specifications also work well for the CHG experiment installed in the northern straight today.

2.2.2 Beam Position Monitors

DELTA is equipped with $J = 54$ beam position monitors (BPMs) that measure the transverse position of the beam's center. Fig.2.7 displays an overview of the storage ring where the location of the BPMs are marked. The horizontal and vertical measurements of the BPMs

$$\vec{x} = \Big(x_1, \, \dots, \, x_J \Big)^T \tag{2.12}$$

and

$$\vec{y} = \Big(y_1, \, \dots, \, y_J \Big)^T \tag{2.13}$$

are available via `EPICS` with a rate of about 10 Hz mostly determined by Ethernet latency. Each BPM consists of a quartet of capacitive pick-up electrodes paired with read-out electronics. The electrodes are inlets built into the vacuum chamber. Most BPMs use the geometry displayed in Fig. 2.8 [36]. The exceptions are BPMs 40 and 41 that are built into the tapers of the vacuum chamber of the superconducting wiggler (SCW).

The voltages U_i of the pick-ups are pairwise subtracted to reveal the horizontal position [37]

$$x = c_x(x, \, y) \frac{(U_2 + U_4) - (U_1 + U_3)}{\sum_{i=1}^4 U_i} \tag{2.14}$$

and the vertical position

$$y = c_y(x, \, y) \frac{(U_1 + U_2) - (U_3 + U_4)}{\sum_{i=1}^4 U_i} \tag{2.15}$$

of the beam. The calibration factors $c_x(x, \, y)$ and $c_y(x, \, y)$ are non-linear and geometry-specific. They were determined via a simulation of the electric field in the DELTA BPM. The equation system consisting of equations (2.14) and (2.15) has to be solved for x and y to determine the correct orbit position. If the orbit does not deviate too far from the center of the BPM, the calibration factors can be considered constant in good approximation. They are $c_x^{\text{SCW}} = 10.4\,\text{mm}$ and $c_y^{\text{SCW}} = 23.9\,\text{mm}$ for the two BPMs with different geometry around the SCW
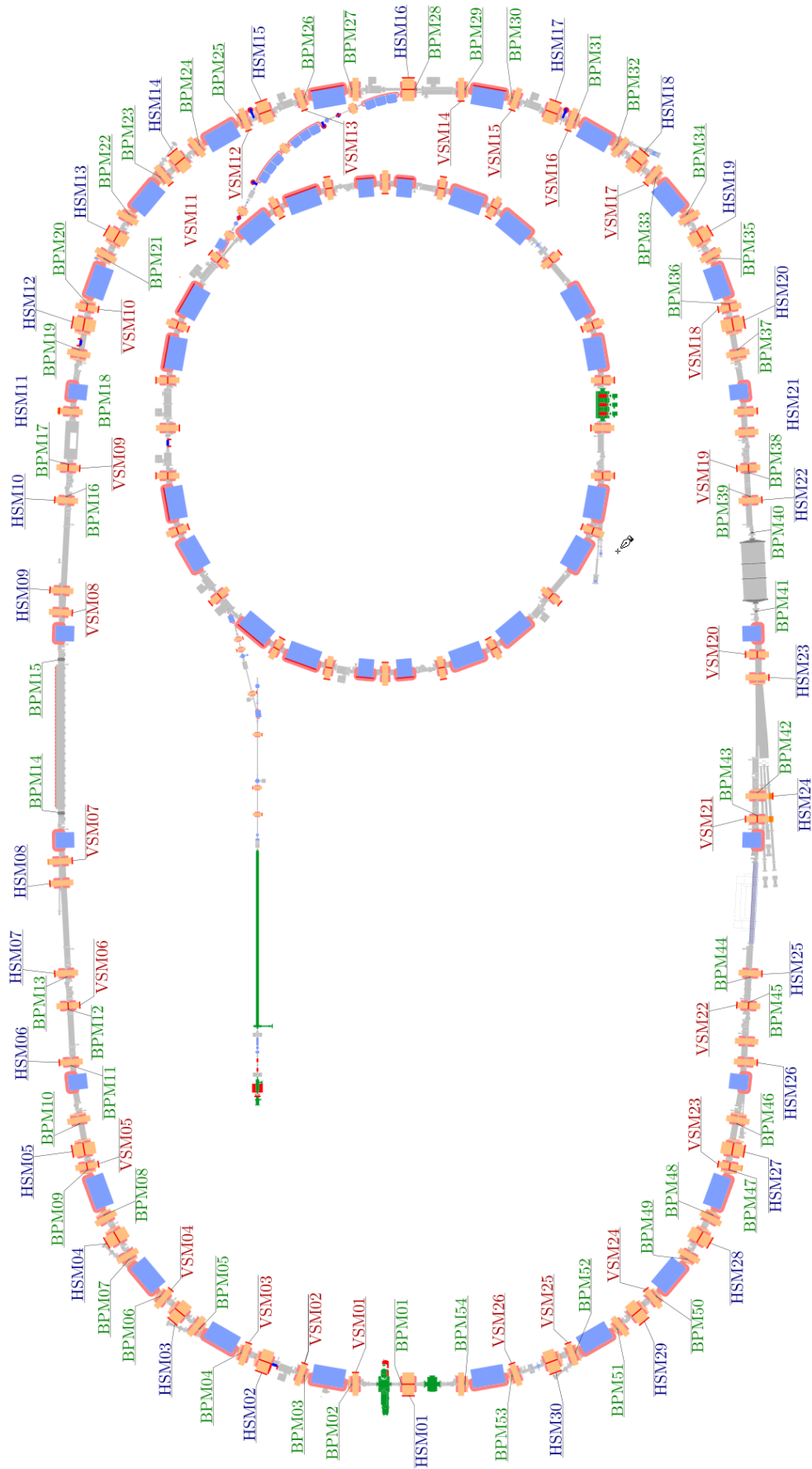
Figure 2.7: Positions of BPMs (see Ch. 2.2.2) as well as the horizontal and vertical steerer magnets (HSM and VSM) (see Ch. 2.2.3) along the storage ring. Source: adapted from technical drawing [18].
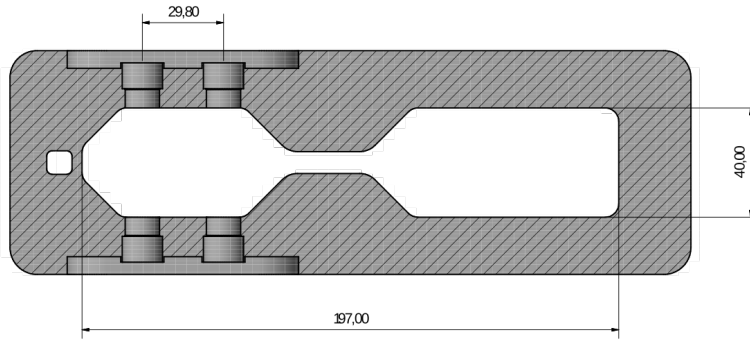
Figure 2.8: Cross section of typical BPM electrode inlets in a vaccum chamber used at DELTA. Source: adapted from technical drawing [35].

[38] and $c_x = 15.9\,\text{mm}$ and $c_y = 19.6\,\text{mm}$ everywhere else. All orbit measurements available via `EPICS` are calculated with constant calibration factors. Fig. 2.9 displays the evolution of the systematic error when measuring off-center for the standard geometry. The orbit position is calculated by the read-out electronics of each BPM. Two different read-out electronics are used at DELTA.

44 BPMs are equipped with Bergoz MX BPMs [39]. This read-out electronics generates an analogous signal of $\pm 10\,\text{V}$ equivalent to $\pm 10\,\text{mm}$ orbit displacement that is digitized by an ESD Module [40] for up to 4 Bergoz units and then fed into `EPICS` via a CAN (controller area network) field bus to a central processor unit (CPU) sitting on a VME (versa module eurocard) crate [36]. The analog-digital converter (ADC) feature a resolution of 12 bit including 1 sign bit resulting in a $4.8\,\mu\text{m}$ resolution for orbit measurements.
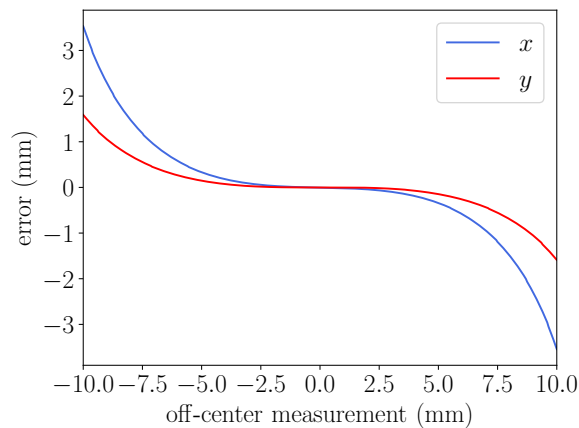
Figure 2.9: Systematic error of off-center orbit measurement in a BPM with constant calibration factors.

10 BPMs are equipped with Libera Electron processors [41]. This FPGA-based measurement electronics filters the voltage signal induced on the BPM pick-ups by the beam with a bandpass of $10\,\text{MHz}$ around the RF frequency of DELTA and then undersamples the filtered signal within a rate of about $117\,\text{MHz}$ [41]. The time series is averaged down to supply on-demand orbit measurements at turn-by-turn rate of $2.6\,\text{MHz}$ and continuous orbit measurements at $10\,\text{kHz}$
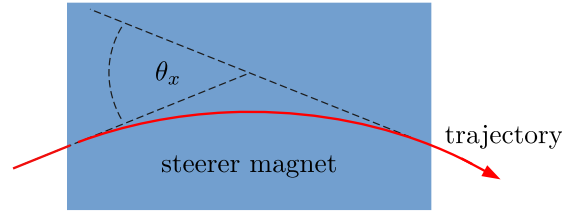
Figure 2.10: Schematic of a kick in a steerer magnet.

for a fast orbit feedback and $10\,\text{Hz}$ for closed orbit measurements. At DELTA, the triggers of the turn-by-turn measurements are synchronized with the kicker of the tune measurement system (see Ch. 2.2.4 for details). Each Libera runs a Linux kernel and broadcasts buffers of measurements at turn-by-turn rate and continuous closed-orbit measurements to `EPICS` via Ethernet. The averaging process allows Libera Electrons to achieve a resolution of $<1\,\mu\text{m}$ for the closed-orbit measurements [42].

2.2.3 STEERER MAGNETS

The storage ring is equipped with $K_x = 30$ horizontal steerer magnets (HSMs) and $K_v = 26$ vertical steerer magnets (VSMs) [36]. Figure 2.7 displays a top-up view of the accelerators at DELTA where the steerer magnets of the storage ring are marked. A horizontal steerer magnet alters the horizontal angle of the beam by $\Delta x' = \theta_x$ (see schematig in Fig. 2.10) while a vertical steerer magnet alters the vertical angle of the beam by $\Delta y' = \theta_y$. These deflection angles are called steerer strengths in the following. In the context of orbit correction and optics analysis, it is useful to define steerer strength vectors for the horizontal steerer magnets

$$\vec{\theta}_x = \left(\theta_{x1},\ \cdots\ ,\ \theta_{xK_x} \right), \tag{2.16}$$

the vertical steerer magnets

$$\vec{\theta}_y = \left(\theta_{y1},\ \cdots\ ,\ \theta_{yK_y} \right) \tag{2.17}$$

and both together

$$\vec{\theta} = \left(\theta_{x1},\ \cdots\ ,\ \theta_{xK_x},\ \theta_{y1},\ \cdots\ ,\ \theta_{yK_y} \right). \tag{2.18}$$

The coils of the steerer magnets are mounted on combined-function quadrupoles where they overlay the magnetic field of the quadrupole with a dipole field as shown in Figure 2.11. They are fed by current sources with a range of $\pm10\,\text{A}$ and a resolution of about $2.4\,\text{mA}$ (12 bit + 1 sign bit). Their maximum rate of change is $4.7\,\text{A/s}$. The dependence of the multipole components of the combined-function quadrupoles on the two electric currents feeding the quadrupole and steerer coils were measured and interpolated in [12]. This allows to calculate the steerer strength applied by a steerer magnet for a given yoke saturation and including the

effects of the magnet's fringe fields via a conversion script named i2k. At an electron energy of 1.5 GeV, horizontal steerer magnets deflect up to 3.13 mrad if mounted on full yokes and up to 3.00 mrad if mounted on half yokes (see Ch. 2.2.1 for details on the triplet cell). Vertical steerer magnets apply up to 1.13 mrad of deflection. They are only mounted on half yokes. Groups of 4 current sources each share a controller area network (CAN) module to connect to a VME crate that serves as controller. The controller is capable of ramping all steerer magnets coherently after being fed a vector of current targets for all steerer magnets via EPICS.
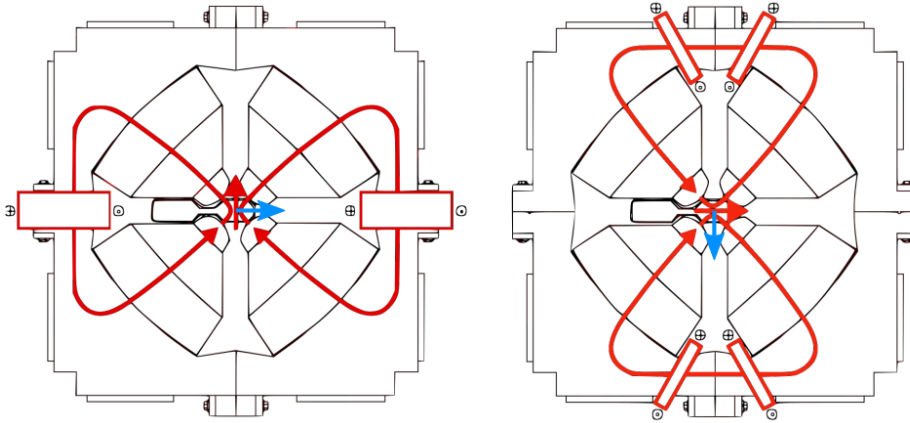
Figure 2.11: Coils of horizontal (left) and vertical (right) steerer magnets on quadrupoles. The coils and the magnetic field are marked in red. The red arrow indicates the direction of the magnetic field at the center of the quadrupole. The blue arrow marks the direction of the Lorentz force on passing electrons. Source: dissertation image from [36].

2.2.4 KICKER-BASED TUNE MEASUREMENT

The storage ring is equipped with a kicker-based tune measurement system whose measurements are used for an automated tune feedback [43]. The measurement system consists of an excitation kicker in the western arc of the storage ring and a BPM with Libera read-out electronics. The slotted-pipe kicker [44] excites betatron motion in the x and y plane driven by a 250 ns FWHM pulse (about 2/3rds or the revolution time) from a halfwave pulser. The horizontal and vertical betatron motion of the beam is measured over 2048 turns via the Libera Electron read-out electronics (see Ch. 2.2.2 for details) at BPM43. The betatron phase advance between kicker and BPM is close enough to 90° to measure a strong signal. The horizontal and vertical time series of betatron motion are then analyzed in a 2-step process on a computer. Firstly, regions of interest are determined via a fast Fourier transform. Secondly, the horizontal and vertical timeseries are fitted with sinewaves via the Marquardt-Levenberg algorithm. The arguments of the fitted sinewaves are the tunes times 2π. Overall, the complete tune measurement system achieves a precision of 25 Hz.

The measurements are used for a simple tune feedback that scales the quadrupole strengths in the arcs of the storage ring to compensate tune shifts resulting from thermal effects and orbit movements in sextupoles.

2.2.5 Optics Settings

For injections, the beam circulating in DELTA is brought close to the injection septum via a dynamic bump facilitated by three kicker magnets and a static orbit bump facilitated by three current-controlled dipole magnets. This setup allows to control two properties of the stored beam, momentum and position of its center of charge, with two three-magnet bumps instead of a single four-magnet bump. The static orbit bump can be removed after injection. This avoids unexpected kicks and focusing changes when going off-center through quadrupoles and sextupoles. This is often used for accelerator research. Keeping the tunes constant when removing the static orbit bump requires adapting the quadrupole strengths via the tune correction of the storage ring. This results in a different set of Twiss parameters (see "model server" in Fig. 11.1). The optics setting enabling injections is referred to as user optics (see Fig. 2.6 for its Twiss parameters) and the optics setting without static orbit bump is referred to as machine-study optics in the following chapters.

2.3 Slow Orbit Feedback of the Storage Ring

The closed orbit in a storage ring needs to be controlled to prevent damage to the accelerator and maximize the usability of the machine. The latter refers to increasing lifetime, stabilizing as well as maximizing synchrotron radiation intensity at beamlines and other more specialized applications like making the beam pass an undulator at a specific angle. Storage rings usually use automated orbit feedbacks with digital controllers [6]. Automated orbit feedbacks steer the horizontal orbit Eq. (2.12) measured at all BPMs towards the horizontal orbit reference $\vec{x}_{\mathrm{ref}}$, the orbit as it should be, by altering the strengths of the steerer magnets automatically. This process is a closed control loop (Fig. 2.12). Its sensors are the BPMs (see Ch. 2.2.2 for details) and its actuators are the steerer magnets (see Ch. 2.2.3 for details).

At DELTA, the controller is a program, the orbit correction software, which runs on a CPU. The software reads the current BPM orbit measurements via `EPICS`. After determining the orbit errors

$$\vec{\epsilon}_x = \vec{x} - \vec{x}_{\mathrm{ref}}, \tag{2.19}$$

it begins the calculation of new steerer currents to correct the orbit errors. This requires reading additional parameters such as the currently set steerer magnet currents and the steerer strength constraints $\vec{\theta}_x^{\mathrm{min}}$ and $\vec{\theta}_x^{\mathrm{min}}$. The currents are converted to steerer strengths $\vec{\theta}_x$ using the conversion script i2k [12]. Afterwards, the program calculates new steerer strengths

$$\vec{\theta}_x^{\diamondsuit} = \vec{\theta}_x + \eta \Delta \vec{\theta}_x^* \tag{2.20}$$

that correct the orbit errors. Here, $\Delta \vec{\theta}_x^*$ are the optimal steerer strength corrections according to an internal orbit response model and a programmatic decision-making process (see Ch. 4 for an introduction). The process has to make sure that the corrections comply with the

constraints. The step size η is a number between 0 and 1 reducing the effect of an orbit correction on the control variable Eq. (2.20). This is necessary because the internal model, which the orbit correction software uses to estimate the orbit for a vector of steerer strengths, does not perfectly reflect the physical reality of the storage ring. Reasons for this problem can include non-linearities of magnetic fields and BPMs or changes to the machine not described by the model. The orbit should therefore only be corrected in the direction set by the calculation and not directly to its exact value. If the current machine state is described well by the internal model of the software, the step size can be larger. If that is not the case, for example because the orbit deviations are large, the step size should be smaller. It is a decision made by the operator. The approach of damping a correction to a control variable is a concept used in many iterative convergence and fitting schemes, for example gradient descent [45].

Finally, the orbit correction software broadcasts the electric current equivalents of the new steerer strengths to the power supplies of the magnets and initiates ramping. The equivalents are calculated via the i2k script [12]. Reasons for not directly calculating steerer current corrections in the controller are given in Ch. 4.2. The steps of orbit measurement plus calculation and setting of the new steerer strengths together constitute a horizontal orbit correction

$$\begin{pmatrix} \vec{\theta}_x \\ \vec{x} \end{pmatrix} \quad \rightarrow \quad \begin{pmatrix} \vec{\theta}_x^{\diamond} \\ \vec{x}^{\diamond} \end{pmatrix} \tag{2.21}$$

$$\textbf{subject to} \quad \vec{\theta}_x^{\min} \leq \vec{\theta}_x \leq \vec{\theta}_x^{\max}. \tag{2.22}$$

After the ramping of the steerer magnets has commenced, the new orbit $\vec{x}^{\diamond}$ should be closer to the orbit reference. The explanations similarly apply to the vertical plane.
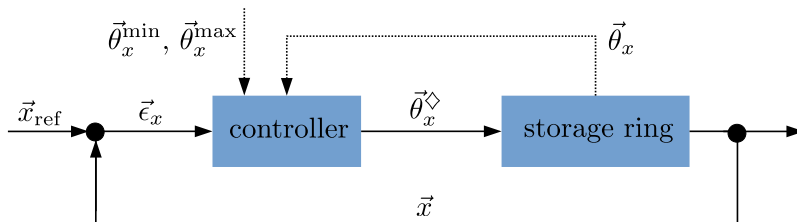
Figure 2.12: Orbit correction as a control loop. Its control and correction quantities are the orbit errors $\vec{\epsilon}_x$ Eq. (2.19) and the new steerer strengths $\vec{\theta}_x^{\diamond}$ Eq. (2.20). The current steerer strengths $\vec{\theta}_x$ and their constraints $\vec{\theta}_x^{\min}$ and $\vec{\theta}_x^{\max}$ are additionally required by the controller.

During an orbit correction, the input vector of orbit errors is assumed to be constant. The time it takes for the controller to calculate and apply the optimal steerer strengths is the reaction time of the feedback. It is the time that passes between measurement and orbit correction. Automated orbit feedbacks can be categorized according to their reaction time into slow and fast. With correction rates of less than $1\,\text{Hz}$, slow orbit feedbacks (SOFBs) are mostly used for static orbit placement although they also damp slow dynamic processes like orbit shifts induced by thermal drifts. Fast orbit feedbacks (FOFBs) damp faster dynamic processes like the effects of grid noise and ground vibrations on the stored beam.

2.3.1 History

The automated orbit feedback at DELTA, which was commissioned in the early 2000s [36][12], falls with correction rates of at least 0.1 Hz (mostly capped by the time required to ramp the magnets) under the category of SOFBs. Another orbit feedback with damping rates of up to 350 Hz, an FOFB, is under development [46]. It uses smaller faster steerer magnets (lower inductivity) and relies on a hardware-programmed field programmable gateway array (FPGA) instead of a CPU to calculate orbit corrections. This work focuses on a software upgrade for the SOFB. In 2002, DELTA commissioned an SOFB testing singular value decomposition (SVD) for calculating the optimal steerer strengths [36]. Its orbit correction software was replaced two years later with a customized SVD approach capable of subjecting the optimal steerer strengths to inequality constraints, a strategy better suited for the operation of the storage ring [47][12]. Chapter 4.4.2 describes the approach and a related method, which is also available in the 2004th software, in more detail.

Although recent developments start incorparating non-linearities via machine learning techniques [48], controllers using linear orbit response models remain common. They are reliable and have been adapted to many use cases. One is the stabilization of the beam energy [49]. A replacement for DELTA's SVD-based orbit correction software was commissioned in 2021 [50]. It uses an interior point method (IPM) for quadratic programs, a special type of convex optimization problem that includes linear inequality constraints, for the calculation of the optimal steerer strengths [51]. The program also assigns unique steerer strengths to linearly dependent steerer magnets and adds two variations of energy correction, energy stabilization and path-length minimization, to the capabilities of the controller. The new software is described in Ch. 5.

2.4 Tools for Optics Analysis of the Storage Ring

Understanding the optics of a storage ring is crucial for its operation and designing future upgrades. In this endeavor, simulation studies and optics measurements are important tools.

Lattice Models

The design of new or upgrades of existing storage rings are commonly accompanied by simulation studies with lattice models. At DELTA, this was as true for the original design study [32] as it is for a recent study identifying optics changes to offset the impact of the SCW on the beta function [52]. The basis for most optics calculations at DELTA is the *del008* optics model. It was used to develop the last major optics overhaul of the storage ring in preparation of the installation of the SAW and the U55 in 1999 [33]. In 2001, the optics model received minor upgrades such as the introduction of unified quadrupole strengths for quadrupole families and a revision of the location of beamline source points. The `MADX` version of this model [34] used within the scope of this work is referred to as the *del008.2001* optics model in the following. It expresses the combined-function quadrupole-and-steerer magnets as

two quadrupoles of half length with a thin sterer magnet between. Although the *del008.2001* optics model theoretically contains a model for the SAW, the optics calculations presented in Fig. 2.6 as well as Ch. 6 and Ch. 10 were done without it. Another optics model used within the scope of this work is the model employed in the so-called model server. The model server is an input-output controller that reads online machine parameters such as the currents for the quadrupole and steerer magnet coils of the storage ring via `EPICS` [53]. In the program, the currents are converted to quadrupole and steerer strengths using the program i2k [12] and fed into the `OCELOT` optics code [54] running the *del008.online* optics model. The results are made available via `EPICS`. The *del008.online* model is mostly the same as the *del008.2001* model but with online machine parameters and an optional SCW model. In Ch. 11, model server calculations are compared to results of the response set fit algorithm (RSFA).

2.4.1 BETA FUNCTION MEASUREMENT IN QUADRUPOLES

The first technique available at DELTA to conduct beta function measurements helped checking optics models and supported design studies for EEHG in recent years [55][56]. After exciting a tune shift Δq_x by changing a quadrupole strength by $\Delta\Omega$, the average horizontal beta function in the corresponding quadrupole can be calculated as [14]

$$\overline{\beta}_x = \frac{4\pi}{l}\frac{\Delta q_x}{\Delta\Omega}.$$

(2.23)

Here, l is the length of the magnet. At DELTA, the quadrupole coil currents are altered via a relay cascade that allows to superimpose an additional current from a bipolar current source on the familiy-specific coil currents. A relay cascade refers to a cocatenation of relays in layers to allow for more than two ouputs. The changes in quadrupole strengths associated with changes in coil currents can be calculated via the conversion script i2k [12].

2.4.2 OPTICAL FUNCTION MEASUREMENT AT BEAM POSITION MONITORS

The second meaurement technique for optical functions used at DELTA is the closed-orbit bilinear-exponential algorithm (COBEA) [13]. It extracts the tunes as well as the coupled beta functions, the coupled betatron phase advances and scaled dispersion values at all BPMs from an orbit response matrix (ORM) measurement (see Ch. 4.2 for details) by fitting the bilinear-exponential model with dispersion (BE+d model) to the matrix. An introduction to the COBEA algorithm is given in Ch. 8.

RECENT RESEARCH

COBEA was tested on experimental data from BESSY II, the MLS and DELTA [13][57]. In the case of BESSY II and the MLS, COBEA's optical function estimates were compared to fits with the linear optics from closed orbits (LOCO) algorithm [58]. Differences in beta function results were attributed to normalization errors. The normalization accuracy was limited by measurement uncertainties originating from the shortness of the drift spaces used

to determine the invariants of motion. Overall, the differences were greater for BESSY II than for the MLS. At DELTA, the beta function estimates returned by COBEA were compared to coupled beta function estimates calculated from turn-by-turn time series of orbit deviations [13]. Although both matched well, the comparison was only possible at a subset of 10 out of 54 BPMs with turn-by-turn capable measurement electronics. COBEA's tune and dispersion fitting capabilities were later also verified at DELTA [59]. The shape of one of COBEA's dispersion fit results matched the shape of a frequency response of the storage ring well. A COBEA analysis of response matrices recorded over several years also produced tunes very close to measurements.

The measurement of an orbit response matrix for the analysis with COBEA requires a dedicated ORM measurement that takes about 15 minutes at DELTA. Orbit responses and orbit corrections are related. Therefore, initial research into adapting COBEA's approach to multi-steerer orbit response measurements and integrating the adapted algorithm into the SOFB software was conducted [60][61]. Chapter 9 introduces a more mature version of the adapted algorithm with better start value generation, the RSFA. It is benchmarked against COBEA in simulation studies featuring strong coupling in Ch. 10. Chapter 11 presents experimental results for the RSFA. Additional research includes a derivation of the steerer parameters in the BE+d model [62]. It is presented in Appendix 14 in detail.

3 Linear Beam Dynamics

The theoretical concepts explained in the following build the foundation for understanding orbit correction approaches with linear orbit response models (see Ch. 4 and Ch. 5) as well as understanding optical function measurements via the COBEA algorithm (see Ch. 8) and the RSFA (see Ch. 9).

3.1 Coupled Betatron Motion

Coupled betatron motion is a generalization of uncoupled betatron motion, which was introduced in Ch. 2.1.1, and two parameterizations exist to describe it. The first was introduced by D. A. Edwards and L. C. Teng in 1973 [63] and the second by H. Mais and G. Ripken in 1982 [64]. While the Edwards-Teng parameterization uses a coordinate transformation to describe coupled betatron oscillations with a single amplitude and phase per mode but in rotated coordinates, the Mais-Ripken parameterization keeps the coordinate system of the co-moving coordinate frame but increases the number of optical functions. The following introduction to coupled betatron motion mainly follows [65], a variant of the Mais-Ripken parameterization, which presents a comprehensive description of coupled betatron motion using complex oscillations, that coincides with the parameterization used in [13] to describe coupled orbit responses (see Ch. 3.2.1 for details).

Motion dynamics in the co-moving coordinate system of a storage ring in linear approximation are modeled by two coupled second-order differential equations of the four transverse phase space coordinates $x(s)$, $x'(s)$, $y(s)$ and $y'(s)$ [66]. Their solutions describe particle trajectories through quadrupoles, dipoles (weak focusing), the fringe fields of both magnets as well as drift spaces and can be used to calculate the evolution of an initial phase space vector $\vec{z}(s_0)$ at any position s in the lattice

$$\vec{z}(s) = \boldsymbol{T}_{s_0 \to s}\vec{z}(s_0). \tag{3.1}$$

Here, the transfer map $\boldsymbol{T}_{s_0 \to s}$ is a 4x4 symplectic matrix determined by the lattice between s_0 and s. Its calculation requires the knowledge of the position, type, strength, length and skew angle of each magnet as well as the length of each drift space in that part of the lattice. If start and end position differ by exactly one turn, i.e. $s = s_0 + L$, then $\boldsymbol{T}_{s_0 \to s_0 + L}$ is called a one-turn transfer map $\boldsymbol{T}_{s_0 \to s_0}$ and it encodes important properties of particle motion. The solution of the eigenvalue problem

$$\vec{z}(s_0 + L) = \boldsymbol{T}_{s_0 \to s_0}\vec{z}(s_0) \tag{3.2}$$
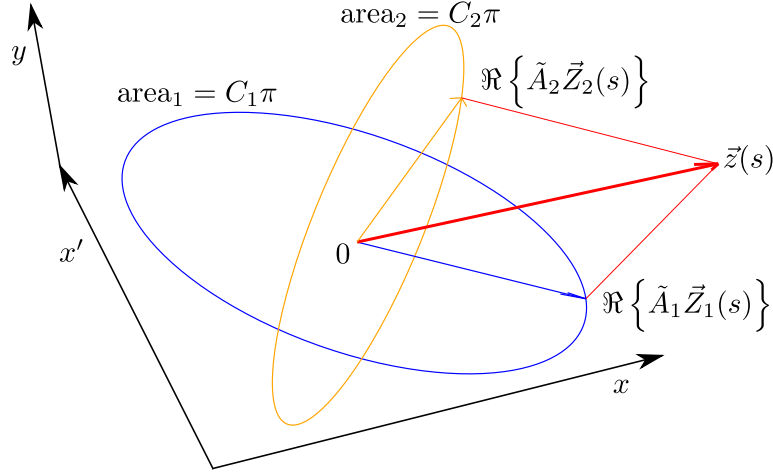
Figure 3.1: Projection of coupled betatron motion as superposition of two modes from 4D to 3D.

returns $M = 2$ complex eigenvalue pairs $e^{\pm i2\pi q_m}$ where $m = 1$-2 and two corresponding pairs of complex eigenvectors $\vec{Z}_m$ and $\vec{Z}_m^*$. Under the assumption of bound motion and neglect of synchrotron radiation, the eigenvalues are constrained to a complex unit circle $|e^{\pm i2\pi q_m}| = \pm 1$ to preserve the absolute size of the phase space vector and to comply with Liouville's theorem. After normalizing the eigenvectors such that

$$\vec{Z}_m^\dagger \boldsymbol{U} \vec{Z}_m = -2i \tag{3.3}$$

with a conjugated and transposed eigenvector $\vec{Z}_m^\dagger$ and a matrix

$$\boldsymbol{U} = \begin{pmatrix} 0 & 1 & 0 & 0 \\ -1 & 0 & 0 & 0 \\ 0 & 0 & 0 & 1 \\ 0 & 0 & -1 & 0 \end{pmatrix} \tag{3.4}$$

is being fulfilled, the phase space vector can be expressed as a real-valued sum of scaled eigenvectors $\tilde{A}_m \vec{Z}_m$ (see Eq. (3.8) for an interpretation) that can be propagated to any position in the storage ring

$$\vec{z}(s) = \boldsymbol{T}_{s_0 \to s} \sum_{m=1}^{M} \Re\left\{ \tilde{A}_m \vec{Z}_m(s_0) \right\} = \sum_{m=1}^{M} \Re\left\{ \tilde{A}_m \vec{Z}_m(s) \right\}. \tag{3.5}$$

On the next turn, this vector is rotated by the eigenvalue

$$\boldsymbol{T}_{s \to s} \vec{z}(s) = \sum_{m=1}^{M} \Re\left\{ \tilde{A}_m e^{i2\pi q_m} \vec{Z}_m(s) \right\} \tag{3.6}$$

revealing a superposition of two phase space oscillation modes, the coupled betatron oscillation. Each turn, the modes advance with constant phase advances $2\pi q_m$, where q_m are the mode
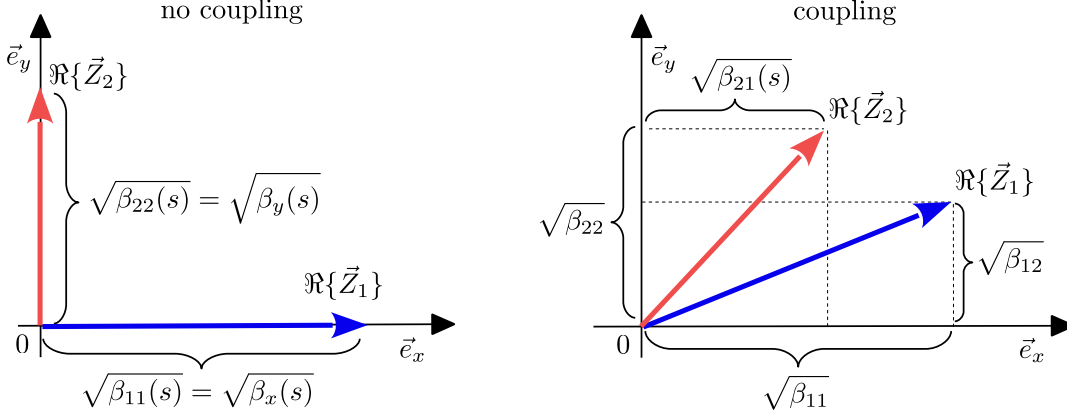
Figure 3.2: Relation of the eigenvectors Eq. (3.7) (colored arrows) and the (un)coupled beta functions. Without transverse coupling (left), the coupled beta functions $\beta_{11}(s)$ and $\beta_{22}(s)$ match the uncoupled ones $\beta_x(s)$ and $\beta_y(s)$ while the coupling terms $\beta_{12}(s)$ and $\beta_{21}(s)$ are 0. In the presence of coupling (right), the eigenvectors rotate around the beam axis that is perpendicular to the transverse plane shown here.

tunes, along phase space ellipses with areas πC_m, one for each mode. The constants C_m are generalizations of the Courant-Snyder invariant. The normalization process Eq. (3.3) effectively divides each eigenvector by the square root of its invariant. Figure 3.1 displays a 3D schematic on the relation of phase space vector, eigenvectors and the phase space ellipses. The evolution of the coupled betatron oscillation around the storage ring is described by 13 generalized optical functions of which 10 are independent. They are properties of the lattice hidden in the eigenvectors

$$\vec{Z}_1 = e^{i\Phi_1(s)} \begin{pmatrix} \sqrt{\beta_{11}(s)} \\ -\dfrac{i(1-u(s))+\alpha_{11}(s)}{\sqrt{\beta_{11}(s)}} \\ \sqrt{\beta_{12}(s)}e^{i\nu_1(s)} \\ -\dfrac{iu(s)+\alpha_{12}(s)}{\sqrt{\beta_{12}(s)}}e^{i\nu_1(s)} \end{pmatrix} \quad \text{and} \quad \vec{Z}_2 = e^{i\Phi_2(s)} \begin{pmatrix} \sqrt{\beta_{21}(s)}e^{i\nu_2(s)} \\ -\dfrac{iu(s)+\alpha_{21}(s)}{\sqrt{\beta_{21}(s)}}e^{i\nu_2(s)} \\ \sqrt{\beta_{22}(s)} \\ -\dfrac{i(1-u(s))+\alpha_{22}(s)}{\sqrt{\beta_{22}(s)}} \end{pmatrix}. \tag{3.7}$$

Here, the four coupled beta functions β_{mw} are projections of the amplitude of the betatron oscillation with $C_m = 1$ of the m-th mode onto $W = 2$ planes indexed with $w = 1\text{-}2$. If no coupling is present, the coupled beta functions match the uncoupled beta functions for $m = w$ (see Fig. 3.2 for details). The four coupled alpha functions $\alpha_{mw}(s)$ coincide with the negative half derivatives of the coupled beta functions $\alpha_{mw}(s) = -\beta'_{mw}(s)/2$ in areas where no longitudinal magnetic field is present. The four coupled phase functions $\Phi_m(s)$ and their off-plane modifiers $\nu_m(s)$ model the phase advance of the betatron oscillation modes. Without transverse coupling, $\Phi_0(s)$ and $\Phi_1(s)$ are equal to $\Phi_x(s)$ and $\Phi_y(s)$. The remaining generalized optical function $u(s)$ has no equivalent in the description of uncoupled betatron motion. The complex scaling factors

$$\tilde{A}_m = \sqrt{C_m}e^{i\Phi_m^{\text{init}}}, \tag{3.8}$$

determine the initial phases Φ_m^{init} and the amplitudes $\sqrt{C_m \beta_{mw}(s)}$ of a specific particle.

3.2 COUPLED ORBIT RESPONSE

The closed orbit in a storage ring shifts to a new orbit if dipole strengths are altered. This phenomenon, called orbit response, is lattice dependent and can, in the approximation of coupled linear beam dynamics, be expressed analytically in two forms. The first form describes the lattice dependency with optical functions. The second form uses transfer maps. Both models are compared in the appendix 14.3.1.

3.2.1 THE BILINEAR-EXPONENTIAL MODEL

Trajectories in a storage ring in coupled linear approximation can according to [13] be modeled as betatron oscillations. When a kick is applied, the closed orbit switches from being the ideal orbit to a former betatron oscillation. Figure 3.3 displays a before-and-after schematic of the process. The kick closes the betatron oscillation and opens the ideal orbit. Otherwise, both trajectories remain the same. The new closed orbit can therefore be written as a combination of Eq. (3.5) and Eq. (3.6)

$$\vec{z}(s) = \begin{cases} \sum\limits_{m=1}^{M} \Re\left\{ \tilde{A}_m \vec{Z}_m(s) \right\} & \text{for} \quad s > s_k \\ \sum\limits_{m=1}^{M} \Re\left\{ \tilde{A}_m e^{i2\pi q_m} \vec{Z}_m(s) \right\} & \text{for} \quad s < s_k \end{cases} \tag{3.9}$$

Here, the complex scaling factor Eq. (3.8) corrects the amplitude and the phase of each mode to match the orbit response. After passing the steerer magnet, the beam firstly traverses the $s > s_k$ section of the lattice, passes the origin at $s = 0$ and secondly traverses the $s < s_k$ section. The eigenvector in the $s < s_k$ section therefore has to be modified by an additional phase factor $e^{i2\pi q}$ that accounts for the turn-dependent phase shift occurring at the origin of the longitudinal coordinate frame. Both parts can be assembled into a single analytical expression

$$\vec{z}(s) = \sum_{m=1}^{M} \Re\left\{ A_m e^{i\pi q_m \text{sign}(s_k - s)} \vec{Z}_m(s) \right\} \quad \text{for} \quad s \neq s_k. \tag{3.10}$$

by substituting $A_m = e^{i\pi q_m} \tilde{A}_m$. These equations represent the bilinear-exponential (BE) model for thin steerer magnets. It describes the orbit response in the complete storage ring except at the position of the kick. Although not covered here, the BE model also applies to thick steerer magnets without any modification of the analytical expression. The derivation of an analytical expression for the steerer parameters in thin-steerer-magnet approximation Eq. (14.13) [62] is given in the appendix 14.

$$\vec{z}(s) = \sum_{m=1}^{M=2} \Re\left\{\tilde{A}_m \vec{Z}_m(s)\right\}$$

$$\vec{z}(s) = \sum_{m=1}^{M=2} \Re\left\{\tilde{A}_m e^{i2\pi q_m} \vec{Z}_m(s)\right\}$$
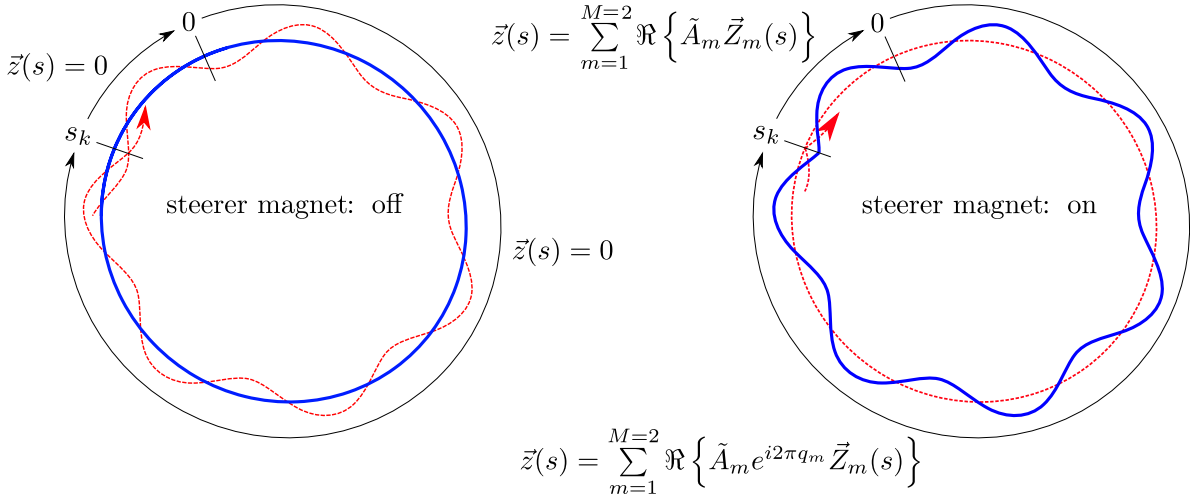
Figure 3.3: Closed orbits (blue) and a betatron oscillation (red) for the design lattice (left) and with a kick at position s_k (right). The equations parameterize the closed orbit in the two segments $s < s_k$ and $s > s_k$.

3.2.2 Orbit Response from Transfer Maps

Similar to Eq. (3.2), the closed orbit at the position of a thin steerer magnet s_k fulfills [67]

$$\vec{z}(s_k + L) = \boldsymbol{T}_{s_k \to s_k} \vec{z}(s_k) + \vec{\theta} \tag{3.11}$$

where $\vec{\theta} = (0, \theta_x, 0, \theta_y)^{\mathrm{T}}$ is the kick applied by the steerer magnet and $\boldsymbol{T}_{s_k \to s_k}$ is the one-turn transfer matrix mapping a phase space vector at the steerer magnet to the next turn. Solving this equation for the closed orbit and propagating it through the storage ring with a transfer map $\boldsymbol{T}_{s_k \to s}$ gives the orbit response

$$\vec{z}(s) = \boldsymbol{T}_{s_k \to s}(\boldsymbol{1} - \boldsymbol{T}_{s_k \to s_k})^{-1}\vec{\theta} \quad \text{for} \quad s \neq s_k \tag{3.12}$$

at an arbitrary position s in the storage ring. The model is widely used in accelerator physics [68][17][67].

3.3 Dispersive Orbit Drifts

The RF frequency of the storage ring controls the orbit length and can be used to change the beam energy (see Ch. 2.1.2 for an explanation). Field errors, thermal effects and active orbit steering also affect this equilibrium. They divert the beam from its unperturbed orbit changing the orbit length by an additional Δs_r as illustrated in Fig. 3.4. Since the orbit length has to conform with the RF frequency, the beam energy then changes by δ so that [17]

$$\frac{f}{f + \Delta f} - 1 \approx \alpha\delta + \frac{\Delta s_r}{L} \tag{3.13}$$

is fulfilled. See Eq. (2.10) for more details on the approximation. When the beam energy changes, the transverse position of the closed orbit adjusts by $\delta\vec{D}(s)$. The vector

$$\vec{D}(s) = \left(D_x(s), D_x'(s), D_y(s), D_y'(s)\right)^T \tag{3.14}$$

contains the horizontal and vertical dispersion function and their longitudinal derivatives (see Ch. 2.1.2 for an explanation). The introduced orbit response models have to be revised to account for this effect. The bilinear-exponential model with dispersion (BE+d model) is [13]

$$\vec{z}(s) = \sum_{m=1}^{M} \Re\left\{A_m e^{i\pi q_m \mathrm{sign}(s_k-s)}\vec{Z}_m(s)\right\} + \delta\vec{D}(s) \quad \text{for} \quad s \neq s_k. \tag{3.15}$$

Similarly, a transfer-map model with dispersion can be calculated with 4D transfer maps as [67]

$$\vec{z}(s) = \boldsymbol{T}_{s_k \to s}(\boldsymbol{1} - \boldsymbol{T}_{s_k \to s_k})^{-1}\vec{\theta} + \delta\vec{D}(s) \quad \text{for} \quad s \neq s_k \tag{3.16}$$

or according to equation (3.12) but with 6D transfer maps. The latter will result in a 6D closed orbit that contains the energy deviation as the 6-th coordinate.
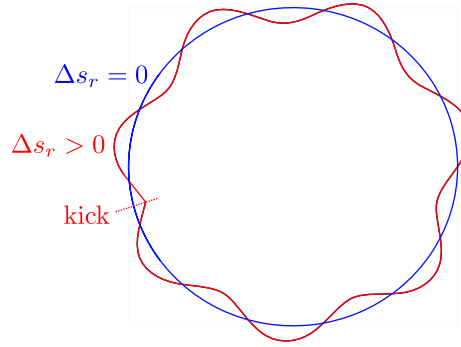
Figure 3.4: A field error or intentional kick from a steerer magnet diverts the beam from its ideal orbit (blue) and lengthens it (red).

4 BUILDING BLOCKS OF ORBIT CORRECTION SOFTWARE AT DELTA

Building on the linear orbit response models explained in Ch. 3.2, the following Chapter firstly outlines common concepts of orbit correction used in both of DELTA's SOFB software generations. Secondly, the core DELTA-specific optimization methods employed in the first controller generation, the SVD-based software [12], are explained. The chapter builds the foundation for understanding the optimization modes available in the second controller generation, the IPM-based software, which is introduced in Ch. 5. All explanations given in the following also apply to the vertical plane.

4.1 INTRODUCTION

A horizontal orbit correction Eq. (2.20) and Eq. (2.21) steers the orbit towards the horizontal orbit reference. The calculation of optimal steerer strength corrections $\Delta\vec{\theta}_x^*$ requires three components.

1. A model to predict the effect of the steerer magnets on the orbit. Both, the SVD- and the IPM-based software, use measured ORMs for this purpose. The measurement process is described in Ch. 4.2.

2. A figure of merit to determine whether the predicted orbit is better or worse. Again, both software generations use the same quantity, the weighted root mean square (WRMS) of orbit errors. It is explained in Ch. 4.3.

3. A process to calculate the optimal steerer strengths. Both software generations rely on minimization problems to do that. Chapter 4.4 lists three methods to formulate and solve minimization problems to calculate optimal steerer strength corrections that are either widely used in accelerator physics or employed in the SVD-based software. The methods of the IPM-based software are explained in Ch. 5.2 and Ch. 5.3.

4.2 ORBIT RESPONSE MATRIX

An orbit correction software requires a model relating the steerer strength of all steerer magnets to the closed orbit position at all BPMs. In the approximation of linear beam dynamics, changing the strength of a steerer magnet k by $\Delta\theta_{xk}$ excites a linear orbit response $\Delta\vec{x}(\Delta\theta_{xk})$ at all BPMs. The orbit response could either be described with the BE+d model Eq. (3.15)

or the transfer map model with dispersion Eq. (3.16). For the purpose of orbit correction, it is useful to normalize the orbit response as in [66]

$$\vec{R}_{xk} = \frac{\Delta \vec{x}(\Delta \theta_{xk})}{\Delta \theta_{xk}} \tag{4.1}$$

and aggregate the orbit responses of all steerer magnets in the ORM $\boldsymbol{R}_x$, where the orbit response of each steerer magnet is a column of the matrix. The ORM allows to calculate the orbit response when changing the strength of all horizontal steerer magnets by $\Delta \vec{\theta}_x$ as

$$\Delta \vec{x} = \boldsymbol{R}_x \Delta \vec{\theta}_x. \tag{4.2}$$

The ORM in both controller generations is measured by exciting each steerer magnet individually. A schematic drawing of the measurement process for a single element is given in Fig. 4.1. The implementation of the measurement process was done by [36]. Although it is possible to measure an ORM with an electric-current denominator, using the steerer strength calculated via the i2k conversion tool [12] instead makes the ORM more resilient to optics changes. This is a result of the steerer magnets being mounted on quadrupoles at DELTA (see Ch. 2.2.3 for details). Changing optics, which implies altering quadrupole currents, therefore also changes the deflection angles of the steerer magnets. In addition to that, a steerer-strength denominator allows an ORM to be used at different beam energies. As DELTA is not ramped anymore, this is, however, more of a theoretical argument.
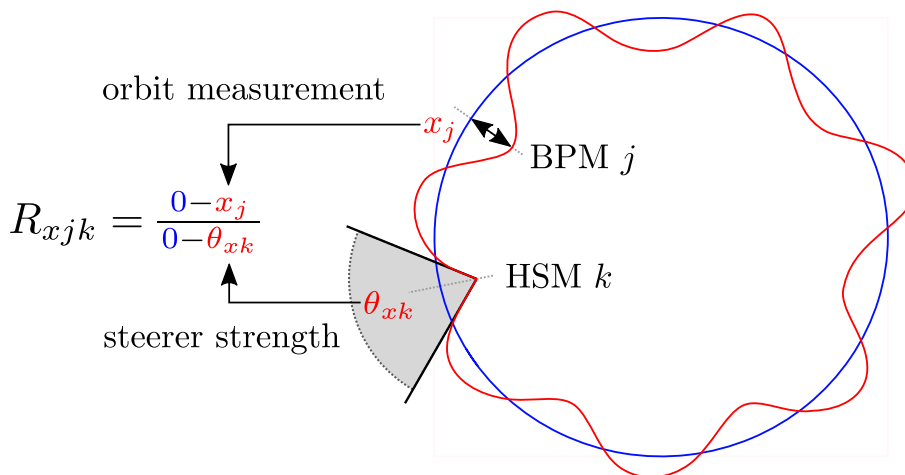
Figure 4.1: Measuring an element of the horizontal ORM at a BPM j for the horizontal steerer magnet (HSM) k relative to the ideal orbit. Initially, the steerer strength at the HSM and the orbit are both zero. After applying a steerer strength θ_{xk}, which can be interpreted as kick angle, the orbit at the BPM changes to x_j.

4.3 WEIGHTED ROOT MEAN SQUARE OF ORBIT ERRORS

An orbit correction software requires a scalar figure of merit determining the quality of orbit correction for optimizing the orbit. This quantity is the weighted root mean square of orbit errors (WRMS) [12]

$$\text{WRMS}(\vec{\epsilon}_x) = ||\boldsymbol{W}_x \vec{\epsilon}_x||_2 = \sqrt{\frac{1}{J} \sum_{j=1}^{J} w_{xj}^2 \epsilon_{xj}^2}. \tag{4.3}$$

Here, $||...||_2$ marks the Euclidean vector norm and $\vec{\epsilon}_x$ are the orbit errors Eq. (2.19). The WRMS maps the vector product of weighted errors to a scalar. Compared to the l1 vector norm, the Euclidean vector norm has the benefit of increasing with the square of orbit deviations at each BPM. This makes the software preferably correct the orbit at BPMs with large orbit errors if the orbit cannot be corrected onto the orbit reference everywhere. The latter is common at storage rings with less steerer magnets than BPMs. The strong imbalance of steerer magnets and BPMs at DELTA makes it necessary to additionally add a weight matrix $\boldsymbol{W}_x$ to the Euclidean norm. It is a diagonal matrix multiplying the orbit error at each BPM with a BPM-specific weight w_{xj}. It is necessary to achieve an above-average orbit correction quality at the injection septum, the undulators U55 and U250 and some source points of beamlines. Figure 4.2 displays a plot of the weight distribution at DELTA. Combined, the heuristics of the WRMS make orbit correction at important BPMs (large weights) a priority for the orbit correction software if the orbit errors at less important BPMs (small weights) are not too large.
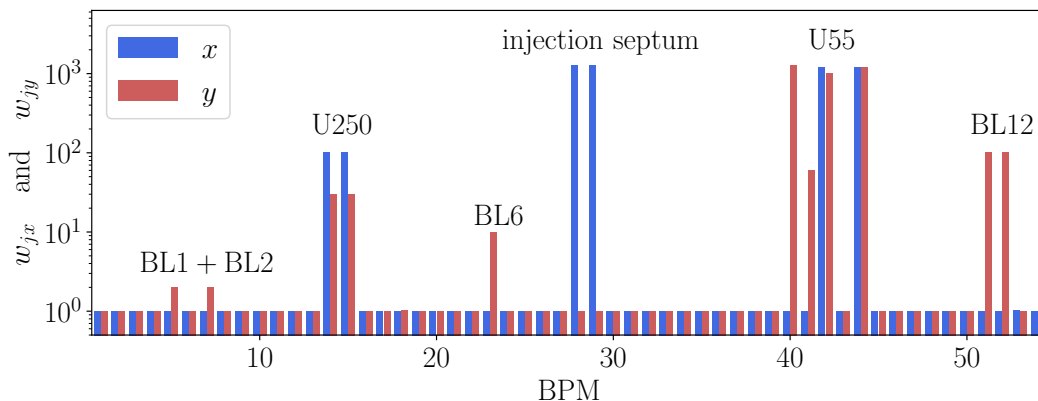
Figure 4.2: BPM weights from orbit reference *reference.200710-2* used in user operation at DELTA. The largest weights > 1000 are assigned to the injection septum and the undulator U55.

4.3.1 PHYSICAL INTERPRETATION

The process of orbit correction theoretically distributes the weighted orbit errors between all BPMs equally. In situations where the orbit correction is optimal, the WRMS value should therefore equal the product of weight and orbit error at each BPM

$$\text{WRMS}(\vec{\epsilon}_x^*) \approx w_{xj}\epsilon_{xj}. \tag{4.4}$$

In this approximation, a WRMS value of $2\,\text{mm}$ makes the orbit error about $2\,\text{µm}$ at a BPM with weight 1000 and $4\,\text{µm}$ at a BPM with weight 500. This interpretation only works for the largest weight tier at DELTA (> 1000) well because the orbit correction software internally uses the square of the orbit WRMS. The impact of an orbit error at a BPM with weight 1000 on orbit correction is therefore 100 times bigger than the impact of the same orbit error at another BPM with weight 100. The smaller weights ≤ 100 are so much smaller than the largest weight tier that the approximation given in Eq. (4.4) is lost in noise. Another limitation of this interpretation is the resolution of the BPMs.

4.4 ORBIT CORRECTION

The process of orbit correction refers to finding a set of steerer strength corrections that correct a given set of orbit errors. If the ORM is a square matrix and is full rank, the optimal steerer strength corrections can be obtained by inverting

$$\mathbf{R}_x \Delta \vec{\theta}_x^* = \vec{\epsilon}_x \tag{4.5}$$

yielding [14]

$$\Delta \vec{\theta}_x^* = \mathbf{R}_x^{-1} \vec{\epsilon}_x. \tag{4.6}$$

At many storage rings including DELTA, neither is the case. In more general terms, the process of orbit correction refers to finding an orbit with a better orbit correction quality that can be parameterized as minimizing the WRMS of the expected orbit errors $\vec{\epsilon}_x + \boldsymbol{R}_x \Delta \vec{\theta}_x$ after correction

$$\min_{\Delta \vec{\theta}_x} \quad \text{WRMS}\left(\vec{\epsilon}_x + \boldsymbol{R}_x \Delta \vec{\theta}_x \right). \tag{4.7}$$

The minimization process distributes the weighted orbit errors evenly across all BPMs (see Ch. 4.3.1). This and similar optimization problems introduced are referred to as orbit correction problems in this work as their formulation and methods to solve them lie at the heart of both orbit correction software generations, the SVD-based software from 2004 and the new IPM-based software.

4.4.1 SINGULAR VALUE DECOMPOSITION

The orbit correction problem can be solved by pseudoinversion of the ORM via SVD. An additional application of SVD is found in regularization. Both techniques are widely used in accelerator physics and are explained in the following. SVD decomposes the ORM into a matrix product [69]

$$\boldsymbol{R}_x = \boldsymbol{U} \boldsymbol{\Sigma} \boldsymbol{V}^{\mathrm{T}} \tag{4.8}$$

that can be interpreted as a principal component analysis of the data set of steerer-specific orbit responses $\vec{R}_{xk}$ that forms the ORM

$$\boldsymbol{R}_x = \left(\vec{R}_{xk} \right). \tag{4.9}$$

Here, $k = 1 \cdots K$ indexes the K steerer magnets. The first factor

$$\boldsymbol{U} = (\vec{u}_j), \tag{4.10}$$

where $j = 1 \cdots J$ indexes the J BPMs, contains the principal components $\vec{u}_j$. It is a $(J \times J)$ orthonormal matrix. The principal components pose an alternative basis for the K columns and are chosen iteratively with each additional principal component maximising the described data variance while being orthonormal to all its kin. There are as many principal components as there are BPMs. At DELTA $(J > K)$, the second factor

$$\boldsymbol{\Sigma} = \begin{pmatrix} \sigma_1 & \cdots & 0 \\ \vdots & \ddots & \vdots \\ 0 & \cdots & \sigma_i \\ \vdots & \ddots & \vdots \\ 0 & 0 & 0 \end{pmatrix} \tag{4.11}$$

is a rectangular $(J \times K)$ diagonal matrix. Its diagonal is made up of real numbers σ_i called singular values where the size of the i-th singular value reflects the data variance described by the i-th principal component. Since each additional principal component stands for equal or lower data variance, its corresponding singular value is also the same or smaller. This evolution can be visualized in a so-called singular value spectrum (see example in Fig. 4.3). If $J > K$, there are K singular values. The third factor

$$\boldsymbol{V}^T = (\vec{v}_k)^T \tag{4.12}$$

is a $(K \times K)$ orthonormal matrix. It contains principal-component coefficients for each steerer. The orbit response of each steerer magnet can therefore be written as sum of principal components

$$\vec{R}_{xk} = \sum_{i=1}^{I=K} \sigma_i v_{ik} \vec{u}_i \quad \text{for} \quad J > K \tag{4.13}$$

where the coefficients determine how much each principal component contributes. The first coefficient, the singular value, is the same for all steerer magnets. The second coefficient v_{ik} is steerer-specific. The importance of the principal components hence varies from steerer to steerer. In a real ORM, the first principal components are significantly more important than the last few principal components as the corresponding singular values are orders of magnitude apart (see also example in Fig. 4.3).

PSEUDOINVERSE

The SVD matrix product can be inverted by individually inverting each matrix yielding the Moore-Penrose pseudoinverse of the ORM [70]

$$\boldsymbol{R}_x^+ = \boldsymbol{V} \boldsymbol{\Sigma}^+ \boldsymbol{U}^{\mathrm{T}}. \tag{4.14}$$
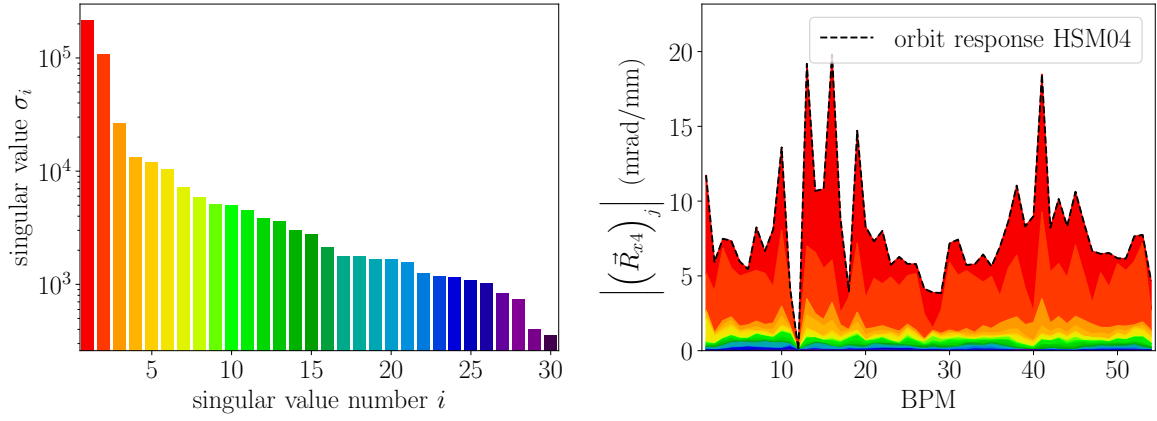
Figure 4.3: Singular value spectrum for the horizontal part of the ORM *response.160311-1* (left) and the principal component decomposition of the orbit response of the horizontal steerer magnet HSM04 $\vec{R}_{x4}$ from the same matrix according to equation (4.13) (right). Each singular value belongs to the principal component of the same color. The orbit response at BPM12 is zero because the BPM is currently not in use due to one of its four pick-up electrodes being broken.

Here, the pseudoinverse $\mathbf{\Sigma}^+$ is calculated by transposing $\mathbf{\Sigma}$ and replacing each sigular value on its diagonal with its own reciprocal value. The matrix inverses of the two orthogonal matrices are their transposes. A pseudoinverse has similar properties as an inverse matrix as it fulfills [71]

$$\mathbf{R}_x \mathbf{R}_x^+ = \mathbf{I} \tag{4.15}$$

where $\mathbf{I}$ is the unit matrix. Yet, attempting to solve a linear equation system with a pseudoinverse only gives the best possible solution in a least-squares sense [70]. An optimal set of steerer strengths

$$\vec{\theta}_x^* = \mathbf{R}_x^+ \Delta\vec{x} \tag{4.16}$$

calculated with the pseudoinverse therefore solves the orbit correction problem 4.7.

Regularization

Regularization refers to the heuristic modification of the objective function of an optimization problem to achieve a more desirable outcome. In the context of orbit correction, it refers to altering the orbit correction problem in a way that it prefers smaller steerer strength corrections while still decreasing the WRMS. This goal reflects the limited accuracy of the linear orbit response model: the larger the steerer strength, the more the accuracy of the model decreases. Non-linearities of magnetic fields and BPMs are among the reasons for the limited accuracy. Large changes of the steerer strength may therefore yield unexpected results. At DELTA, the traditional way to go about regularization is to remove principal components from the

ORM. This requires decomposing the matrix according to Eq. (4.8), replacing a number of the smallest singular values in the $\boldsymbol{\Sigma}$ matrix with zeros and then putting the matrix back together. While pruning singular values changes the steerer strength corrections resulting from an orbit correction quite substantially, the expected WRMS does not change much as long as the cutting is limited to just a few singular values (see example in Fig. 4.4). The number of principal components removed at DELTA depends on the ORM that is in use. An unwanted side-effect of this regularization technique is the rank reduction of the ORM because it introduces linear dependencies among steerer magnets. Linearly dependent steerer magnets are not assigned with unique steerer strengths when solving the orbit correction problem. Instead, their optimal steerer strength setting depends on their linearly dependent kin. As such, the steerer strength from a linearly dependent steerer may change over time and introduce orbit noise. A method to prevent this issue, which is employed by the new IPM-based software, is presented in Ch. 5.2.2.
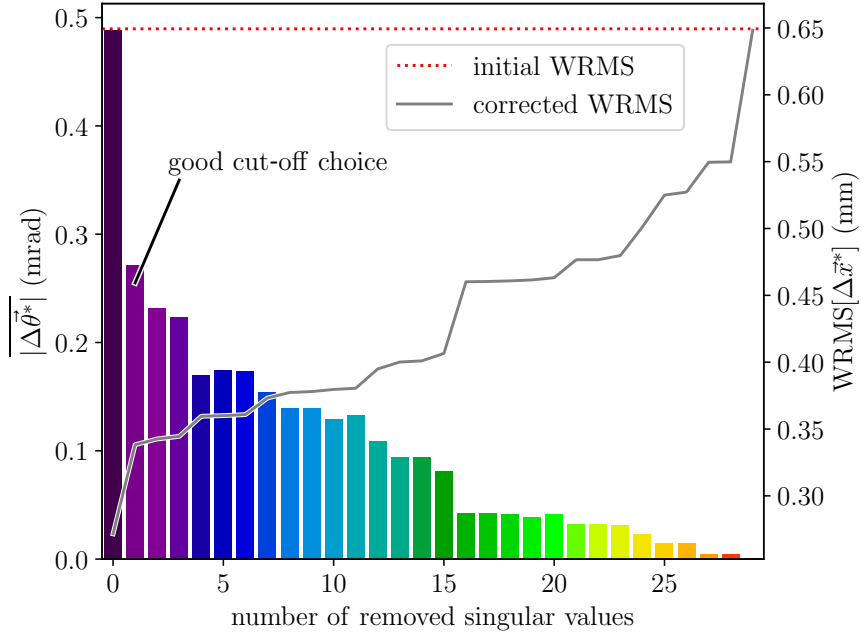
Figure 4.4: Effect of regularization on an orbit correction: weighted orbit errors measured in March 2021 are corrected towards the weighted orbit reference *reference.201207-1* with the regularized ORM *response.160311-1*. The more singular values are removed, the worse the orbit correction becomes as signaled by an increasing WRMS of orbit errors after the orbit correction commenced WRMS[$\Delta\vec{x}^*$] (gray line). This is, however, accompanied by a decreasing average change in steerer strength $\overline{|\Delta\vec{\theta}_x^*|}$ (bar plot). The colors of the bars reflect the color coding of the singular value spectrum and the principal components of HSM04 presented in Fig. 4.3. In this example, it would be a reasonable decision to exclude one principal component from the orbit response matrix before correcting the orbit as it cuts the required average change in steerer strengths nearly in half to around 0.28 mrad but increases the WRMS only marginally to about 0.35 mm.

4.4.2 INSUFFICIENT STEERER STRENGTH

The available steerer strength may at times be insufficient to correct a given vector of orbit errors. In that case, inequality constraints for the steerer strengths have to be added to the orbit correction problem. The minimization problem then becomes [12]

$$\min_{\Delta\vec{\theta}_x} \quad \text{WRMS}\left(\vec{\epsilon}_x + \boldsymbol{R}_x\Delta\vec{\theta}_x\right) \tag{4.17}$$

$$\text{subject to} \quad \vec{\theta}_x^{\min} \leq \vec{\theta}_x + \Delta\vec{\theta}_x \leq \vec{\theta}_x^{\max} \tag{4.18}$$

where $\vec{\theta}_x^{\min}$ and $\vec{\theta}_x^{\max}$ are the lower and upper constraints on the strength of each steerer. A solution of the constrained orbit correction problem satisfies the Karush-Kuhn-Tucker theorem [69]. It states that for an optimization problem with objective function $f(\vec{x})$ subject to inequality constraints $\vec{g}(\vec{x}) \leq 0$ and equality constraints $\vec{h}(\vec{x}) = 0$ the point $\vec{x}^*$ is an optimal solution if there are coefficients $\vec{\mu}^*$ and $\vec{\lambda}^*$ so that the Lagrangian

$$\mathcal{L}(\vec{x}, \vec{\mu}, \vec{\lambda}) = \vec{\mu}^{\mathrm{T}}\vec{g}(\vec{x}) + \vec{\lambda}^{\mathrm{T}}\vec{h}(\vec{x}) \tag{4.19}$$

is stationary at the minimum

$$\vec{\nabla}\mathcal{L}(\vec{x}^*, \vec{\mu}^*, \vec{\lambda}^*) = 0. \tag{4.20}$$

The coefficients are commonly referred to as Lagrange multipliers. The application of the gradient gives a set of equations that are the Karush-Kuhn-Tucker conditions. The Karush-Kuhn-Tucker conditions for the problem at hand are

$$\text{grad}\left(\text{WRMS}\left(\vec{\epsilon}_x + \boldsymbol{R}_x\Delta\vec{\theta}_x^*\right)\right) = \sum_k (\mu_k^{\min})^* \vec{n}_k^{\min} + \sum_k (\mu_k^{\max})^* \vec{n}_k^{\max}. \tag{4.21}$$

Here, the strength limits of each steerer magnet $k = 1, \cdots, K$ are expressed via the normal vectors of the constant minimum and maximum inequality constraints $\vec{n}_k^{\min}$ and $\vec{n}_k^{\max}$ with corresponding Lagrange multipliers $\mu_k^{\min}$ and $\mu_k^{\max}$. The $(...)^*$ marks the optimal multiplier. In the prameterization used here, the normal vectors point away from the origin. This way, the coefficients μ_k have to be positive for the inequality constraints to take effect. The constraint is called active in this case. If one constraining plane is active, the Karush-Kuhn-Tucker conditions require the gradient of the objective function and the normal vectors of the active constraining plane to be parallel (see example in Fig. 4.5). If there are more constraining planes, the gradient has to be part of the cone spanned up by the normal vectors of all constraining planes.

Common methods to solve non-linear optimization problems subject to equality constraints, like attempting to solve the Karush-Kuhn-Tucker conditions directly, which is known as method of Lagrange multipliers [69], do not generalize to optimization problems subject to inequality constraints because it is impossible to know which inequality constraints are active for a given problem instance before solving it. Therefore, alternative methods to find the
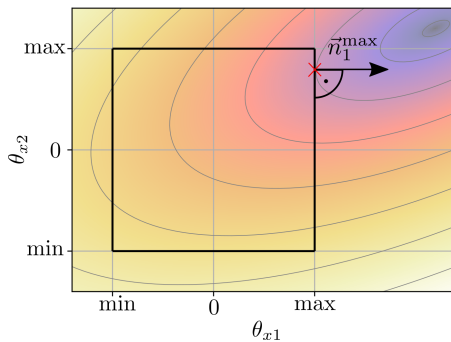
Figure 4.5: Color-coded simulated objective function value of the orbit correction problem (minimum value violet) as a function of the steerer strengths. The black box marks the area that can be reached with the available steerer strength. The unconstrained solution is outside of the constraints putting the constrained solution on the upper constraint of the first steerer strength. There, the constraint is a tangent to the isoline making the gradient of the objective function and the normal vector of the constraining plane parallel. This satisfies the Karush-Kuhn-Tucker conditions.

solution to the constrained orbit correction problem are required. Two methods employed by the SVD-based software, the strategy of orthogonal projections and the strategy of the active set [12], are introduced in the following. Both use an iterative approach to converge to the constrained solution in weighted orbit space. Here, the isolines of the objective are circles and the solution to the constrained orbit correction problem is the point on the active constraining planes that is closest to the unconstrained solution. Both strategies require the unconstrained solution, which is calculated via SVD, as input. As heuristic methods, both strategies suffer from the same theoretical problem: neither can be proven to converge in a finite number of steps or converge at all. In numerical tests with up to five constrained steerer magnets, both strategies, however, found the optimal solution conforming with the Karush-Kuhn-Tucker conditions in about 100 ms in all examined cases.

STRATEGY OF ORTHOGONAL PROJECTIONS

The strategy of orthogonal projections projects the unconstrained solution onto one constraining plane at a time until a solution is found [12]. The criterion for selecting the next plane is the distance of the partially converged solution to the origin within the subspace of remaining active constraining planes. An example of this method is given in Fig. 4.6 (left). In the example, the top and right constraints are active. The strategy of orthogonal projections firstly picks the closest point on the top constraint $\vec{x}_1^*$ because it is closer to the unconstrained solution $\vec{x}^*$ than the closest point on the right constraint. As $\vec{x}_1^*$ is still outside of the right constraint, it is projected onto this constraint in $\vec{x}_2^*$ in a second step. Here, the algorithm stops because no active planes remain.

The strategy of the active set determines where the vector of the unconstrained solution intersects the constraining planes. From there, the strategy follows the constraining planes until it finds the constrained solution. An example of this method is given in Figure 4.6 (right). In the example, the strategy of the active set tracks through the interior of the constrained set towards the unconstrained solution $\vec{x}^*$ until it hits the right constraint in $\vec{x}_1^*$. From here, the strategy follows this now active constraining plane upward. The search ends in the intersection of the top and right constraints in $\vec{x}_2^*$ as this point is the closest point to the unconstrained solution that still adheres to the constraints.
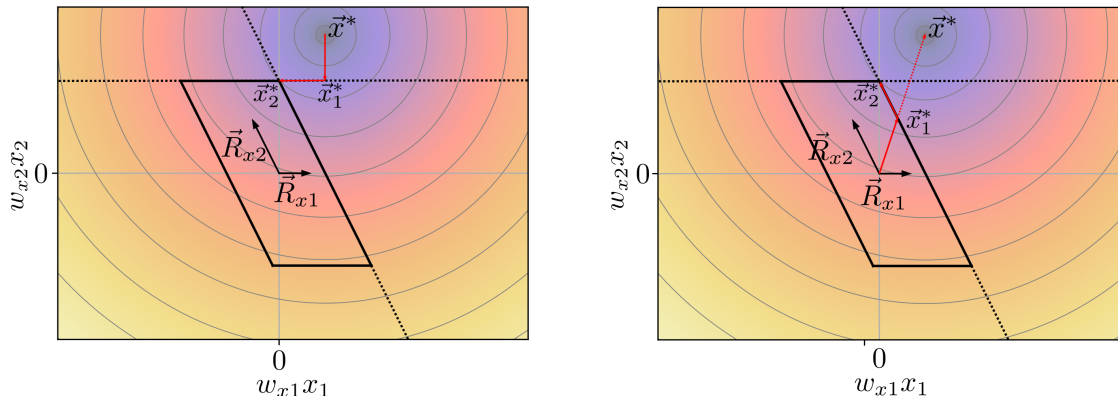
Figure 4.6: Strategy of orthogonal projections (left) and strategy of the active set (right) from [12] demonstrated on the color-coded simulated objective function value (minimum value violet) as a function of the weighted orbit errors for two steerers and two BPMs.

4.4.3 METHOD OF THE MOST EFFECTIVE STEERER MAGNET

One of the earliest automated approaches to orbit correction was the method of the most effective steerer magnet developed at CERN in 1973 [72]. Instead of using all steerer magnets for an orbit correction, this approach only utilizes the single most effective steerer magnet. That steerer magnet is found by solving the orbit correction problem Eq. (4.7) for each steerer separately and then selecting the steerer that performs best for applying the orbit correction. This procedural simplicity also allows to subjugate the solution to inequality steerer strength constraints. Compared to solving the (constrained) orbit correction problem with all steerer magnets, the orbit correction resulting from the method of the most effective steerer magnet is only optimal if the orbit perturbation is caused by a single dipole error with a steerer magnet close-by [14]. In all other cases, orbit correction with this method produces sub-optimal results and leads to non-reproducible steerer strengths. The approach was tested at DELTA [36] but soon replaced by the SVD-based software (see Ch. 4.4.2) due to its shortcomings [12]. Still, the method has one advantage. At DELTA, one of the limiting factors of orbit correction quality is the resolution of the power supplies driving the steerer magnets. As the method of the most effective steerer magnet only uses a single steerer, the applied correction

is larger than the average strength correction per steerer magnet calculated when solving the orbit correction problem with all steerer magnets. The SVD-based and IPM-based correction methods therefore hit the resolution limit earlier than the method of the most effective steerer magnet. The new software (see Ch. 5 for program details) switches to the method of the best steerer magnet below an adjustable WRMS limit that allows it to surpass the orbit correction quality achieved with the SVD-based software (see Ch. 7.1 for an experimental comparison).

5 New Orbit Correction Software

The last Ch. 4 introduced orbit response matrices (ORMs), the weighted root-mean-square (WRMS) of orbit errors and the constrained orbit correction problem as basic building blocks of both orbit correction software generations at DELTA. This chapter focuses on the three modes of orbit and energy correction available in the new software. All modes are built on an interior point method (IPM) for quadratic programs. After Ch. 6 will have presented a proof-of-principle simulation study for one of the energy-correction modes, Ch. 7 provides experimental results for the orbit-correction mode and both energy-correction modes.

5.1 Quadratic Programs

The new software uses an IPM for quadratic programs to solve the orbit correction problem. The advantage of this method is its convergence speed, scalability and built-in acceptance for linear equality and inequality constraints. The constraints are useful to construct additional features like steerer-strength and orbit constraints. The latter are necessary for developing methods for energy correction (see Ch. 5.3). Quadratic programs are a type of convex optimization problem. Their general form is [73]

$$\underset{\vec{\vartheta}}{\text{minimize}} \quad \frac{1}{2}\vec{\vartheta}^{\mathrm{T}}\boldsymbol{Q}\vec{\vartheta} + \vec{q}^{\mathrm{T}}\vec{\vartheta} \tag{5.1}$$

$$\text{subject to} \quad \boldsymbol{A}\vec{\vartheta} = \vec{a} \tag{5.2}$$

$$\boldsymbol{B}\vec{\vartheta} \leq \vec{b} \tag{5.3}$$

where $\vec{\vartheta}$ are the optimization variables and the matrices $\boldsymbol{Q}$, $\boldsymbol{A}$ and $\boldsymbol{B}$ as well as the vectors $\vec{q}$, $\vec{a}$ and $\vec{b}$ contain real numbers. The matrix $\boldsymbol{Q}$ is positive semidefinite.

5.1.1 Interior Point Method

An IPM for quadratic programs is an optimization approach designed to find a solution for Eq. (5.1) by iterating over vectors $\vec{\vartheta}$ stemming from the interior of the feasible set until it finds an optimal vector $\vec{\vartheta}^*$ (see schematic in Fig. 5.1). All possible vectors $\vec{\vartheta}$ satisfying the constraints define the feasible set. The interior of the feasible set excludes its surface. IPMs therefore approximate the solution of an optimization problem if the optimal vector of optimization variables belongs to the surface.

Quadratic programs are a subset of second-order cone programs (SOCPs) because their feasible set can be written as a product of Lorentz cones [74]. General rules for converting a range
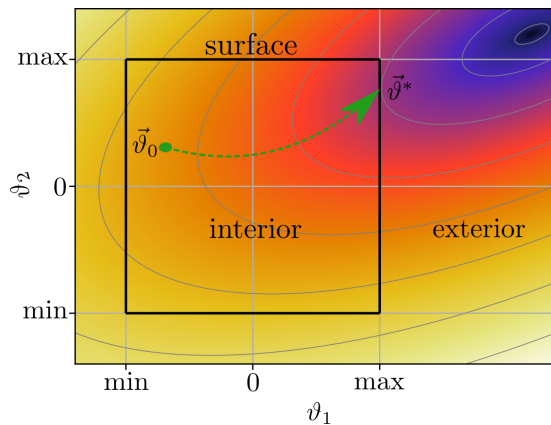
Figure 5.1: Path of an IPM from start $\vec{\vartheta}_0$ to optimum through the color-coded interior of a 2D feasible set (minimum value violet). The surface separates interior and exterior.

of optimization problems to SOCPs can be found in [75]. A simple example is the quadratic program

$$\underset{\vartheta_1, \vartheta_2}{\text{minimize}} \quad \vartheta_1^2 + \vartheta_2^2 \tag{5.4}$$

that is represented by the SOCP

$$\underset{f}{\text{minimize}} \quad f \tag{5.5}$$

$$\text{subject to} \quad \sqrt{\vartheta_1^2 + \vartheta_2^2} \leq f \tag{5.6}$$

with a scalar objective f. The quadratic objective of the original problem is converted to an inequality constraint $\sqrt{\vartheta_1^2 + \vartheta_2^2} \leq f$ equivalent to a Lorentz cone. Figure 5.2 shows a schematic drawing of the feasible set. Similar to linear programs, SOCPs are subjects of a duality theorem: every SOCP has a twin, another optimization problem whose objective determines a lower bound for the objective function of the original optimization problem. Since the original optimization problem is a minimization problem, the twin is a maximization problem. The original problem is called primal. The twin is called dual. If the primal is robust feasible, the dual is robust solvable and vice versa. Any optimization problem with a non-empty feasible set is "feasible". The addition of "robust" demands feasibility of the primal under small perturbations. The property "robust solvable" similarly certifies solvability for the dual under small perturbations.

The method used to solve quadratic programs for applications described in this work is *coneqp* from the `CVXOPT Python` package [76]. It is a primal-dual IPM that exploits the duality of quadratic programs by solving the primal problem and the dual problem simultaneously [77]. This allows *coneqp* to calculate the difference between the objective of the primal and the objective of the dual after each step. The difference is called duality gap and it decreases to zero if optimality is reached. The *coneqp* method encodes the constraints of the primal
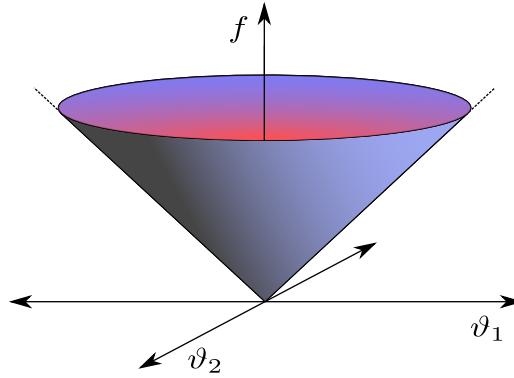
Figure 5.2: A Lorentz cone representing the feasible set of the SOCP example Eq. (5.5).

and the dual problems in their respective objectives with self-concordant logarithmic barrier functions. These allow solving the primal and the dual as unconstrained optimization problems via a Newton approach. With each Newton step, *coneqp* tracks through the interior of the feasible set of both problems along the central path leading from the minimum of the barrier to the minimum of the constrained objective, the sum of the unconstrained objective and the barrier [75]. The influence of the barrier on the constrained objective is controlled by a penalty parameter that decreases step-by-step. Since the logarithmic barrier functions go to infinity if their argument goes to zero, the constraints remain encoded in the constrained objective even if the penalty parameter is very small. The central path is set by the minimum of the constrained objective changing step-by-step. The solver follows the minimum. This approach exploits the local fast convergence of the Newton method. If the duality gap after any Newton step is sufficiently close to zero, *coneqp* terminates. Primal-dual IPMs with self-concordant barrier functions employing the central-path-following scheme, like *coneqp*, increase their target accuracy by a fixed percentage with every step and converge with a small number of iterations almost independent of problem size and data [73]. This makes them a popular choice for solving quadratic programs.

5.2 ORBIT-CORRECTION MODE

The orbit-correction mode estimates the optimal steerer strength corrections $\Delta\vec{\theta}_x^*$ for a horizontal orbit correction Eq. 2.20 and Eq. (2.21) either using the method of the most effective steerer magnet (see Ch. 4.4.3 for details) or via the following two steps:

1. Calculate relative steerer strength corrections $\Delta\vec{\vartheta}^*$ that steer the orbit towards the orbit reference (see Ch. 5.2.1).

2. Calculate new and equally distributed absolute steerer strengths $\vec{\vartheta}^*$ by reshuffling the results of the first step $\vec{\theta}_x + \Delta\vec{\vartheta}^*$ (see Ch. 5.2.2). The final steerer strength corrections are then given by $\Delta\vec{\theta}_x^* = \vec{\vartheta}^* - \vec{\theta}_x$.

The solution retains all features from both individual steps meaning that the orbit is steered towards the orbit reference, unique values are assigned to linearly dependent steerer magnets and steerer-strength as well as orbit-constraints are respected. The method of the best steerer magnet is used if the orbit WRMS is below a certain threshold (program setting). This setup allows to bypass the lower WRMS bound imposed by the resolution of the current sources of the steerer magnets. However, using the method of the best steerer magnet comes at the cost of unreproducible steerer strengths. Also, orbit constraints cannot be used. Both should be acceptable as orbit corrections hardly move the orbit if the WRMS is already small.

The new orbit correction software offers two more modes that add either energy stabilization or path length shortening to the feature list (see Ch. 5.3 for details). A schematic comparison of all modes is shown in Fig. 5.3).

pathway	orbit correction		energy stabilization	orbit shortening
input	$\vec{\theta}_x$	$\vec{\theta}_x$	$\vec{\theta}_x$ & f	$\vec{\theta}_x$ & f
1. step	correct orbit	correct orbit with most eff. steerer	correct orbit & stabilize energy	correct orbit
2. step	distribute steerer strength equally		distribute steerer strength equally	minimize energy
output	$\Delta\vec{\theta}_x^*$	$\Delta\vec{\theta}_x^*$	$\Delta\vec{\theta}_x^*$ & Δf^*	$\Delta\vec{\theta}_x^*$ & Δf^*
unique solution	yes	no	yes	yes
beam energy	varies	varies	constant	minimal
orbit length	varies	varies	constant	minimal

Figure 5.3: An overview of the three modes of the software: the orbit correction mode (blue) introduced in Ch. 5.2 as well as the energy-stabilizing and orbit-shortening modes (green and red) explained in Ch. 5.3. Here, $\vec{\theta}_x$ and f are the steerer strengths and the RF frequency before the orbit correction and $\Delta\vec{\theta}_x^*$ and Δf^* are changes to these quantities.

5.2.1 Method for Correcting the Orbit

Finding a set of relative steerer strength corrections $\Delta\vec{\vartheta}$ that steer the orbit towards the orbit reference requires solving the constrained orbit correction problem Eq. (4.17). Expanding the squared objective function gives

$$\left\lVert \boldsymbol{W}_x\left(\vec{\epsilon}_x + \boldsymbol{R}_x\Delta\vec{\vartheta}\right)\right\rVert_2^2 \tag{5.7}$$

$$= \vec{\varepsilon}_x^{\mathrm{T}}\boldsymbol{W}_x^{\mathrm{T}}\boldsymbol{W}_x\vec{\varepsilon}_x + 2\vec{\varepsilon}_x^{\mathrm{T}}\boldsymbol{W}_x^{\mathrm{T}}\boldsymbol{W}_x\boldsymbol{R}_x\Delta\vec{\vartheta} + \Delta\vec{\vartheta}^{\mathrm{T}}\boldsymbol{R}_x^{\mathrm{T}}\boldsymbol{W}_x^{\mathrm{T}}\boldsymbol{W}_x\boldsymbol{R}_x\Delta\vec{\vartheta}. \tag{5.8}$$

After dropping the constant term $\vec{\varepsilon}_x^{\mathrm{T}} \boldsymbol{W}_x^{\mathrm{T}} \boldsymbol{W}_x \vec{\varepsilon}_x$, the orbit correction problem with the steerer-strength constraints

$$\vec{\theta}_x^{\min} \leq \vec{\theta}_x + \Delta\vec{\vartheta} \leq \vec{\theta}_x^{\max} \tag{5.9}$$

can be parameterized as quadratic program

$$\underset{\Delta\vec{\vartheta}}{\text{minimize}} \quad \vec{\varepsilon}_x^{\mathrm{T}} \boldsymbol{W}_x^{\mathrm{T}} \boldsymbol{W}_x \boldsymbol{R}_x \Delta\vec{\vartheta} + \frac{1}{2}\Delta\vec{\vartheta}^{\mathrm{T}} \boldsymbol{R}_x^{\mathrm{T}} \boldsymbol{W}_x^{\mathrm{T}} \boldsymbol{W}_x \boldsymbol{R}_x \Delta\vec{\vartheta} \tag{5.10}$$

$$\text{subject to} \quad \begin{pmatrix} -\mathbf{1} \\ \mathbf{1} \end{pmatrix} \Delta\vec{\vartheta} \leq \begin{pmatrix} \vec{\theta}_x - \vec{\theta}_x^{\min} \\ -\vec{\theta}_x + \vec{\theta}_x^{\max} \end{pmatrix}. \tag{5.11}$$

The coefficient matrix $\boldsymbol{R}_x^{\mathrm{T}} \boldsymbol{W}_x^{\mathrm{T}} \boldsymbol{W}_x \boldsymbol{R}_x$ is positive definite because it is a product of two matrices, the ORM $\boldsymbol{R}_x$ and the weight matrix $\boldsymbol{W}_x$, with the same property. The objective function is a multi-dimensional parabola in this case. Removing singular values for the purpose of regularization makes the coefficient matrix positive semidefinite and the parabola looses the same number of dimensions. The IPM also allows to add orbit constraints

$$\vec{x}^{\min} \leq \vec{x} + \boldsymbol{R}_x \Delta\vec{\vartheta} \leq \vec{x}^{\max} \tag{5.12}$$

in the equivalent quadratic-program compliant form

$$\begin{pmatrix} -\boldsymbol{R}_x \\ \boldsymbol{R}_x \end{pmatrix} \Delta\vec{\vartheta} \leq \begin{pmatrix} \vec{x} - \vec{x}^{\min} \\ -\vec{x} + \vec{x}^{\max} \end{pmatrix} \tag{5.13}$$

to the orbit correction problem. The constraints model a software aperture that the orbit cannot exceed. A software aperture is useful to limit orbit movements where the range of permitted orbit errors is small. Empirically, this is around BPM23 the case at DELTA. Here, the vacuum chamber heats up if the vertical orbit reference is altered by less than $1\,\mathrm{mm}$ [78]. Using orbit constraints in the orbit correction problem requires the orbit before correction $\vec{x}$ and the software aperture ($\vec{x}^{\min}$, $\vec{x}^{\max}$) as additional inputs.

5.2.2 Method for Distributing Steerer Strengths Equally

Regularization is achieved by removing singular values from the ORM (see part of Ch. 4.4.1 dedicated to regularization). Removing 1 singular value, however, also decreases the rank of the ORM by 1. The more singular values are removed, the more steerer magnets become linearly dependent. At time of writing, 2 and 3 vertical singular values are cut in user operation resulting in 2 horizontal and 3 vertical linearly dependent steerer magnets. These pose a problem because the orbit correction program cannot assign a unique optimal steerer strength to them in an orbit correction. Instead, the optimal steerer strength of these magnets depends on their linearly dependent kin. This behavior can cause steerer strengths of linearly dependent steerer magnets to fluctuate throughout operation which can in turn destabilize orbit. Minimizing the squared steerer strengths $\vec{\vartheta}^{\mathrm{T}}\vec{\vartheta}$ while maintaining the already corrected orbit solves

this problem as steerer strength gets redirected from steerer magnets with large values to those with small values. This leads to steerer strength being distributed equally among linearly dependent steerer magnets. The quadratic program representing the sketched-out approach and that additionally respects the limited range of steerer strengths via inequality constraints is

$$\underset{\vec{\vartheta}}{\text{minimize}} \quad \vec{\vartheta}^{\mathrm{T}} \vec{\vartheta} \tag{5.14}$$

$$\text{subject to} \quad \boldsymbol{R}_x \vec{\vartheta} = \boldsymbol{R}_x \left(\vec{\theta}_x + \Delta\vec{\vartheta}^* \right) \tag{5.15}$$

$$\begin{pmatrix} -\mathbf{1} \\ \mathbf{1} \end{pmatrix} \vec{\vartheta} \leq \begin{pmatrix} -\vec{\theta}_x^{\mathrm{min}} \\ \vec{\theta}_x^{\mathrm{max}} \end{pmatrix}. \tag{5.16}$$

Here, $\Delta\vec{\vartheta}^*$ are the steerer strength corrections resulting from solving minimization problem Eq. (5.10) and $\mathbf{1}$ is a diagonal matrix of 1s.

5.3 Energy-Correction Modes

As explained in Ch. 3.3, the RF frequency, the transverse orbit and the beam energy are related: if the RF frequency or the transverse orbit changes, the beam energy adapts. This dependence can be exploited to correct the beam energy via an SOFB. Altering the RF frequency by Δf changes the beam energy by δ according to Eq. (3.13) and the transverse orbit position by $\delta D_x(s)$, where $D_x(s)$ is the horizontal dispersion function. The dispersive orbit shift makes it possible to treat the RF cavity like a steerer magnet in the orbit correction problem, a steerer that also affects the beam energy. As the energy is not directly measured, only one of two rules may be applied: either maintain the current energy without changing the orbit or find the smallest energy while keeping the orbit changes to a minimum. The latter is equivalent to finding the shortest orbit. Both methods are introduced in the following and build the basis for two additional modes (see Fig. 5.3 for a comparison). The correction method for stabilizing the beam energy (see Ch. 5.3.1) in conjunction with the method distributing steerer strengths equally (see Ch. 5.2.2) together constitute the energy-stabilizing mode. The method determining steerer strengths for orbit corrections (see Ch. 5.2.1) and the method for shortening the orbit (see Ch. 5.3.2) together constitute the orbit-shortening mode.

5.3.1 Method for Stabilizing the Beam Energy

The orbit correction problem can be modified to find steerer strengths that correct both the beam energy and the transverse orbit position [49]. The method was first introduced at the European Synchrotron Radiation Facility (ESRF) where it was used in conjunction with SVD. Since then, similar methods were adopted at KARA (formally ANKA) [79] as well as BESSY II and the MLS [80]. At BESSY II, the energy stabilizing capabilities of this approach are regularly checked via Compton backscattering. A similar method was also implemented in the SVD-based software at DELTA but only partially tested (see discussion below) [12]. The approach layed out in the following takes the original idea from the ESRF and adapts it to the IPM used in the new software by parameterizing it as quadratic program with steerer strength and optional orbit constraints.

Orbit errors may fall under one of three categories requiring the orbit correction software to react differently each time:

1. The orbit errors are dispersive $\vec{\varepsilon}_x \propto \vec{D}_x$ and modulate the orbit length by Δs_r. As Δf is initially zero, this causes an energy shift

$$\delta = \frac{\Delta s_r}{\alpha L} \tag{5.17}$$

according to Eq. (3.13). Here, α is the momentum compation factor and L the circumference of the storage ring. To correct the orbit and the beam energy, the orbit correction software must apply an RF frequency correction Δf^* so that

$$\frac{f}{f + \Delta f^*} - 1 = \frac{\Delta s_r}{L} \tag{5.18}$$

is fulfilled. Then follows $\delta = 0$ and the beam energy remains unchanged.

2. The orbit errors are non-dispersive and do not affect the orbit length and hence the beam energy. Here, the orbit correction software must modulate the steerer strengths according to the solution of the orbit correction problem Eq. (5.10) to correct the orbit.

3. A combination of both.

All three scenarios are covered by solving a modified orbit correction problem

$$\underset{\Delta\vec{\vartheta}, \Delta f}{\text{minimize}} \quad \underbrace{\left\|\vec{\varepsilon}_x + \boldsymbol{R}_x \Delta\vec{\vartheta} + \vec{\mathcal{D}}_x \Delta f\right\|_2^2}_{\text{objective A}} + \underbrace{\sum_{k=1}^{K} \Delta\vartheta_k^2}_{\text{objective B}} \tag{5.19}$$

that can be separated into two objectives. Objective A aims to minimize the orbit errors by redistributing steerer strengths and employing the cavity like a steerer magnet. The steerer strength of the RF cavity is the RF frequency correction Δf that alters the orbit by $\Delta f \vec{\mathcal{D}}_x$. Here, $\vec{\mathcal{D}}_x$ can be interpreted as the orbit response of the cavity. It is proportional to the dispersion function $\vec{\mathcal{D}}_x \propto \vec{D}_x$. Objective B targets minimizing the total steerer strength excluding the RF frequency correction. The combined objective can be summarized as follows: correct the orbit (objective A) while using the RF cavity as much as possible (objective B). If the ORM is a square matrix and has full rank, the cavity orbit response is linearly dependent on the steerer magnets. In this case, the objective A not only decreases to zero but can stay that way even when the steerer strengths are reshuffled by objective B. Both objectives are therefore independent and can be minimized at the same time. That means the steerer magnets alone are used for non-dispersive orbit steering while any dispersive orbit drift is corrected with an appropriate frequency correction. If this energy-stabilizing mode is used on an already corrected orbit, it prevents any further energy drift and thereby effectively "locks in" the beam energy at the time of method activation. The orbit remains corrected as well. Some storage rings are equipped with less steerer magnets than BPMs though. This makes their ORM non-square. The optimization problem Eq. (5.19) can then only be solved in a least-square sense. Potentially, this poses a problem because the cavity might also be used for non-dispersive orbit steering.

The quadratic program representing the modified orbit correction problem with additional steerer-strength constraints is

$$\underset{\Delta\vec{\varphi}}{\text{minimize}} \quad \Delta\vec{u}^{\mathrm{T}}\boldsymbol{R}_{\mathrm{I}}\Delta\vec{\varphi} + \frac{1}{2}\Delta\vec{\varphi}^{\mathrm{T}}\boldsymbol{R}_{\mathrm{I}}^{\mathrm{T}}\boldsymbol{R}_{\mathrm{I}}\Delta\vec{\varphi} \tag{5.20}$$

$$\text{subject to} \quad \begin{pmatrix} -\mathbf{1} \\ \mathbf{1} \end{pmatrix}\Delta\vec{\varphi} \leq \begin{pmatrix} \vec{\varphi} - \vec{\varphi}^{\mathrm{min}} \\ -\vec{\varphi} + \vec{\varphi}^{\mathrm{max}} \end{pmatrix}. \tag{5.21}$$

Here, the RF frequency correction Δf is added to the optimization variables

$$\Delta\vec{\varphi} = (\Delta\vartheta_1, \cdots, \Delta\vartheta_{K_x}, \Delta f)^{\mathrm{T}} \tag{5.22}$$

requiring the current RF frequency f and optionally some RF frequency limits f^{min} and f^{max} to be appended the current steerer strengths $\vec{\theta}_x$ and their constraints $\vec{\theta}_x^{\mathrm{min}}$ and $\vec{\theta}_x^{\mathrm{max}}$ resulting in $\vec{\varphi}$, $\vec{\varphi}^{\mathrm{min}}$ and $\vec{\varphi}^{\mathrm{max}}$. The ORM is extended by an additional column and an additional row yielding

$$\boldsymbol{R}_{\mathrm{I}} = \begin{pmatrix} & & & \mathcal{D}_{x1} \\ & \boldsymbol{R}_x & & \vdots \\ & & & \mathcal{D}_{xJ} \\ 1 & \cdots & 1 & 0 \end{pmatrix}. \tag{5.23}$$

The changed dimensions of the ORM $\boldsymbol{R}_{\mathrm{I}}$ make it necessary to append a 0 to the vector of orbit errors

$$\Delta\vec{u} = (\Delta\varepsilon_{x1}, \cdots, \Delta\varepsilon_{xJ}, 0)^{\mathrm{T}}. \tag{5.24}$$

The energy-stabilization enhanced orbit correction problem Eq. (5.20) can be used interchangeably with the standard orbit correction problem Eq. (5.10) and is compatible with the method introduced in Ch. 5.2.2 to distribute steerer strengths equally. Similarly to the standard problem, the modified model can be supplemented with orbit constraints to include a software aperture.

DISCUSSION

DELTA does not fit the method template. The reason is that the storage ring is equipped with less BPMS (see Ch. 2.2.2) than horizontal steerer magnets (see Ch. 2.2.3): the ratio is $J = 54$ by $K_x = 30$. This gives the unregularized horizontal ORM a rank of 30 while the rank of the ideal square full-rank matrix is 54. DELTA therefore requires 14 additional steerers to fulfill the requirements of the energy-stabilizing mode. Still, the fact that KARA employs a very similar method [79] with 40 BPMs [81] and 28 horizontal steerer magnets [82] points to the ratio not being too important. An initial measurement presented in Ch. 7.2 indicates that the energy-stabilizing mode without BPM weights also works at DELTA. The weights (see Ch. 4.3) pose another problem. If they are included in Eq. (5.19) (requires multiplying the

equation with the weight matrix $\boldsymbol{W}_x$), the method produces a different frequency correction than without weights. This was numerically tested. Experimentally, this makes the orbit-stabilizing mode with weights unusable: the orbit correction software just increases/decreases the RF frequency until the beam is lost. Previous tests of a similar method in the SVD-based program probably have encountered the same weight-related issue because the RF frequency and steerer strengths diverged back then as well [12]. An idea to remove the weights and make the energy-stabilizing mode work in user operation is discussed in the outlook in Ch. 12.2.

5.3.2 Method for Shortening the Orbit

The method finding unique settings for linearly dependent steerer magnets (see Ch. 5.2.2) is modified in the following to additionally adjust the beam energy and find the shortest orbit that fits the orbit reference. It works by minimizing the total steerer strength at the cost of increasing the RF frequency correction via an optimization problem

$$\underset{\vec{\vartheta},\,\Delta f}{\text{minimize}} \quad \sum_{k=1}^{K} \vartheta_k^2 \qquad (5.25)$$

$$\text{subject to} \quad \boldsymbol{R}_x \vec{\theta}_x + \vec{\mathcal{D}}_x \Delta f = \boldsymbol{R}_x \left(\vec{\theta}_x + \Delta \vec{\vartheta}^* \right). \qquad (5.26)$$

The already corrected orbit is kept stationary. In this form, the method to shorten the orbit only works if the ORM is a square matrix with full rank making the frequency response linearly dependent on the steerer magnets. Then, the steerer strengths and the RF frequency correction can be reshuffled without affecting the BPM readings. For an operator, only the reduction in overall steerer strengths $|\vec{\theta}|$ is visible when the method is used. Figure 5.4 shows a schematic of the described effect.
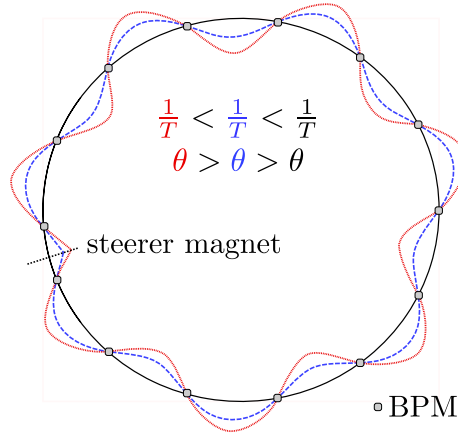
Figure 5.4: Three orbits with different revolution frequencies $1/T$ but the same BPM readings: a long orbit (red), a shorter orbit (blue) and the shortest orbit (black). The latter is also the ideal orbit. All orbits receive a different kick θ from a steerer magnet. Given the different lengths of all orbits, the RF frequency corresponding to each orbit is different as well.

The orbit-shortening mode can be adapted to storage rings with less steerer magnets than BPMs by replacing the equality orbit constraints with inequality orbit constraints

$$\boldsymbol{R}_x \left(\vec{\theta}_x + \Delta \vec{\vartheta}^* \right) - \frac{1}{2} \Delta \vec{x}_{\mathrm{b}} \leq \boldsymbol{R}_{\mathrm{II}} \vec{\varphi} \leq \boldsymbol{R}_x \left(\vec{\theta}_x + \Delta \vec{\vartheta}^* \right) + \frac{1}{2} \Delta \vec{x}_{\mathrm{b}} \qquad (5.27)$$

that keep the orbit within a thin band of

$$\Delta \vec{x}_{\mathrm{b}} = \frac{\Delta \vec{x}_{\mathrm{b}}^{\max}}{\text{diag}(\boldsymbol{W})} \qquad (5.28)$$

around the corrected orbit. This modification makes it possible to deploy the orbit-shortening mode at DELTA. The maximum width of the band is given by a vector of empiric values

$$\Delta \vec{x}_{\mathrm{b}}^{\mathrm{max}} = (100\,\mu\mathrm{m}, \cdots, 100\,\mu\mathrm{m})^{\mathrm{T}} \tag{5.29}$$

that worked well in a simulation and an experimental study (see Ch. 6 and Ch. 7.3). The width scales inversely with the BPM weight keeping the orbit at more important BPMs more stable. An unwanted side effect of the inequality constraints is the introduction of orbit noise. The quadratic program representing the optimization problem with additional steerer-strength constraints is

$$\underset{\vec{\varphi}}{\text{minimize}} \quad \vec{\varphi}^{\mathrm{T}} \boldsymbol{Q}_{\mathrm{II}} \vec{\varphi} \tag{5.30}$$

$$\text{subject to} \quad \begin{pmatrix} \mathbf{1} \\ -\mathbf{1} \\ \boldsymbol{R}_{\mathrm{II}} \\ -\boldsymbol{R}_{\mathrm{II}} \end{pmatrix} \cdot \vec{\varphi} \leq \begin{pmatrix} \vec{\varphi}_{\mathrm{max}} \\ -\vec{\varphi}_{\mathrm{min}} \\ \boldsymbol{R}_x \left(\vec{\theta}_x + \Delta \vec{\vartheta}^* \right) + \frac{1}{2} \Delta \vec{x}_{\mathrm{b}} \\ -\boldsymbol{R}_x \left(\vec{\theta}_x + \Delta \vec{\vartheta}^* \right) + \frac{1}{2} \Delta \vec{x}_{\mathrm{b}} \end{pmatrix}. \tag{5.31}$$

The RF frequency correction Δf is added to the optimization variables

$$\vec{\varphi} = (\vartheta_1, \cdots, \vartheta_{K_x}, \Delta f)^{\mathrm{T}} \tag{5.32}$$

and the ORM is extended by adding the frequency response $\mathcal{D}_x$ as an additional column

$$\boldsymbol{R}_{\mathrm{II}} = \begin{pmatrix} & & \mathcal{D}_{x1} \\ & \boldsymbol{R}_x & \vdots \\ & & \mathcal{D}_{xJ} \end{pmatrix}.$$

The diagonal matrix

$$\boldsymbol{Q}_{\mathrm{II}} = \mathrm{diag}(1, \cdots, 1, 0) \tag{5.33}$$

contains ones and a single zero in the end to minimize the summed squares of all optimization variables except the RF frequency correction.

6 Testing the Orbit-Shortening Mode in a Simulation

The orbit-shortening mode introduced in Ch. 5.3.2 is tested in a simulation to demonstrate that it finds the shortest orbit for an orbit reference. The simulation is an improved version of [50].

6.1 Simulation

The simulation is based on a simple model of the storage ring at DELTA implemented in `Python` that tracks how variations of the RF frequency and the steerer strengths affect the beam energy and the horizontal closed orbit. Among other data, the simulation uses optical functions from the `MADX` [83] *del008.2001* [34] lattice model as input (see Ch. 2.4 for details on the model). The `PyMad Python` package [84] is used as `MADX-Python` interface. The `MADX-Python` hybrid approach is necessary to simulate a closed orbit that reflects changes of the RF frequency as dispersive orbit drifts. `MADX` and other optics codes such as `Elegant` [85] and the `polymorphic tracking code` (PTC) [86] ignore this phenomenon. The version of the storage ring model used to generate results for this work improves on [50] by approximating the curvature of the closed orbit in quadrupoles better. The enhanced simulation cuts the magnets into slices and calculates a trajectory for every slice. This improves the path length calculation when passing the quadrupoles off-center and resulted in a notable reduction of frequency and energy oscillations while using the orbit-shortening mode in the simulated environment. The `Python` model of the storage ring provides a simulated horizontal orbit

$$\vec{x}^{\mathrm{a}} = \boldsymbol{R}_x^{\mathrm{a}} \vec{\theta}_x + \vec{D}_x^{\mathrm{a}} \delta \tag{6.1}$$

at all BPMs to be accessed by the orbit-shortening mode. The model incorporates transverse orbit effects from two sources: orbit displacements induced by the steerer magnets and dispersive orbit changes caused by the RF cavity. The orbit displacements from the steerer magnets $\boldsymbol{R}_x^{\mathrm{a}} \vec{\theta}_x$ are determined by a vector of steerer strengths $\vec{\theta}_x$ and an ORM $\boldsymbol{R}_x^{\mathrm{a}}$. The matrix is calculated via the BE model Eq. (3.10) with analytical steerer parameters given by Eq. (14.13) from Twiss parameter output of the `MADX` Twiss module. The dispersive orbit changes $\vec{D}_x^{\mathrm{a}} \delta$ are given by the product of the energy deviation δ and the dispersion function $\vec{D}_x^{\mathrm{a}}$ that is also supplied by the `MADX` Twiss module. The energy deviation is determined by the length of the orbit. Therefore, it depends on the steerer strengths and the RF frequency. Whenever the

steerer strengths or the RF frequency change, the energy deviation needs to be recalculated numerically in `Python`.
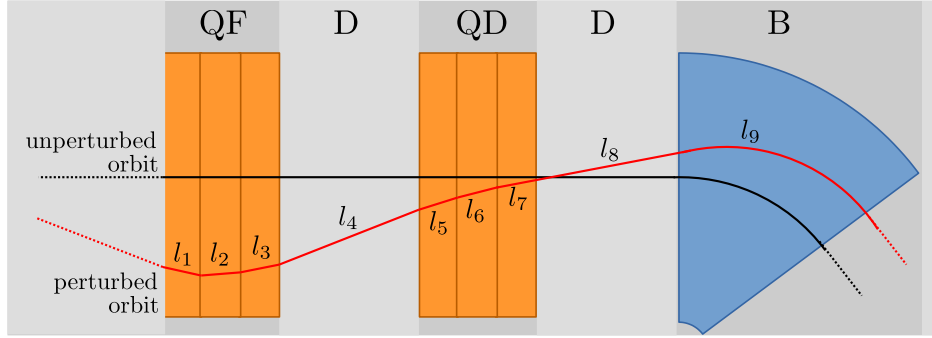
Figure 6.1: Part of the perturbed (red) and the unperturbed orbit (black). The orbit length of the perturbed orbit is the sum over the orbit lengths in all elements.

6.1.1 CALCULATING THE BEAM ENERGY

The energy deviation, the RF frequency and the orbit length are related according to Eq. (3.13) that is reformulated as

$$\frac{f}{f + \Delta f} - 1 = \frac{\Delta s_{\delta r}(\delta, \vec{\theta}_x)}{L} \tag{6.2}$$

by introducing a total orbit length variation

$$\Delta s_{\delta r}(\delta, \vec{\theta}_x) = L_1(\delta, \vec{\theta}_x) - L \tag{6.3}$$

where L is the length of the design orbit and $L_1(\delta, \vec{\theta}_x)$ is the length of the perturbed orbit. It sums up the effect of the steerer magnets and the RF cavity on the orbit. The length of the perturbed orbit is calculated numerically from an extended transverse orbit

$$\vec{x}^{\rm b} = \boldsymbol{R}_x^{\rm b}\vec{\theta}_x + \vec{D}_x^{\rm b}\delta, \tag{6.4}$$

a superset of $\vec{x}^{\rm a}$ that additionally contains the horizontal orbit positions at the entries of all drift spaces, quadrupoles, bending magnets and the RF cavity. The quantities $\boldsymbol{R}_x^{\rm b}$ and $\vec{D}_x^{\rm b}$ are the ORM and the dispersion vector from the `MADX` Twiss module corresponding to the superset. The length calculation iterates over all elements of the lattice adding up the distance between horizontal orbit position at the entry and exit of each element in a two dimensional coordinate system

$$L_1(\delta, \vec{\theta}_x) = \sum_i l_i(\delta, \vec{\theta}_x). \tag{6.5}$$

Figure 6.1 demonstrates the relation of the element lengths and the orbit lengths. Quadrupoles are subdivided into multiple parts to better capture the curved trajectory in the magnet. The

beam path in dipole magnets is calculated as circular trajectory. Whenever the RF frequency or the steerer strengths change, the `Python` storage ring model solves Eq. (6.2) numerically for the energy deviation by minimizing

$$\min_{\delta} \quad \left| \frac{f}{f + \Delta f} - 1 - \frac{\Delta s(\delta, \vec{\theta}_x)}{L} \right|^2. \tag{6.6}$$

This requires iterating the following steps:

1. update δ;

2. calculate closed orbit;

3. calculate resulting orbit length variation $\Delta s(\delta, \vec{\theta}_x)$ and

4. test if δ solves the minimization problem Eq. (6.6). Start over if not.

6.2 Test Setup

The orbit-shortening mode was tested by collecting statistical convergence data on the storage ring model. For each run, the storage ring model was perturbed with equally distributed random steerer strengths $\vec{\theta}_x \in [-0.1\,\mathrm{mrad}, 0.1\,\mathrm{mrad}]$ and a constant RF frequency variation $\Delta f = 5\,\mathrm{kHz}$. The orbit-shortening mode was then executed 100 times. After each step, the resulting steerer strength corrections $\Delta\vec{\theta}_x^*$ were applied with a step size of $\eta = 0.7$ according to Eq. (2.20) to correct the orbit towards the reference, the unperturbed orbit. The stepsize was selected empirically (see Ch. 2.3 for details). Ideally, the correction scheme should reduce all steerer strengths and the frequency deviation back to zero while doing so, because the shortest orbit is the orbit reference itself (see Ch. 5.3.2 on further explanations on the orbit shortening mode). To calculate the orbit WRMS, real weights from a reference file were used.

6.3 Test Results

The evolution of the control variable of the correction scheme, the orbit WRMS, and the evolution of the sum of the absolute steerer strengths $\overline{|\vec{\theta}_x|}$ for each of the 100 steps are presented in Fig. 6.2. The evolution of the energy deviation δ and the evolution of the RF frequency shift Δf are given in Fig. 6.3.

The orbit WRMS according to Eq. (4.3) encodes the weighted distance between the orbit and the reference. The large initial peak is caused by the initial perturbation of the RF frequency and the steerer strengths that drive the orbit away from the orbit reference. Over several steps, the WRMS decreases which signals an increasing match of orbit and orbit reference. An orbit WRMS of zero means that the orbit and the reference are identical. After about 10 steps, the orbit WRMS is close to zero. The absolute steerer strengths and the RF frequency deviation take about 25 steps to be corrected. The energy deviation moves similarly to the RF frequency deviation. It underlines why the orbit-shortening mode is categorized as energy
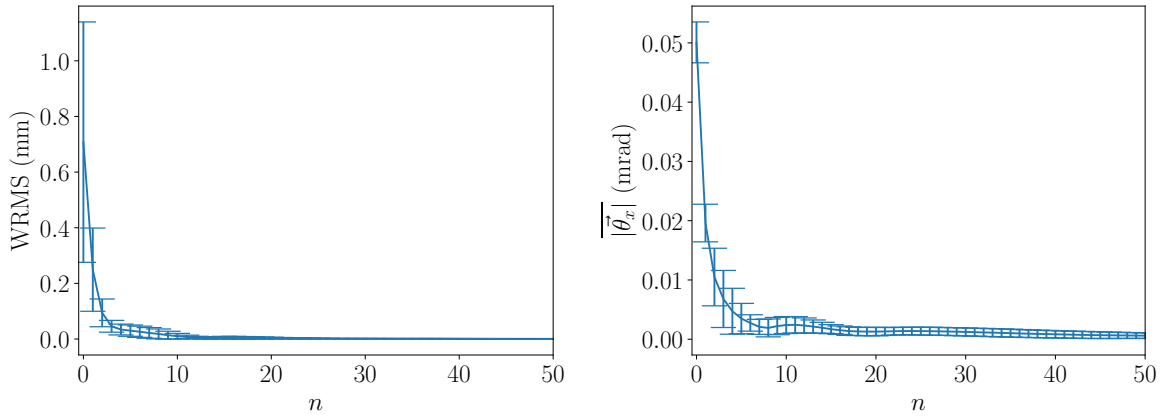
Figure 6.2: Evolution of the average orbit WRMS (left) and the average absolute steerer strengths $\overline{|\vec{\theta}_x|}$ (right) of the storage ring model across 100 applications of the orbit-shortening mode. The error bars mark the standard deviation of both quantities.

correction scheme. When decreasing the RF frequency, the orbit correction software increases the beam energy.

All in all, the orbit-shortening mode corrects the orbit and (in this case) increases the orbit length as intended. The correction process consists of two phases. In the first phase up to step 10, orbit and energy correction are applied together. The second phase from step 10 to step 25 only constitutes energy correction. Here, the steerer strengths and the RF frequency deviation are reshuffled without changing the orbit much. The number of steps required to converge is similar across all runs. The convergence time is therefore mostly independent of the initial steerer-strength perturbation.
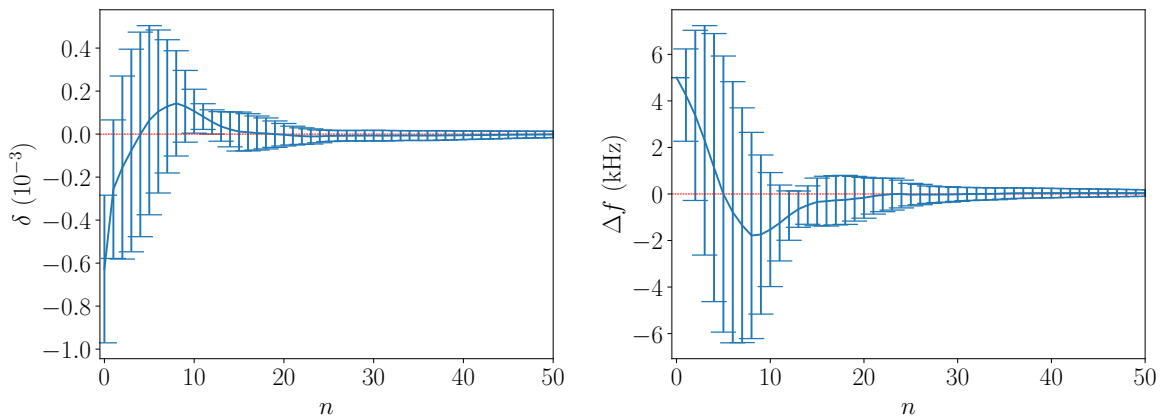
Figure 6.3: Evolution of the average energy shift δ (left) and the average frequency shift Δf (right) of the storage ring model across 100 applications of the orbit-shortening mode. The error bars mark the standard deviation of both quantities.

7 Experimental Tests of the New Orbit Correction Software

The new IPM-based orbit correction software was introduced in Ch. 5. After its orbit-shortening mode was already shown to work in a simulation in Ch. 6, this Chapter presents experimental results for the orbit-correction mode, the energy-stabilizing mode and also the orbit-shortening mode. A summary and an outlook can be found in the final Ch. 12.

7.1 Comparison with its Predecessor

The orbit stability is characterized by the minimum WRMS reached with the SOFB and the evolution of this state over time as it is impeded by thermal movements of the vacuum chamber and magnetic field errors. The orbit stabilities offered by the the SVD-based software and the new IPM-based software were compared in 2020 when the old superconducting wiggler SAW (see Ch. 2.2.1 for details) was still in operation. The magnetic fields of the SAW applied a net horizontal kick to the beam proportional to its field strength. In contrast to the new SCW, the superconducting coils of the SAW were not permanently connected to its power supplies and had to be actively recharged every 12 to 24 hours. Between these events, the magnetic field strength of the wiggler and its net horizontal kick decreased and distorted the orbit. In user operation, correcting the resulting orbit drift was an important duty of the SOFB. The performances of the SVD-based software and the IPM-based software were monitored in this environment with the SAW in two consecutive measurements. Both software generations used the same ORM and the same orbit reference.

7.1.1 Results

The results for the orbit WRMS are given in Fig. 7.1 for the old and and Fig. 7.2 for the new software. Both software generations achieve a good orbit stability during SAW operation. The average orbit WRMS (see Ch. 4.3 for an explanation) of the old software is

$$\overline{\mathrm{WRMS}}_x^{\mathrm{old}} = 2.1\,\mathrm{mm} \pm 1.1\,\mathrm{mm} \tag{7.1}$$

in the horizontal plane and

$$\overline{\mathrm{WRMS}}_y^{\mathrm{old}} = 1.0\,\mathrm{mm} \pm 0.3\,\mathrm{mm} \tag{7.2}$$
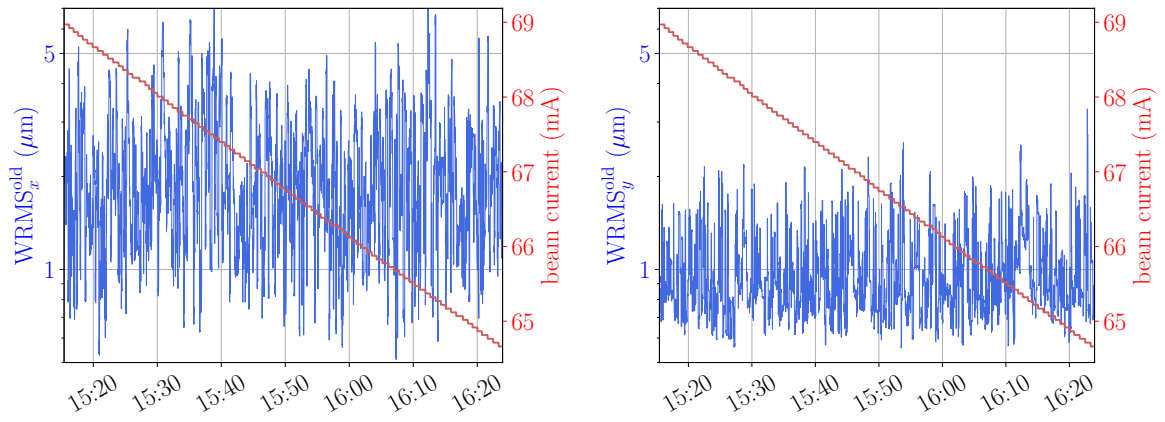
Figure 7.1: Horizontal orbit WRMS (left: blue), vertical orbit WRMS (right: blue) and beam current (red) during SAW operation for the old SVD-based software.
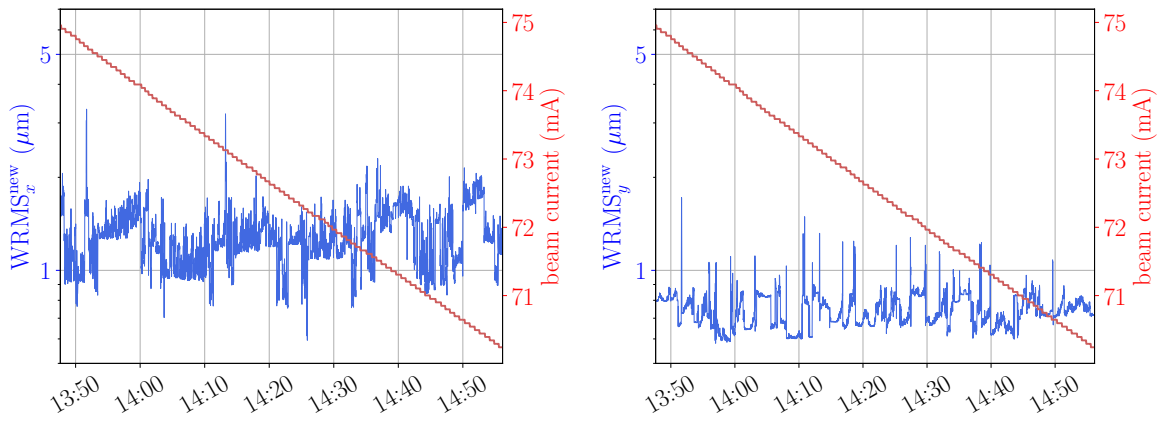
Figure 7.2: Horizontal orbit WRMS (left: blue), vertical orbit WRMS (right: blue) and beam current (red) during SAW operation for the new IPM-based software.

in the vertical plane. The errors are standard deviations. For the BPMs with the largest weights (≈ 1100 in the injection area and around the U55), the averages translate to orbit errors of less than $3\,\mu m$ in the horizontal plane and $1\,\mu m$ in the vertical plane that are already below the resolution of the Bergoz MX BPMs of $5\,\mu m$ (see Ch. 2.2.2 for an introduction). This is possible because some of the BPMs with large weights in the straight sections are equipped with Libera Electrons read-out electronics that reach a smaller resolution $<1\,\mu m$. The average WRMS achieved by the new software is even smaller reaching

$$\overline{\mathrm{WRMS}}_x^{\mathrm{new}} = 1.3\,\mathrm{mm} \pm 0.3\,\mathrm{mm} \tag{7.3}$$

in the horizontal plane and

$$\overline{\mathrm{WRMS}}_y^{\mathrm{new}} = 0.7\,\mathrm{mm} \pm 0.1\,\mathrm{mm} \tag{7.4}$$

in the vertical plane. The smaller minima come from switching to the method of the most effective steerer magnet when the WRMS is already small (see Ch. 4.4.3 for details). Storage rings usually target a beam stability within 1/10th of their beam size [87][88][89]. A comparison of the beam size and the orbit stabilities reached with both software generations in DELTA's three insertion devices in Tab. 7.1 shows that both programs yield similar results. In the undulator U55, the orbit stability is well below 1/10th of the beam size. The size in the U250 is about right. Only the orbit in the SAW moves more. This is not a problem as the wiggler emits synchrotron radiation in a large enough cone. It even serves three beamlines at once (see Fig. 2.4 for a top-up view of the accelerator complex).

name	$\overline{\beta_x}$	$\sqrt{\varepsilon_x \overline{\beta_x}}$	w_x	$\overline{\mathrm{WRMS}}_x^{\mathrm{old}}/w_x$	$\overline{\mathrm{WRMS}}_x^{\mathrm{new}}/w_x$
U250	$3\,\mathrm{m}$	$212\,\mu m$	100	$21\,\mu m \pm 11\,\mu m$	$13\,\mu m \pm 3\,\mu m$
SAW	$10\,\mathrm{m}$	$378\,\mu m$	1	$2100\,\mu m \pm 1100\,\mu m$	$1300\,\mu m \pm 300\,\mu m$
U55	$10\,\mathrm{m}$	$378\,\mu m$	1100	$<3\,\mu m$	$<2\,\mu m$

Table 7.1: Comparison of the average horizontal beta function $\overline{\beta_x}$, the beam size $\sqrt{\varepsilon_x \overline{\beta_x}}$, the horizontal weight w_x and the orbit stabilities reached with the SVD-based software and the new IPM-based software $\overline{\mathrm{WRMS}}_x^{\mathrm{old}}/w_x$ and $\overline{\mathrm{WRMS}}_x^{\mathrm{new}}/w_x$. The horizontal emittance of DELTA is $\varepsilon_x = 15\,\mathrm{nm\,rad}$ (see Tab. 2.1).
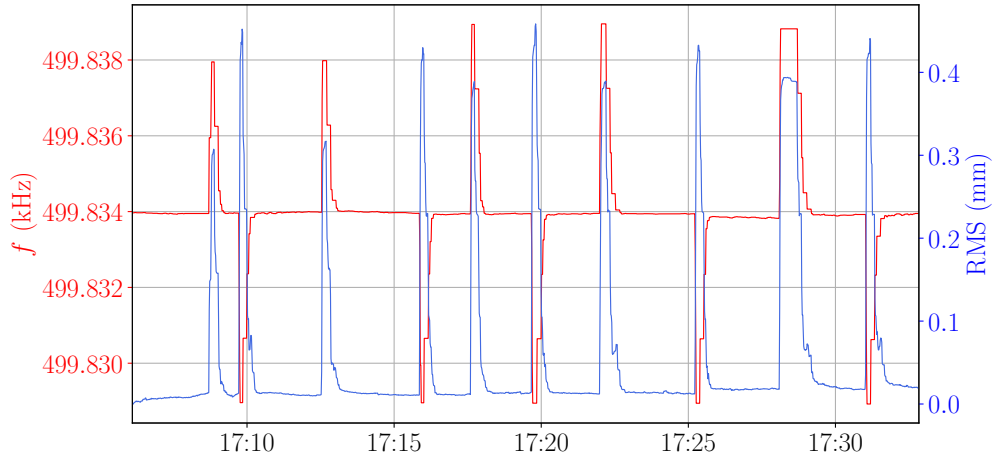
Figure 7.3: Measured RF frequency f and orbit RMS (same as orbit WRMS Eq. 4.3 but without the weight matrix) over time while using the energy-stabilizing mode. Source: scaled plot from [50].

7.2 ENERGY STABILIZATION

At time of writing, DELTA is not equipped with an experimental setup to measure the beam energy. It is therefore not possible to evaluate the energy-stabilizing mode comprehensively in an experiment. Still, it is possible to conduct a proof-of-principle measurement validating the implementation [50]. This was done by firstly selecting the current orbit as orbit reference in the new orbit correction software and reducing all weights to 1 (see discussion in Ch. 5.3.1 for an explanation), secondly perturbing the RF frequency by up to ± 5 kHz and thirdly correcting the orbit with the energy-stabilizing mode. According to Eq. (3.13), altering the frequency also results in an energy shift. Correcting this energy shift requires the SOFB to remove the frequency shift without using the steerer magnets. Results of several iterations of this test are shown in Fig. 7.3. When the RF frequency is perturbed, the orbit RMS (same as the orbit WRMS Eq. 4.3 but without the weight matrix) increases. The energy-stabilizing mode reacts as expected: it corrects the orbit without using the steerer magnets and returns the RF frequency to an average of

$$499\,833.94 \,\text{kHz} \pm 0.04 \,\text{kHz}, \tag{7.5}$$

where the uncertainty is the standard deviation. The result is very close to the RF frequency of DELTA in user operation $499\,834$ kHz (see Tab. 2.1).

7.3 MINIMIZING THE ORBIT LENGTH

After the orbit-shortening mode (see Ch. 5.3.2 for details) was validated in a simulation in Ch. 6, it is experimentally evaluated in the following. The experimental data was already shown in [50]. Firstly, the orbit-shortening mode was applied to the orbit in user optics. The results are shown in Fig. 7.4. The orbit correction increases the RF frequency until it converges at about $499\,835.24\,\text{kHz}$ while decreasing the total currents of all K_x horizontal steerer magnets

$$I_x^{\text{sum}} = \sum_{k=1}^{K_x} |I_{xk}|, \tag{7.6}$$

where I_{xk} is the current of a single steerer, by about $4.5\,\%$. The currents are used as a proxy for the steerer strengths here as both are closely related. During the measurement, the orbit WRMS fluctuates but remains small. This illustrates the working principle of the orbit-shortening mode: replace as much steerer currents (steerer strengths) with an RF frequency shift as possible without altering the orbit.
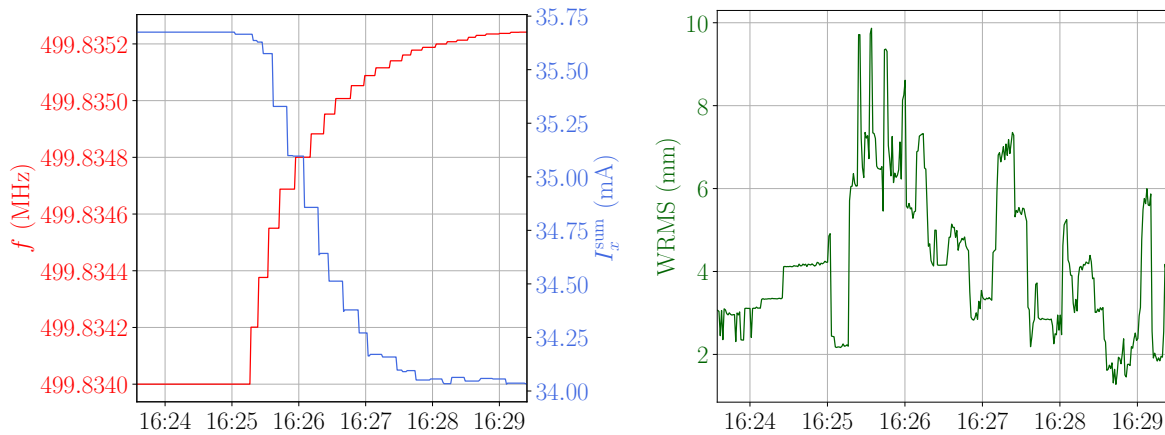
Figure 7.4: Measured RF frequency f and total horizontal steerer currents Eq. (7.6) (left) as well as the orbit WRMS (right) over time while using the orbit-shortening mode in user operation. Source: scaled plots from [50].

Secondly, the orbit-shortening mode was used to assist switching between user optics and machine-study optics (see Ch. 2.2.5 for DELTA's modes of operation). Switching optics requires to firstly remove the static orbit bump that brings the orbit closer to the injection septum in user operation. Secondly, the orbit and its length need to be corrected while the betatron tunes are kept constant by the tune correction program [43] (see Ch. 2.2.4 for details). Toggling of orbit corrections and changes to the RF frequency needed to be controlled manually until recently. The orbit-shortening mode now automates this part of the process as the measurement presented in Fig. 7.5 shows. The Figure displays the evolution of the RF

frequency and the total horizontal steerer currents Eq. (7.6) during optics switching. Initially, the storage ring is in machine-study optics. Here, the average RF frequency is

$$499\,817.65 \,\text{kHz} \pm 0.02 \,\text{kHz}. \tag{7.7}$$

The uncertainty marks the standard deviation. The reference orbit is then switched to user optics (orbit and weights from a reference file) and the orbit bump is manually activated step-by-step while the orbit-correction mode and the tune correction are working. The RF frequency then slowly rises until the storage ring reaches user optics where the average RF frequency is

$$499\,835.38 \,\text{kHz} \pm 0.01 \,\text{kHz}. \tag{7.8}$$

Next, the orbit reference is set to machine-study optics again (orbit and weights from the reference file but with nulled orbit reference and weights set to 1 in the injection area) and the orbit bump is removed step-by-step while the orbit-shortening mode and the tune correction are working again. The switching process is repeated two and a half times in total until the storage ring ends up in machine-study optics. The ideal RF frequencies of both optics settings are reproduced well after each switch. Counter-intuitively, the optimal orbit length decreases (RF frequency increases) when the static orbit bump is activated and increases when it is deactivated. The reason is that the bump needs to cut the design orbit short to bring the orbit closer to the injection septum on the inside of the storage ring (see Fig. 2.4 for an overview of the accelerator complex). The total horizontal steerer currents behave as expected. They peak while the orbit switching is conducted and rest at local minima once the correction has converged. Without bump, the total horizontal steerer currents are about 30 % smaller. This indicates that the SOFB in user operation corrects orbit perturbations resulting from the bump or supports the bump-specific dipole magnets in upholding the bump.
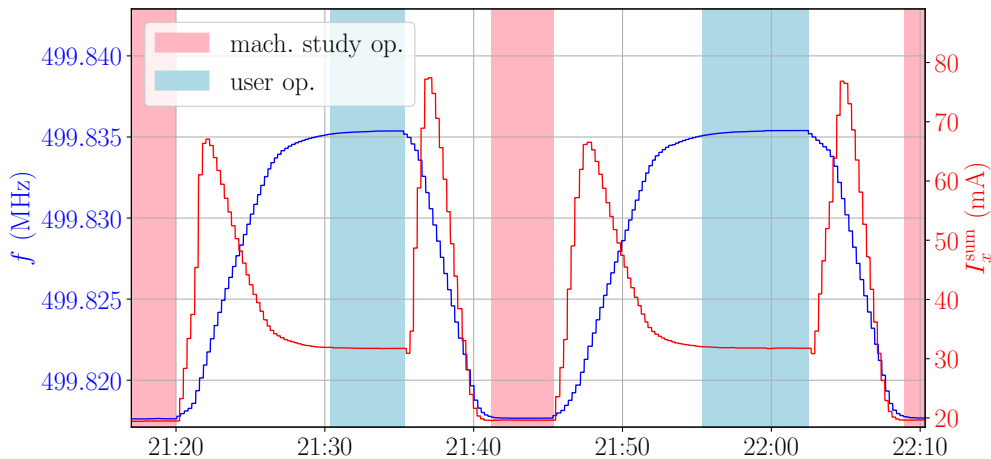
Figure 7.5: Measured RF frequency f and total horizontal steerer currents Eq. (7.6) over time while using the orbit-shortening mode for optics switching. The optics setting is marked by the background color. Source: modified plot excerpt from [50].

8 The Closed-Orbit Bilinear-Exponential Analysis Algorithm

After the introductions to the theory of coupled betatron oscillations in Ch. 3.1 as well as to the BE orbit response model in Ch. 3.2.1 and to the BE+d model in Ch. 3.3, the following description of the COBEA algorithm builds the basis for understanding the response set fit algorithm (RSFA) in Ch. 9. Both algorithms are compared in simulation studies in Ch. 10.

8.1 Prequisites

COBEA decomposes an ORM into coupled beta functions, betatron phase advances and scaled dispersion values at all BPMs. The algorithm is described in [13]. Apart from the matrix, COBEA only requires the ordering of BPMs and steerer magnets along the beam path and the length of a single drift space between two BPMs as input. The algorithm works in three consecutive steps, called layers. The first layer described in Ch. 8.2 prepares start values for the phasors which are the coupled beta functions, the coupled betatron phases and the betatron tunes. The second layer fits the BE+d model to the ORM which is explained in Ch. 8.3. The fit extracts dispersion information and further enhances estimates for the coupled beta functions and the coupled betatron phase advances. The third layer is outlined in Ch. 8.4. It postprocesses the fit results by calculating betatron phase, integer tunes and fit uncertainties. COBEA requires a coupled ORM

$$\boldsymbol{R} = \begin{pmatrix} \boldsymbol{R}_x & \boldsymbol{R}_{xy} \\ \boldsymbol{R}_{yx} & \boldsymbol{R}_y \end{pmatrix} \tag{8.1}$$

as input. The submatrices $\boldsymbol{R}_x$ and $\boldsymbol{R}_y$ are the same decoupled matrices used in both orbit correction software generations at DELTA (see Ch. 4.2 for an explanation). The coupling terms $\boldsymbol{R}_{xy}$ and $\boldsymbol{R}_{yx}$ contain the orbit responses of the vertical steerer magnets in the horizontal plane and the horizontal steerer magnets in the vertical plane. They make it possible to fit the coupled optical functions. The entries of the coupled ORM are R_{wjk}, where the $W = 2$ planes are indexed by $w = 1\text{-}2$, J BPMs are indexed by $j = 1, \cdots, J$ and all $K = K_x + K_y$ (horizontal + vertical) steerer magnets are indexed by $k = 1, \cdots, K$. In the start value layer,

COBEA models the ORM entries using the discretized spatial part of the BE model Eq. (3.10) with separate complex scaling factors A_{mk} called steerer parameters for all steerer magnets

$$R_{wjk}^{\text{BE}} = \sum_{m=1}^{M} \Re\{A_{mk}E_{mjk}Z_{mwj}\}. \tag{8.2}$$

In the fit layer, the discretized spatial part of the BE+d model Eq. (3.15) with scaled energy deviations $b_k \propto \delta_k$

$$R_{wjk}^{\text{BE+d}} = \sum_{m=1}^{M} \Re\{A_{mk}E_{mjk}Z_{mwj}\} + d_{wj}b_k \tag{8.3}$$

is used instead. Here, $m = 1\text{-}2$ indexes the $M = 2$ modes of coupled betatron motion. In both models, the phasors $Z_{mwj} = Z_{mw}(s_j)$ refer to the discretized spatial components of the propagated eigenvectors Eq. (3.7). They are composed of the coupled beta functions and the coupled betatron phases. The scaled dispersion values d_{wj} are proportional to the dispersion functions of the horizontal and vertical plane $d_{1j} \propto D_x(s_j)$ and $d_{2j} \propto D_y(s_j)$. The scaled energy deviations are steerer-specific because the orbit response of each steerer impacts the orbit length and hence the beam energy in a different way. In contrast to the phasors, the scaled dispersion values and the scaled energy deviations cannot be normalized after the fit. Lastly, the phase jumps at the origin are compressed into

$$E_{mjk} = e^{i\pi q_m \text{sign}(s_k - s_j)} \tag{8.4}$$

for easier readability and referred to as model information terms in the following. Here, q_m are the fractional betatron tunes. The model information terms and the steerer parameters are defined as complex conjugates of the quantities used in the original work [13].

8.2 Start-Value Layer

COBEA's start-value layer, dubbed the monitor-corrector subset (MCS) algorithm, works in two steps. Firstly, the beta functions and the betatron phase advances at four (or more) BPMs are reconstructed via an eigenvalue problem in composite-monitor space. This intermediate result is, secondly, used in the corrector-monitor (CM) mapping to determine steerer parameters for all steerer magnets and phasors at all BPMs.

8.2.1 Eigenvalue Problem in Composite-Monitor Space

The first part of the MCS algorithm extracts phasors at four (or more) BPMs and both betatron tunes from an ORM using nothing but sparse model information as additional input.

It is based on the possibility to determine the beta function and the phase advance at a single BPM j_1 by solving the eigenvalue problem

$$
\boldsymbol{T}_{j_1 \to j_1}
\begin{pmatrix}
Z_{m1j_1} \\
Z'_{m1j_1} \\
Z_{m2j_1} \\
Z'_{m2j_1}
\end{pmatrix}
= e^{i\mu_m}
\begin{pmatrix}
Z_{m1j_1} \\
Z'_{m1j_1} \\
Z_{m2j_1} \\
Z'_{m2j_1}
\end{pmatrix},
\tag{8.5}
$$

where the one-turn transfer map $\boldsymbol{T}_{j_1 \to j_1}$ maps a phase space vector at BPM j_1 to the next turn. To reduce reliance on a lattice model, no one-turn map is known a priori. The algorithm solves this problem by reconstructing a proxy one-turn transfer map $\tilde{\boldsymbol{T}}$ from the ORM. The proxy map discards the momentum components at BPM j_1 for the spatial components of a second BPM j_2 thereby mapping vectors of the spatial components of two BPMs j_1 and j_2 to the next turn. The purely spatial 4D vector space is dubbed composite-monitor space because it is composed of the 2D spatial vector spaces at two BPMs. The proxy map constitutes the eigenvalue problem

$$
\tilde{\boldsymbol{T}}
\begin{pmatrix}
Z_{m1j_1} \\
Z_{m2j_1} \\
Z_{m1j_2} \\
Z_{m2j_2}
\end{pmatrix}
= e^{i\mu_m}
\begin{pmatrix}
Z_{m1j_1} \\
Z_{m2j_1} \\
Z_{m1j_2} \\
Z_{m2j_2}
\end{pmatrix}
\tag{8.6}
$$

and thus contains the beta function and the betatron phase advance of both modes for both BPMs in its eigenvectors and also both mode tunes in its eigenvalues. The reconstruction of the proxy map requires dividing the lattice into two parts A and B. These are described by two separate proxy maps $\boldsymbol{M}^{\mathrm{A}}$ and $\boldsymbol{M}^{\mathrm{B}}$ so that

$$
\tilde{\boldsymbol{T}} = \boldsymbol{M}^{\mathrm{A}} \boldsymbol{M}^{\mathrm{B}}.
\tag{8.7}
$$

The matrix $\boldsymbol{M}^{\mathrm{A}}$ maps the spatial components from BPMs j_1 and j_2 to two additional BPMs j_3 and j_4. The matrix $\boldsymbol{M}^{\mathrm{B}}$ maps the spatial components from j_3 and j_4 to j_1 and j_2. These two maps can be directly reconstructed from the ORM by solving the system of equations

$$
\boldsymbol{M}^{\mathrm{A}} \boldsymbol{R}^{\mathrm{A}}(j_1, j_2) = \boldsymbol{R}^{\mathrm{A}}(j_3, j_4)
\tag{8.8}
$$

and

$$
\boldsymbol{M}^{\mathrm{B}} \boldsymbol{R}^{\mathrm{B}}(j_3, j_4) = \boldsymbol{R}^{\mathrm{B}}(j_1, j_2).
\tag{8.9}
$$

The matrices $\boldsymbol{R}^{\mathrm{A}}(j_1, j_2)$ and $\boldsymbol{R}^{\mathrm{A}}(j_3, j_4)$ as well as $\boldsymbol{R}^{\mathrm{B}}(j_1, j_2)$ and $\boldsymbol{R}^{\mathrm{B}}(j_3, j_4)$ are parts of the ORM. They contain the matrix elements at the listed BPMs for subsets of steerer magnets. The subsets must be located in the active segment of their respective measurement cycle. Figure 8.1 gives a visual explanation. For cycle A, the matrices only contain steerer magnets

between BPMs j_4 and j_1 and for cycle B, the matrices contain steerer magnets between BPMs j_2 and j_3. Since each of the proxy transfer maps $\boldsymbol{M}^{\mathrm{A}}$ and $\boldsymbol{M}^{\mathrm{B}}$ is a 4×4 matrix, there need to be at least 4 steerer magnets in each active segment in order to solve Eq. (8.8) and Eq. (8.9). Finally, the phasors resulting from the eigenvalue problem of BPMs j_1 and j_2 Eq. (8.6) can be propagated to phasors at BPMs j_3 and j_4 using map $\boldsymbol{M}^{\mathrm{B}}$. Since the first part of the MCS algorithm also works with more than two segments, phasors at all BPMs can be reconstructed this way.
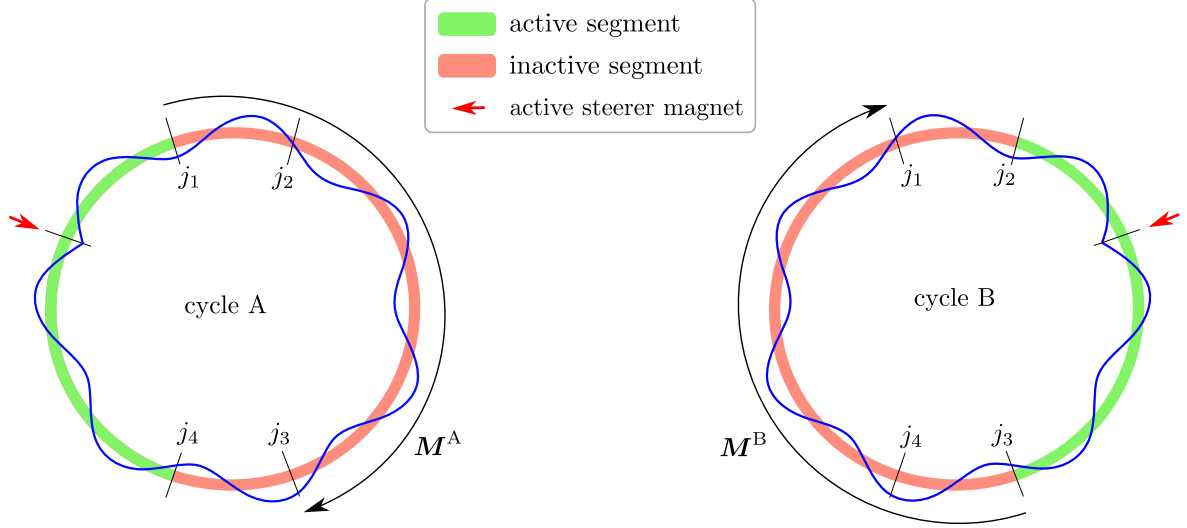
Figure 8.1: Schematic of the reconstruction process for the proxy transfer map of cycle A $\boldsymbol{M}^{\mathrm{A}}$ in composite-monitor space via Eq. (8.8) (left) and the proxy transfer map of cycle B $\boldsymbol{M}^{\mathrm{B}}$ via Eq. (8.9) (right). Each cycle is drawn with an example orbit response of an active steerer magnet. At least four such orbit response measurements with different steerer magnets are required to solve the system of equations for each cycle. The active steerer magnets must be located in the active segments, between BPMs j_4 and j_1 for cycle A and between BPMs j_2 and j_3 for cycle B.

8.2.2 Corrector-Monitor Mapping

The second part of the MCS algorithm, CM mapping, maps the BPM phasors resulting from the eigenvalue problem in composite-monitor space to the steerer parameters for all steerer magnets and the phasors for all BPMs. The discretized BE model Eq. (8.2) can be written as a vector product

$$R_{wjk} = R_{wjk}^{\mathrm{BE}} = \Re\left\{ (Z_{1wj}E_{1jk},\ Z_{Mwj}E_{Mjk})\begin{pmatrix} A_{1k} \\ A_{Mk} \end{pmatrix} \right\} \tag{8.10}$$

that allows to rewrite the ORM as a linear system of equations (see Appendix 13.1.1 for details)

$$\vec{A}^{\mathrm{I}} = \Re\left\{ \boldsymbol{B}^{\mathrm{I}}\vec{C}^{\mathrm{I}} \right\}. \tag{8.11}$$

Here, $\vec{A}^{\mathrm{I}}$ is the ORM in vector form, the matrix $\boldsymbol{B}^{\mathrm{I}}$ is made up of the phasors at all BPMs and all model-information terms while the vector $\vec{C}^{\mathrm{I}}$ consists of all steerer parameters. This system of equations can theoretically be solved for $\vec{C}^{\mathrm{I}}$ giving all steerer parameters. In practice, COBEA's implementation of the eigenvalue problem in composite-monitor space (see Ch. 8.2.1 for details), the first part of the start-value layer, only returns the phasors at a subset of BPMs j_1, j_2, j_3 and j_4. To account for this, the system of equations Eq. (8.11) is reformulated with a vector $\vec{A}^{\mathrm{I}}(j_1,\ j_2,\ j_3,\ j_4)$ that only holds the ORM elements corresponding to the subset of BPMs and a matrix $\boldsymbol{B}^{\mathrm{I}}(j_1,\ j_2,\ j_3,\ j_4)$ that only consists of the subset's phasors and model-information terms as

$$\vec{A}^{\mathrm{I}}(j_1,\ j_2,\ j_3,\ j_4) = \Re\Big\{\boldsymbol{B}^{\mathrm{I}}(j_1,\ j_2,\ j_3,\ j_4)\vec{C}^{\mathrm{I}}\Big\}. \tag{8.12}$$

With the available information, this system of equations can be solved for the matrix $\vec{C}^{\mathrm{I}}$ giving all steerer parameters. Taking a different perspective, the BE model can also be written as a vector product

$$R_{wjk} = R^{\mathrm{BE}}_{wjk} = \Re\left\{(E_{1jk}A_{1k},\ E_{Mjk}A_{Mk})\begin{pmatrix} Z_{1wj} \\ Z_{Mwj} \end{pmatrix}\right\}. \tag{8.13}$$

This allows to rewrite the ORM as another linear system of equations (see Appendix 13.1.2 for details)

$$\vec{A}^{\mathrm{II}} = \Re\Big\{\boldsymbol{B}^{\mathrm{II}}\vec{C}^{\mathrm{II}}\Big\}, \tag{8.14}$$

where $\vec{A}^{\mathrm{II}}$ is the ORM in (another) vector form, the matrix $\boldsymbol{B}^{\mathrm{II}}$ contains all steerer parameters as well as all model-information terms and the vector $\vec{C}^{\mathrm{II}}$ contains all BPM phasors. As all steerer parameters are known at this point, the system can be solved for the matrix $\vec{C}^{\mathrm{II}}$ giving phasors at all BPMs and thereby completing the generation of start values. CM mapping also works if the first part of the start-value layer only returns phasors for two BPMs. All in all, a storage ring with two BPMs and two steerer magnets is the minimum requirement for using CM mapping. The requirements of the first part of the start-value layer are bigger (see closing paragraph of Ch. 8.2.1) and therefore determine the requirements of the start-value layer as a whole.

8.3 Fit Layer

The second layer fits the BE+d model Eq. (8.3) onto the input ORM

$$\min_{\vec{v}} \sum_{wjk} \Big(R^{\mathrm{BE+d}}_{wjk}(\vec{v}) - R_{wjk}\Big)^2. \tag{8.15}$$

employing a quasi-Newton-type method, the limited-memory Broyden–Fletcher–Goldfarb–Shanno algorithm with box constraints (L-BFGS-B) [90] from the `SciPy Python` package [91]. The

optimization variables $\vec{v}$ comprise the BPM phasors Z_{mwj}, the steerer parameters A_{mk}, the tunes μ_m, the scaled dispersion values d_{wj} and the scaled energy deviations b_k. The complex BPM phasors and the complex steerer parameters constitute two degrees of freedom per unit. This gives $2MWJ$ and $2MK$ degrees of freedom for the BPM phasors and the steerer parameters, respectively. The tunes, the scaled dispersion values and the scaled energy deviations are real numbers adding M, WJ and K degrees of freedom. Overall, the optimization variables constitute

$$n = 2MWJ + 2MK + M + WJ + K - (2M + 1) \tag{8.16}$$

degrees of freedom. The $2M + 1$ degrees of freedom subtracted in the end correspond to M start phases, M invariants (phasors) and 1 additional invariant (dispersion term). The BE+d model for the storage ring at DELTA with its $J = 54$ BPMs and $K = 56$ steerer magnets has 1041 degrees of freedom.

8.4 POSTPROCESSING LAYER

The postprocessing layer calculates the beta function estimates, the betatron phase estimates, and the integer tune estimates. Additionally, it provides uncertainties for these quantities based on linear error propagation. Since the uncertainties are not needed for this work, they are not discussed here. See [13] for further details.

8.4.1 BETA FUNCTION ESTIMATES

The beta function estimates are calculated from the fitted BPM phasors according to

$$\beta_{mwj} = \frac{Z_{mwj} Z_{mwj}^*}{C_m}, \tag{8.17}$$

where C_m is a mode-specific invariant of betatron motion that was explained in Ch. 3.1. Its calculation [13]

$$C_m = \Im\{Z_{mwj}^* Z_{mwj}'\} \tag{8.18}$$

requires knowledge of the phase space and hence the derivative of the BPM phasor Z_{mwj}' at a single BPM. Calculating the latter can be achieved if Z_{mwj} is associated with one of two BPMs enclosing a drift space. The difference quotient

$$Z_{mwj}' = Z_{mw(j+1)}' = \frac{Z_{mw(j+1)} - Z_{mwj}}{l} \tag{8.19}$$

then equals the derivative of the phasors at both BPMs with respect to s. The phasor of the second enclosing BPM is $Z_{mw(j+1)}$. At DELTA, a drift space is enclosed by BPM38 and BPM39 shortly before the SCW (see Fig. 2.7 for the position of all BPMs). The length of

the drift space is $l = 0.866$ m. It was used in the calculation of all beta function estimates via COBEA and the RSFA presented in this work.

8.4.2 BETATRON PHASE ADVANCE ESTIMATES

The coupled betatron phase advance estimates for the first BPM are set to zero $\Phi_{mw1} = 0$ to remove, in accordance with the definition of the decoupled phase advance in Eq. (2.5), the fluctuating start phase. The estimates of the remaining BPMs are calculated from the fitted phasors at neighboring BPMs as

$$\Phi_{mwj} = \arctan 2(\Re\{z\}, \Im\{z\}) \qquad \text{with} \qquad z = Z^*_{mw(j-1)} Z_{mwj}. \tag{8.20}$$

The $\arctan 2(x, y)$ function calculates the angle between the vector pointing towards (x, y) and $\vec{e}_x$ (see schematic in Fig. 8.2). In contrast to arctan, $\arctan 2$ also produces the correct angle if the signs of x and y differ. Used in this context, Eq. (8.20) determines the angle between $Z_{mw(j-1)}$ and Z_{mwj}. The definition of the coupled betatron phase advances calculated by COBEA differs from the definition of the phase advances in the propagated eigenvectors Eq. (3.7) given in [65]. For a primarily horizontal first mode and a primarily vertical second mode, both definitions are related by $\Phi_{11j} = \Phi_1(s_j)$, $\Phi_{22j} = \Phi_2(s_j)$, $\Phi_{21j} = \Phi_2(s_j) + \nu_2(s_j)$ and $\Phi_{12j} = \Phi_1(s_j) + \nu_1(s_j)$.
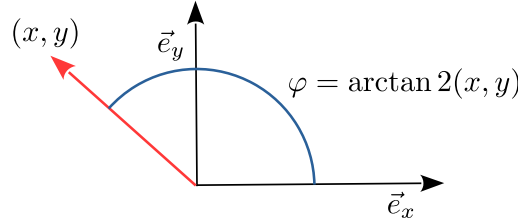
Figure 8.2: The angle calculated by $\arctan 2$ is correct even if the signs of x and y are not the same.

8.4.3 SCALED DISPERSION ESTIMATES

The fitted values d_{wj} are related to the real dispersion D_{wj} by an unknown factor that cannot be recovered. Therefore the fit variables d_{wj} are referred to as scaled dispersion.

8.4.4 INTEGER BETATRON TUNE ESTIMATES

The two betatron tunes determine the betatron oscillations per turn in their respective betatron mode. Each splits into an integer part Q_m and a fractional part q_m. The fractional part is a fit variable of the BE+d model and a direct result of the fitting process. An estimate of the integer part is only calculated in the approximation of decoupled beam optics. For that purpose, COBEA divides the sum of the betatron phase estimates at all BPMs (see Ch. 8.4.2 for details) by 2π. The result is rounded down. It has to be corrected if the invariant of the fit is negative $C_m = -|C_m|$. In that case, the integer part is reduced by 1. An integer tune

calculated via this procedure only reflects reality if there is less then 2π rad phase advance between neighboring BPMs.

9 THE RESPONSE SET FIT ALGORITHM

The RSFA adapts the basic idea of COBEA described in Ch. 8, extracting optical information from an ORM measurement, to response sets. Both algorithms are compared in two simulation studies in Ch. 10 for use in a storage ring in the presence of transverse coupling. Chapter 11 presents experimental results for the RSFA.

9.1 RESPONSE SETS

Response sets comprise response set entries $\mathcal{R}_i$ indexed by $i = 1, \cdots, I$ that can be parameterized as a product of an unknown coupled ORM $\boldsymbol{R}$ in the format of Eq. (8.1) and a vector of steerer strengths $\vec{\theta}_i$ according to Eq. (2.18) as

$$\vec{\mathcal{R}}_i = \boldsymbol{R}\vec{\theta}_i. \tag{9.1}$$

Figure 9.1 compares the orbit response underlying a response set entry to the orbit response of an ORM column. Response sets can, in contrast to ORMs Eq. (4.1), not be normalized with a single steerer strength because each of their entries contains contributions from multiple magnets. A response set

$$\boldsymbol{\mathcal{R}} = \left(\vec{\mathcal{R}}_1 \ \cdots \ \vec{\mathcal{R}}_I \right) \tag{9.2}$$

therefore comes paired with a steerer strength set of equal size

$$\boldsymbol{\theta} = \left(\vec{\theta}_1 \ \cdots \ \vec{\theta}_I \right). \tag{9.3}$$

The new orbit correction software automatically measures a response set entry whenever it corrects the orbit.

9.2 START VALUE GENERATION

The generation of start values in the generalized fit problem adheres to COBEA's two step approach (see Ch. 8.2 for details). Firstly, phasors at four (or more) BPMs are calculated by solving an eigenvalue problem in composite-monitor space. Secondly, the resulting phasors are used to determine all steerer parameters and BPM phasors at all BPMs via a modified CM mapping approach.
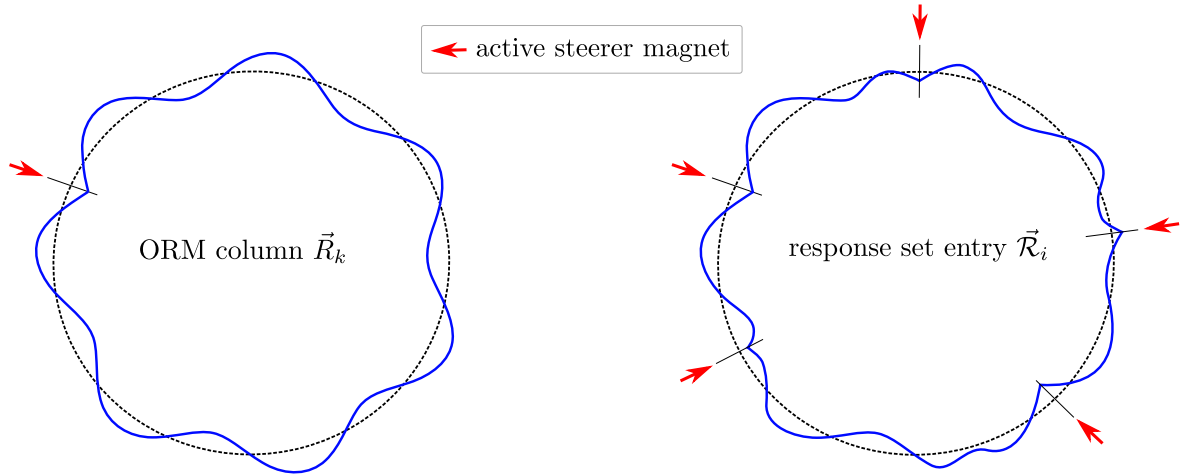
Figure 9.1: Schematic comparison of the orbit response (blue) underlying an ORM column $\vec{R}_k$ (left) and one underlying a response set entry $\vec{\mathcal{R}}_i$ (right): the column is formed by one active steerer magnet while the entry is formed by several.

9.2.1 Eigenvalue Problem for Response Sets

The first part of the original MCS algorithm (see Ch. 8.2.1) divides the lattice into parts A and B. Part A is defined by two entry BPMs j_1 and j_2 and two exit BPMs j_3 and j_4. Part B is defined by two entry BPMs j_3 and j_4 and two exit BPMs j_1 and j_2. The general approach is maintained here as is the original goal: reconstruct the proxy transfer maps in composite monitor space $\boldsymbol{M}^A$ and $\boldsymbol{M}^B$ from Eq. (8.7) and then solve Eq. (8.6). Obtaining the necessary orbit response information for calculating $\boldsymbol{M}^A$ requires adhering to measurement cycle A (see left side of Fig. 8.1). Therefore, an inactive segment in between the BPMs j_1 and j_4 is needed. As each set entry Eq. (9.1) is a superposition of the orbit responses of all K steerer magnets and the steerer magnets are distributed around the storage ring (see right side of schematic in Fig. 9.1), few neighboring BPMs go without a steerer in between them. It is therefore impossible to find an inactive segment that spans half the storage ring. A linear fit of the ORM solves this problem but also imposes a $I \geq K$ restriction on the response set size and is as such ruled out. Instead, a new approach is required. It is the creation of an inactive segment by finding a superposition of response set entries that cancel out locally between the BPMs j_1 and j_4. This is equivalent to demanding that the $\tilde{K}$ steerer magnets in that segment should be associated with zero steerer strength (inactive) in every response set entry. Solving a system of equations

$$0 = \begin{pmatrix} \theta_{11} & \cdots & \theta_{1I} \\ \vdots & \ddots & \vdots \\ \theta_{\tilde{K}1} & \cdots & \theta_{\tilde{K}I} \end{pmatrix} \vec{a}_n \tag{9.4}$$

gives I coefficients

$$\vec{a}_n = (a_{1n} \cdots a_{In})^{\mathrm{T}} \tag{9.5}$$

determining a proxy response set entry

$$\vec{\mathcal{R}}_n^{\mathrm{A}} = \boldsymbol{\mathcal{R}} \vec{a}_n \tag{9.6}$$

that matches this description. The entry does not contain orbit response components belonging to any of the $\tilde{K}$ steerer magnets in the now inactive segment. Figure 9.2 visualizes the orbit responses underlying the original entry and the proxy entry. The process of determining a coefficient vector is repeated until the resulting linear combinations of orbit response entries fill a proxy response set

$$\boldsymbol{\mathcal{R}}^{\mathrm{A}} = \left(\vec{\mathcal{R}}_1^{\mathrm{A}} \cdots \vec{\mathcal{R}}_I^{\mathrm{A}} \right) \tag{9.7}$$

of the same length as the initial set $N = I$. The index $n = 1, \cdots, N$ counts the repetitions. Note, that all solutions to Eq. (9.4) in the proxy response set need to be linearly independent. A simple way achieving this, which was implemented for this work, is to replace the nth coefficient in $\vec{a}_n$ by -1 (or another constant). The first coefficient vector ($n = 1$) then is

$$\vec{a}_1 = (-1, \, a_{2n} \cdots a_{In})^{\mathrm{T}}, \tag{9.8}$$

the second coefficient vector ($n = 2$) is

$$\vec{a}_2 = (a_{1n}, \, -1, \, a_{3n} \cdots a_{In})^{\mathrm{T}} \tag{9.9}$$

and so forth. A proxy response set calculated in this manner allows to construct the same proxy transfer map $\boldsymbol{M}^{\mathrm{A}}$ in composite-monitor space as in the original MCS algorithm by solving a slightly different system of equations

$$\boldsymbol{M}^{\mathrm{A}} \boldsymbol{\mathcal{R}}^{\mathrm{A}}(j_1, \, j_2) = \boldsymbol{\mathcal{R}}^{\mathrm{A}}(j_3, \, j_4). \tag{9.10}$$

Here, the matrices $\boldsymbol{\mathcal{R}}^{\mathrm{A}}(j_1, \, j_2)$ and $\boldsymbol{\mathcal{R}}^{\mathrm{A}}(j_3, \, j_4)$ are parts of the proxy response set created for cycle A that hold elements for the listed BPMs formed by the steerer magnets in the active segment. The proxy transfer map in composite-monitor space of segment B $\boldsymbol{M}^{\mathrm{B}}$ is calculated in a similar fashion. Constructing the proxy response set of segment B $\boldsymbol{\mathcal{R}}^{\mathrm{B}}$ requires finding linear combinations of the original response set entries so that the steerer strengths cancel out locally between BPMs j_3 and j_2. The proxy response set for segment B then determines the proxy transfer map in composite-monitor space according to

$$\boldsymbol{M}^{\mathrm{B}} \boldsymbol{\mathcal{R}}^{\mathrm{B}}(j_3, j_4) = \boldsymbol{\mathcal{R}}^{\mathrm{B}}(j_1, j_2). \tag{9.11}$$

Here, the matrices $\boldsymbol{\mathcal{R}}^{\mathrm{B}}(j_3, j_4)$ and $\boldsymbol{\mathcal{R}}^{\mathrm{B}}(j_1, j_2)$ are parts of the proxy response set created for cycle B that hold elements for the listed BPMs formed by the steerer magnets in the active segment. Finally, the proxy transfer maps of both segments are used to compose the proxy one-turn map Eq. (8.7) that is in turn employed to construct and solve the eigenvalue problem in composite-monitor space (8.6) yielding the spatial phasors of both betatron modes at BPMs j_1 and j_2 that can be propagated to BPMs j_3 and j_4.
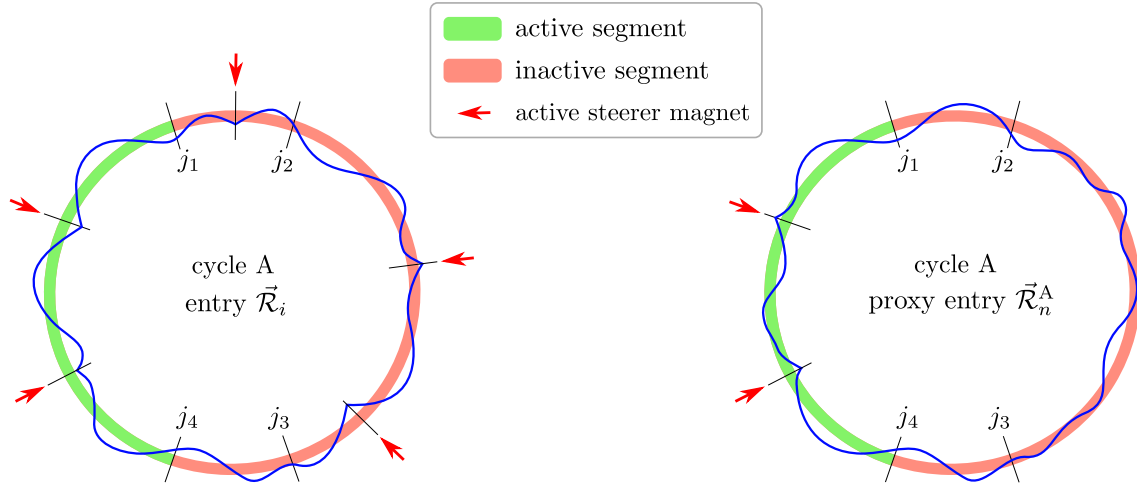
Figure 9.2: Schematic comparison of the continuous orbit response (blue) underlying a response set entry $\vec{\mathcal{R}}_i$ (left) and one underlying a proxy response set entry $\vec{\mathcal{R}}_n^{\mathrm{A}}$ (right) in measurement cycle A. The original response set entry cannot be used for the construction of the proxy transfer $\boldsymbol{M}^{\mathrm{A}}$ because the underlying orbit response is formed by active steerer magnets in the inactive segment. The proxy response set entry can be used because its underlying orbit response is only formed by active steerer magnets in the active segment.

The described method preserves the minimum hardware requirement of COBEA's MCS algorithm. The reconstruction of each proxy transfer map in composite-monitor space requires 4 steerer magnets in the perturbed segment and 4 BPMs. Going with the method described above, that makes 4 BPMs and 8 steerer magnets in total. The data requirement is, however, smaller. Where COBEA's start value layer requires 8 ORM columns, one for each of the steerer magnets, the start value layer of the RSFA only requires a response set with $I = 4$ entries. This set can then be reshuffled into two different proxy response sets of the same length for segments A and B.

9.2.2 CM Mapping on Response Sets

The matrix decomposition used in the orignal CM mapping factorizes the ORM into known and unknown matrices based on the BE model to construct a system of equations that can be solved for the unknown part. A similar approach also works for response sets. Neglecting dispersion,

the response set elements from Eq. (9.2) can be parameterized as linear combinations of BE model instances Eq. (8.2)

$$\mathcal{R}_{wji} = \sum_{k=1}^{K} \theta_{ki} R_{wjk}^{\text{BE}} = \sum_{k=1}^{K} \theta_{ki} \sum_{m=1}^{M} \Re\{Z_{mwj} E_{mjk} A_{mk}\}, \tag{9.12}$$

where θ_{ki} are elements from the steerer strength set Eq. (9.3). Factorizing the equation as

$$\mathcal{R}_{wji} = \Re\{(\theta_{1i} Z_{1wj} E_{1j1} \cdots \theta_{Ki} Z_{1wj} E_{1jK}, \theta_{1i} Z_{Mwj} E_{Mj1}, \cdots, \theta_{Ki} Z_{Mwj} E_{MjK}) \tag{9.13}$$

$$\cdot (A_{11} \cdots A_{1K}, A_{M1} \cdots A_{MK})^{\text{T}}\} \tag{9.14}$$

allows to rewrite the response set as a linear system of equations (see Appendix 13.2.1 for details)

$$\vec{\mathcal{A}}^{\text{I}} = \Re\left\{\boldsymbol{\mathcal{B}}^{\text{I}} \vec{\mathcal{C}}^{\text{I}}\right\}. \tag{9.15}$$

Here, the vector $\vec{\mathcal{A}}^{\text{I}}$ is the response set in vector form. The matrix $\boldsymbol{\mathcal{B}}^{\text{I}}$ contains phasors at all BPMs, all model-information terms and the complete steerer strength set. The vector $\vec{\mathcal{C}}^{\text{I}}$ is made up of all steerer parameters. If the matrix $\boldsymbol{\mathcal{B}}^{\text{I}}$ is known, the system of equations can be solved for the steerer parameters. This is not possible as only the phasors of the four BPMs j_1, j_2, j_3 and j_4 are known at this point. Instead, a reduced version of the system of equations

$$\vec{\mathcal{A}}^{\text{I}}(j_1, j_2, j_3, j_4) = \Re\left\{\boldsymbol{\mathcal{B}}^{\text{I}}(j_1, j_2, j_3, j_4) \vec{\mathcal{C}}^{\text{I}}\right\} \tag{9.16}$$

has to be used. Here, $\vec{\mathcal{A}}^{\text{I}}(j_1, j_2, j_3, j_4)$ and $\boldsymbol{\mathcal{B}}^{\text{I}}(j_1, j_2, j_3, j_4)$ only hold information for the listed BPMs. The reduced system of equations can be solved for $\vec{\mathcal{C}}^{\text{I}}$ giving steerer parameters for all steerer magnets. Alternatively, the response set elements $\mathcal{R}_{wji}$ can be written as a vector product

$$\mathcal{R}_{wji} = \sum_{k=1}^{K} \theta_{ki} R_{wjk}^{\text{BE}} = \Re\left\{\left(\sum_{k=1}^{K} \theta_{ki} E_{1jk} A_{1k}, \sum_{k=1}^{K} \theta_{ki} E_{Mjk} A_{Mk}\right) \begin{pmatrix} Z_{1wj} \\ Z_{Mwj} \end{pmatrix}\right\}. \tag{9.17}$$

This allows to rewrite the response set as another linear system of equations (see Appendix 13.2.2 for details)

$$\vec{\mathcal{A}}^{\text{II}} = \Re\left\{\boldsymbol{\mathcal{B}}^{\text{II}} \vec{\mathcal{C}}^{\text{II}}\right\}, \tag{9.18}$$

where the vector $\vec{\mathcal{A}}^{\text{II}}$ is the response set in vector form and the vector $\vec{\mathcal{C}}^{\text{II}}$ contains all BPM phasors. The matrix $\boldsymbol{\mathcal{B}}^{\text{II}}$ contains all steerer parameters, all model-information terms and the complete steerer strength set. The system of equations is solved for matrix $\vec{\mathcal{C}}^{\text{II}}$ giving the final results, the phasors at all BPMs.

A difference in applying CM mapping on response sets to the original CM mapping on response matrices is the minimum requirement of the second step. With response matrices, a subset

of steerer parameters can be mapped to a subset of BPMs. In the case of response sets, all steerer parameters have to be known. This is not a problem since a subset of BPM phasors can still be mapped to all steerer parameters. The first step of the CM mapping procedure hence produces enough steerer parameters to conduct the second step.

9.3 Fit

Fitting the BE+d model on a response set can be achieved by solving the minimization problem

$$\min_{\vec{v}} \sum_{wji} \left(\mathcal{R}_{wji} - \sum_{k} R_{wjk}^{\text{BE+d}}(\vec{v})\theta_{ki} \right)^2 . \tag{9.19}$$

The aggregated vector of fit variables $\vec{v}$ is determined by the parameters of the BE+d model and the parameterization of the complex numbers in the model. The latter may either be polar or Cartesian. COBEA uses the Cartesian representation of complex numbers as does the RSFA. The vector of fit variables and the number of degrees of freedom are thus mostly the same. The only exception are the betatron tunes. The RSFA offers the option to keep them constant. This allows to feed the algorithm with tune measurements from another source such as the kicker-based tune measurement system (see Ch. 2.2.4). This reduces the difficulty of the fit problem and sometimes improves fit results. If the tunes are kept constant, the number of degrees of freedom is reduced by two. Tunes included, the BE+d model for the storage ring at DELTA has 1041 degrees of freedom (see Ch. 8.3). Each response set entry adds $J = 54$ data points in $W = 2$ planes, that is $WJ = 108$ data points in total, to the optimization problem. Hence, the theoretical minimum response set size for the RSFA is 10 so that

$$10 \cdot 108 = 1080 > 1041 \tag{9.20}$$

holds. For all application discussed in this document, the Adam (adaptive moment estimation) algorithm [92] from the tensorflow `Python` package [93] was used to conduct the fitting process. The algorithm was developed for large-scale machine learning problems and works well with non-linear objective functions.

9.4 Postprocessing

The estimates for the beta function, the betatron phase and the scaled dispersion are extracted from the fit results. This process is the same as in COBEA because the fit variables are the same. Similar to COBEA, a calculation of fit uncertainties has been implemented on the basis of linear error propagation. The propagation of errors differs for the RSFA because its objective function is different. The implementation is not discussed here because the resulting uncertainties are not used in this work.

10 Simulation Studies Benchmarking the Two Orbit Response Fit Algorithms

The description of the COBEA algorithm in Ch. 8 layed the foundation for introducing the RSFA in Ch. 9. In the following, both algorithms are benchmarked on simulated orbit response matrices (ORMs) and simulated response sets to assess the quality of their optical function estimates in the presence of coupling and without it. Chapter 11 presents RSFA fit results on experimental data.

10.1 Simulation Details

The ORMs and response sets used for fitting purposes in the simulation studies described in this chapter were simulated in `MADX` [83] and assembled in `Python` using the `PyMad Python-MADX` application interface [84]. The *del008.2001* optics model of the storage ring at DELTA [34] (see Ch. 2.4 for details) was the basis for all simulations. For this work, the model was modified in two ways:

1. Addition of a $30\,\mathrm{cm}$ long $499.83\,\mathrm{MHz}$ cavity with a voltage of $300\,\mathrm{kV}$. The RF resonator alters the beam energy when the orbit length changes. This was described in Ch. 2.1.2 and is necessary to test the dispersion term in the BE+d model.

2. Assumption of skew angles $a_q\hat{\varphi}$ for each quadrupole. Here, $\hat{\varphi}$ is a unified skew angle that is the same for all quadrupoles and a_q is a quadrupole-specific factor. A skew angle rolls a quadrupole about the longitudinal axis. This adds transverse coupling and is necessary to test the description of coupling in the BE+d model.

For the first simulation study presented in Ch. 10.2, seven ORMs were simulated column by column. Each column was determined by perturbing the storage ring model with a steerer strength of $0.25\,\mathrm{mrad}$ at a single steerer magnet, measuring the orbit difference and normalizing it with the steerer strength. The seven ORMs were simulated for the same quadrupole-specific factors and seven different unified skew angles, one every $5\,\mathrm{mrad}$ between 0 and $30\,\mathrm{mrad}$. The factors were chosen in a way that, for a unified angle of $\hat{\varphi} = 10\,\mathrm{mrad}$, `MADX` produces coupled beta function results similar to the COBEA estimates for the ORM measurement *response.160311-2*. Figure 10.1 presents a comparison of the `MADX` simulation and the COBEA results. Each further increment of the unified skew angle rotates the primarily horizontal mode and the primarily vertical mode of betatron motion further out of their native planes (see schematic in Fig. 3.2 for an explanation of this process) and introduces more transverse
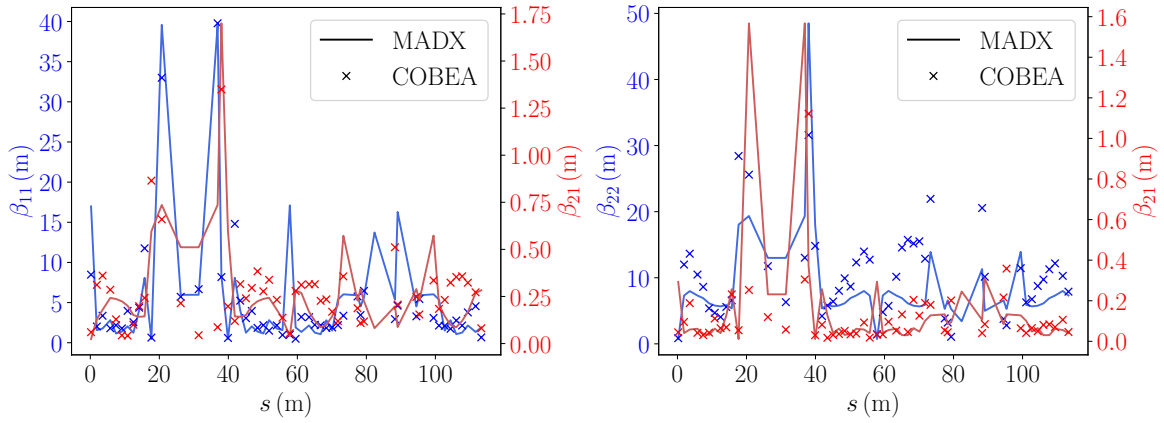
Figure 10.1: Comparison of the coupled beta function results of the modified *del008.2001* model with a unified skew angle of $\hat{\varphi} = 10\,\text{mrad}$ calculated in `MADX` to results calculated via COBEA for the ORM *response.160311-2*. The COBEA results for BPM12 (faulty pickup) and BPM41 (large fit residuals) were removed.

coupling. This results in a rising ratio of the primary-plane and secondary-plane beta function values of each betatron mode as Fig. 10.2 suggests. Neglecting the marginal effect of the cavity on the optical function calculation, the beta function results for a unified skew angle $\hat{\varphi} = 0$ are the same as the results for the unmodified *del008.2001* model presented in Fig. 2.6. The ORM simulations for larger unified skew angles $\hat{\varphi} > 10\,\text{mrad}$ were examined to test the capabilities of COBEA and the RSFA to reconstruct optical functions in the presence of strong transverse coupling. A noise estimate for the BPM readings was not included in the ORM simulations because ORMs commonly have a large signal-to-noise ratio.
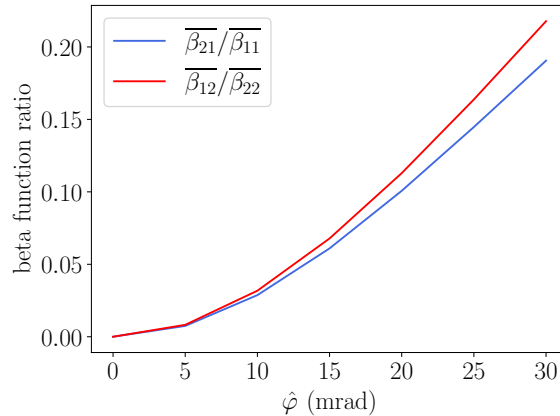
Figure 10.2: The evolution of transverse coupling in the modified *del008.2001* model depicted by ratios of the coupled BPM-averaged beta function values $\overline{\beta_{21}}/\overline{\beta_{11}}$ and $\overline{\beta_{12}}/\overline{\beta_{22}}$ for an increasing unified skew angle $\hat{\varphi}$ calculated in `MADX`.

The response sets in the second simulation study presented in Ch. 10.3 were only simulated for the realistic unified skew angle $\hat{\varphi} = 10\,\text{mrad}$. In contrast to the ORM simulations, the response set entries Eq. (9.1) were simulated with random equally distributed steerer strengths between

−0.1 mrad and 0.1 mrad. The smaller strength better reflects a common orbit correction step. Since the randomness may result in very small orbit shifts, BPM noise was added to the simulation to better reflect reality. Most BPMs at DELTA are equipped with Bergoz MX BPMs (see Ch. 2.2.2 for details). Their resolution is 5 µm. Any BPM reading consequently carries the risk of a ± 2.5 µm error that can be modeled via two uniformly distributed random variables ϵ_{x_1}, $\epsilon_{x_2} \in [-2.5\,\text{µm}, 2.5\,\text{µm}]$. The horizontal orbit response with noise at any BPM is thus given by

$$(x_2 + \epsilon_{x_2}) - (x_1 + \epsilon_{x_1}) = x + \epsilon_x, \tag{10.1}$$

where x_1 and x_2 are the orbit measurements before and after excitation, x is the horizontal orbit response without noise and ϵ_x is the triangularly distributed sum noise resulting from superpositioning the two uniformly distributed random variables ϵ_{x_1} and ϵ_{x_2}. The same holds true in the vertical plane. The optical function calculations were cross-checked with the `polymorphic tracking code` (`PTC`) [94] because the `MADX` Twiss module may not work properly in the presence of dispersion [83] but no significant differences in the calculation of beta functions or any other parameter were found.

10.2 Benchmark on Orbit Response Matrices

COBEA and the RSFA were fed with 7 simulated ORMs with increasing levels of transverse coupling. ORMs are a special type of response sets and can therefore be used as input of the RSFA. The precision requirement for COBEA's L-BFGS fit of the BE+d model was increased to 10^{-18} for the fits because it significantly increased COBEA's performance. The RSFA was used without betatron tune fitting (see Ch. 9.3 for details on this option). For each unified skew angle, the betatron phase advance Φ_{mj}^{fit}, the beta function β_{mwj}^{fit} and the dispersion results $\vec{d}_w$ of COBEA and the RSFA are compared to the betatron phase Φ_{mj}, the beta function β_{mwj} and the dispersion values $\vec{D}_w$ from `MADX`. The beta function and the dispersion values stem from the `MADX` Twiss module while the betatron phase results were calculated from transfer maps. The betatron phase advance deviations of the fits are evaluated as averages

$$\overline{\Delta\Phi}_m = \text{avg}_j \left| \Phi_{mj}^{\text{fit}} - \Phi_{mj} \right| \tag{10.2}$$

and standard deviations

$$\sigma_{\Phi_{mw}} = \text{std}_j \left(\Phi_{mj}^{\text{fit}} - \Phi_{mj} \right) \tag{10.3}$$

over all BPMs. The figures of merit for the beta function deviations are averages

$$\overline{\Delta\beta}_{mw} = \text{avg}_j \left| \beta_{mwj}^{\text{fit}} - \beta_{mwj} \right| \tag{10.4}$$

and standard deviations

$$\sigma_{\beta_{mw}} = \text{std}_j\left(\beta_{mwj}^{\text{fit}} - \beta_{mwj}\right) \tag{10.5}$$

over all BPMs. The dispersion values are compared via similarity products

$$a_w = \frac{\vec{D}_w^{\text{T}}\vec{d}_w}{\left\|\vec{D}_w\right\|^2 \cdot \left\|\vec{d}_w\right\|^2} \tag{10.6}$$

that may range from 0 if the shape of the fitted dispersion does not match the `MADX` dispersion at all, to 1 if the shape of the fitted dispersion is the same as the `MADX` dispersion, or -1 if the shapes match but one is flipped up-side-down as in $\vec{d}_w \to -\vec{d}_w$. This is necessary because the dispersion output from fits of the BE+d model is not normalized (see Ch. 8.4.3 for an explanation).

Results

The figures of merit are presented in Fig. 10.3. Strikingly, COBEA and the RSFA produce very similar results. The betatron phase advance deviations produced by both fit methods are small in the horizontal plane $\overline{\Delta\Phi}_1 < 0.4\,\text{mrad}$ and medium in the vertical plane $\overline{\Delta\Phi}_2 < 3\,\text{mrad}$. To give some perspective, `MADX` calculates an average phase advance of 170 mrad (horizontal) and 60 mrad (vertical) between BPMs for the *del008.2001* model. The primary beta function deviations are small in the horizontal plane $\overline{\Delta\beta}_{11} < 0.1\,\text{m}$ as well as in the vertical plane $\overline{\Delta\beta}_{22} < 0.15\,\text{m}$. The beta function averages over all BPMs in the *del008.2001* model (no coupling) are $\overline{\beta}_x = 5.7\,\text{m}$ and $\overline{\beta}_y = 9.5\,\text{m}$. The secondary beta function deviations are about the same size as the primary ones. They are $\overline{\Delta\beta}_{12} < 0.1\,\text{m}$ and $\overline{\Delta\beta}_{21} < 0.1\,\text{m}$. In general, the betatron phase and beta function deviations increase with the level of transverse coupling. The similarity products for the dispersion results indicate a close to perfect reconstruction of the scaled dispersion function in both planes $a_x \approx 1$ and $a_y \approx 1$. Only the vertical similarity product for a unified skew angle of $\hat{\varphi} = 0$ is close to zero because, without transverse coupling, there is hardly any dispersion in the vertical plane that could be fitted.

All in all, both fit methods reproduce the beta function of the `MADX` Twiss module well for all generalized skew angles. COBEA and the RSFA can therefore be expected to produce good beta function estimates at DELTA and should also be able to perform well in environments with larger transverse coupling.
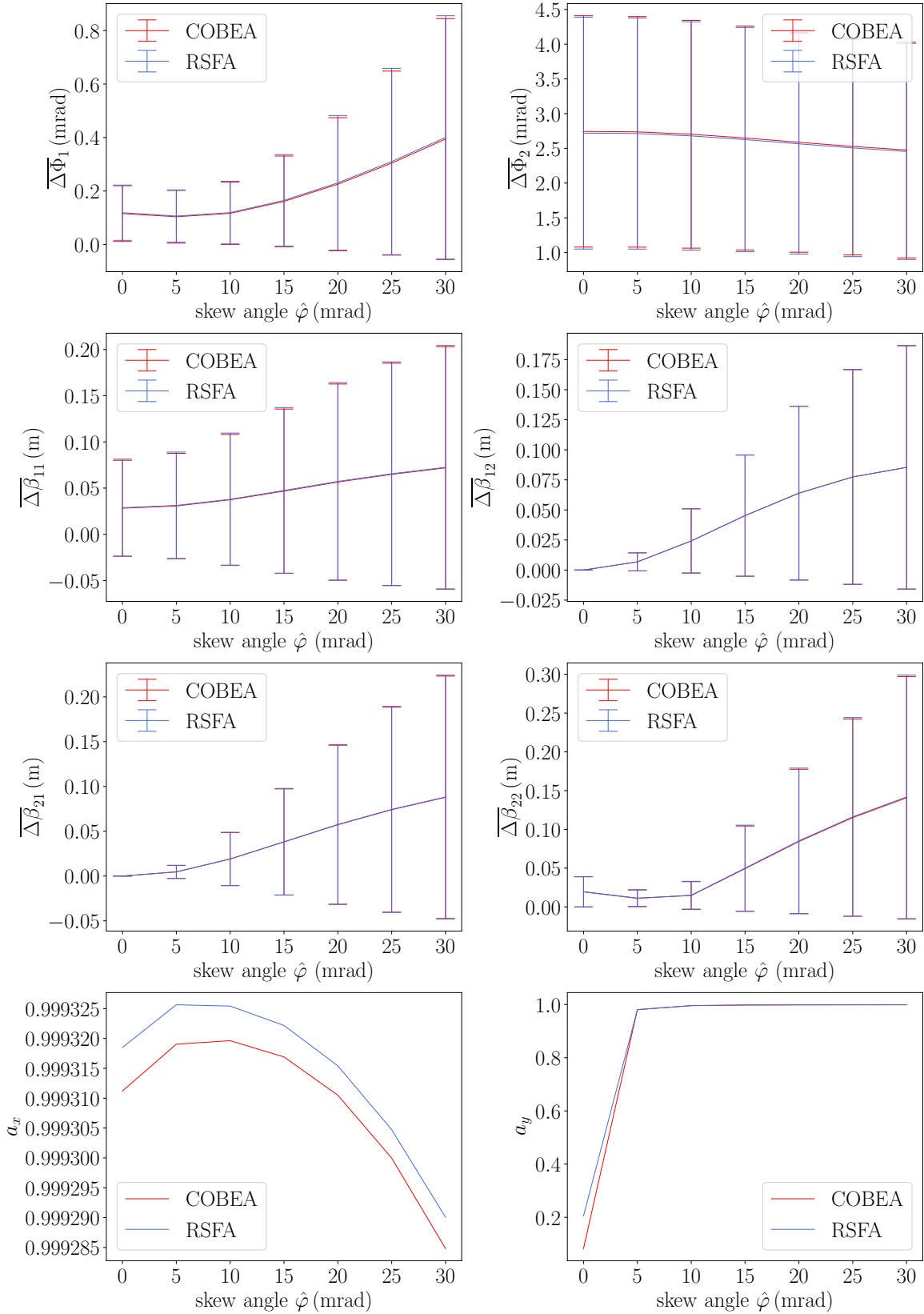
Figure 10.3: Comparison of COBEA and RSFA results for fits on simulated ORMs. Left and right side: horizontal and vertical quantities. From top to bottom: betatron phase Eq. (10.2) with error bars Eq. (10.3), beta function Eq. (10.4) with error bars Eq. (10.5) as well as dispersion similarity product Eq. (10.6).

10.3 ON RESPONSE SETS

COBEA and the RSFA were benchmarked on random response sets simulated for a unified skew angle of $\hat{\varphi} = 10$ mrad with set sizes ranging from $S = 20$ to 120. For COBEA, this required conducting a linear fit of the response sets first and then feeding its result into the algorithm because COBEA only accepts ORMs as input. The linear fit in this workaround restricts the minimum response set size to the number of steerer magnets that is 56. The theoretical minimum set size for the RSFA is 10. In contrast to the ORM fits, the RSFA was used with tune fitting here because, contrary to intuition, it increased the quality of the fit results. An explanation of the minimum response set size and the tune fitting option was given in Ch. 9.3.

The results of $U = 100$ fits with the COBEA workaround and the RSFA for each set size are compared in the following. The figures of merit used for this purpose are similar to the quantities introduced for the ORM benchmark in Ch. 10.3. But due to each response set size being tested with 100 random response sets, the fitted betatron phase advance Φ^{fit}_{umj}, the fitted beta function values $\beta^{\text{fit}}_{umwj}$ and the fitted dispersion values $\vec{d}_{uw}$ all carry an additional index u. All quantities are averaged over this index to compress the results into plots similar to Fig. 10.3. For response sets, the betatron phase advance deviations are evaluated as averages

$$\overline{\overline{\Delta\Phi}}_m = \text{avg}_j\left(\text{avg}_u\left|\Phi^{\text{fit}}_{umj} - \Phi_{mj}\right|\right) \tag{10.7}$$

and standard deviations

$$\sigma_{\overline{\Phi}_m} = \text{std}_j\left(\text{avg}_u\left|\Phi^{\text{fit}}_{umj} - \Phi_{mj}\right|\right) \tag{10.8}$$

over all BPMs. The figures of merit for the beta function deviations are averages

$$\overline{\overline{\Delta\beta}}_{mw} = \text{avg}_j\left(\text{avg}_u\left|\beta^{\text{fit}}_{umwj} - \beta_{mwj}\right|\right) \tag{10.9}$$

and standard deviations

$$\sigma_{\overline{\beta}_{mw}} = \text{std}_j\left(\text{avg}_u\left|\beta^{\text{fit}}_{umwj} - \beta_{mwj}\right|\right) \tag{10.10}$$

over all BPMs. The dispersion values are compared via similarity products

$$a_{uw} = \frac{\vec{D}_w^{\text{T}}\vec{d}_{uw}}{\left|\left|\vec{D}_w\right|\right|^2 \cdot \left|\left|\vec{d}_{uw}\right|\right|^2} \tag{10.11}$$

that may range from 0 if the shape of the fitted dispersion does not match the `MADX` dispersion at all, to 1 if the shape of the fitted dispersion is the same as the `MADX` dispersion, or -1 if the fitted dispersion values are flipped up-side-down $\vec{d}_w \to -\vec{d}_w$. This is necessary because

the dispersion output from fits of the BE+d model is not normalized (see Ch. 8.4.3). The distributions of the similarity products are evaluated as averages

$$\overline{a}_w = \text{avg}_u(a_{uw}) \tag{10.12}$$

and standard deviations

$$\sigma_{a_w} = \text{std}_u(a_{uw}). \tag{10.13}$$

10.3.1 Results

The figures of merit are presented in Fig. 10.4. The COBEA workaround and the RSFA produce very similar fit results for the largest response set size $S = 120$. Here, the average betatron phase advance deviations in both modes $\overline{\overline{\Phi}}_m(S = 120)$ are in the mrad range and beta function deviations $\overline{\overline{\Delta\beta}}_{mw}(S = 120) < 0.1\,\text{m}$ are also very small. Both are comparable to the fit results for the ORMs (see Fig. 10.3). For fits on smaller response set sizes, the deviations in betatron phase and beta functions increase. As expected, the COBEA workaround stops working below a set size of $S = 56$ where the linear fit of the response set becomes underconstrained. The RSFA was specifically designed to be used on small set sizes. For a set size of $S = 20$, it still produces small beta function deviations of $\overline{\overline{\Delta\beta}}_{mw}(S = 20) < 0.4\,\text{m}$. For even smaller set sizes, errors increase fast. Results for $S < 20$ are therefore excluded from the analysis. This includes the theoretical minimum set size of $S = 10$ (see Ch. 9.3 for an explanation). Despite the good general results, the response set fits of the COBEA workaround and the RSFA are worse than the previously analyzed ORM fits in two regards. One are the large standard deviations of the betatron phase advance $\sigma_{\overline{\Phi}_1}(S = 120) = 100\,\text{mrad}$ and $\sigma_{\overline{\Phi}_2}(S = 120) = 50\,\text{mrad}$. Even at the maximum set size, they are one to two orders of magnitude larger than the standard deviations of the betatron phase fits for the ORMs. Two are the dispersion fits whose similarity products mostly score considerably lower than 1 although their accuracy increases for larger set sizes. The noise added to the simulated response sets may take a toll here.

All in all, this simulation shows that, with the RSFA, it is possible to reliably reconstruct the coupled beta functions from response sets as small as $S = 20$ and in the presence of noise while the COBEA workaround fails for $S < 56$. For large set sizes $S \geq 80$, the COBEA workaround and the RSFA are similarly accurate.
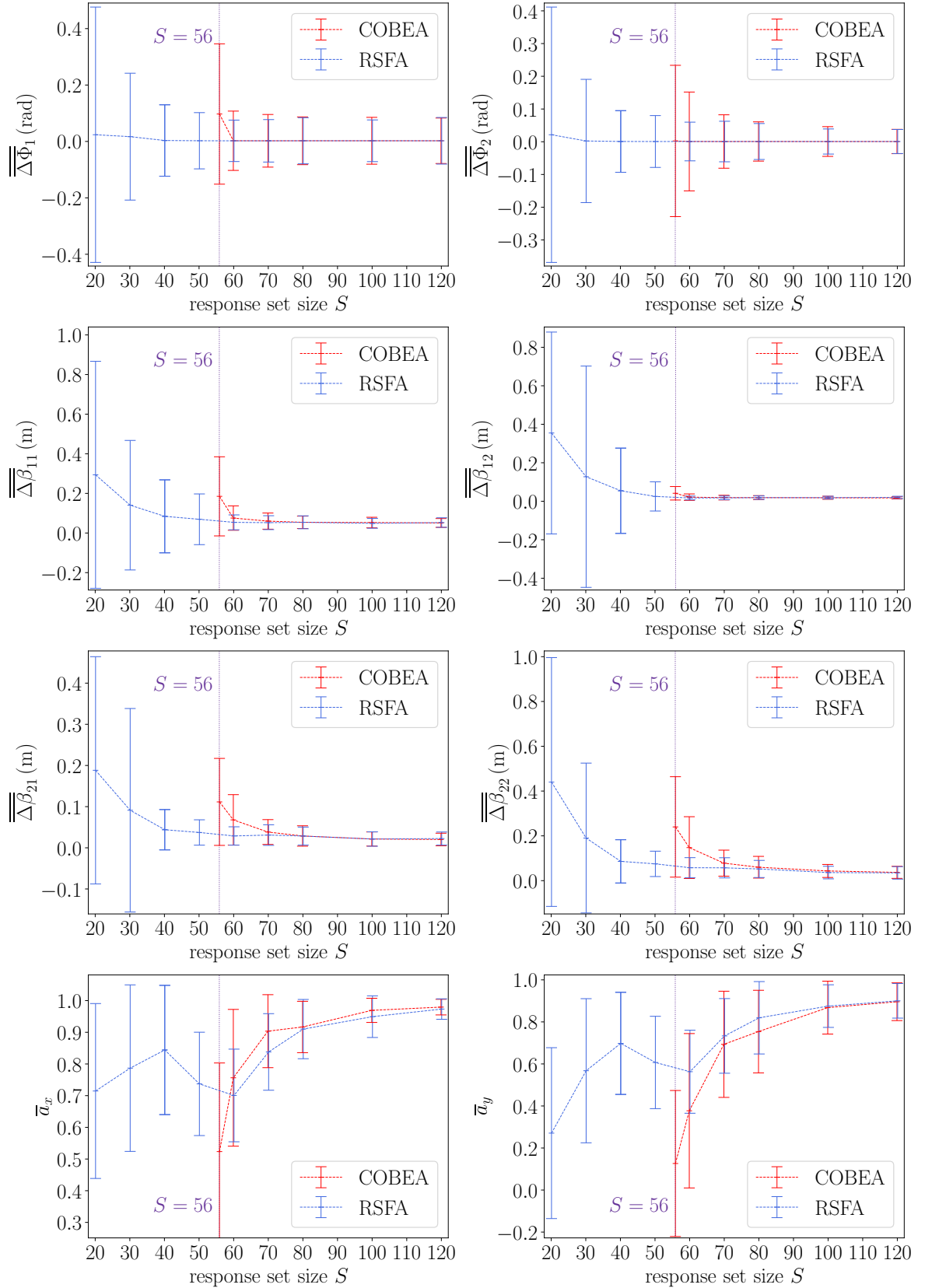
Figure 10.4: Comparison of COBEA and RSFA results for fits on simulated response sets. Left and right side: horizontal and vertical quantities. From top to bottom: betatron phase Eq. (10.7) with error bars Eq. (10.8), beta function Eq. (10.9) with error bars Eq. (10.10) as well as dispersion similarity product Eq. (10.12) with error bars Eq. (10.13). The COBEA workaround does not produce any results for set sizes $S < 56$ because the linear fit, which is required for the workaround, becomes underconstrained.

11 Experimental Results for the Response Set Fit Algorithm

COBEA (see Ch. 8) was compared to the RSFA (see Ch. 9) in two simulation studies in Ch. 10. In the following, the RSFA is used on experimental data to compare its fit results to other optical function measurements and to evaluate the impact of the superconducting asymmetric wiggler (SCW) on user optics.

11.1 Comparison with other Sources

The ability of the RSFA to reconstruct optical functions from random steerer magnet-induced orbit shifts is evaluated in the following. For that purpose, RSFA fit results for the beta function, the betatron phase and the scaled dispersion are compared to the Twiss parameter estimates from three other sources. These are uncoupled beta function measurements in quadrupoles, OCELOT [54] calculations from the model server [53] and dispersion measurements. The model server calculations are based on the real quadrupole strengths of the storage ring (see Ch. 2.4 for an explanation).

11.1.1 Measurement

The basis for the RSFA analysis was a response set with 1300 entries recorded without the static orbit bump in machine-study optics (see Ch. 2.2.5 for details on operation modes) to keep the effect of non-linear magnetic fields, mainly a sextupole in the injection area, and non-linear BPM readings on the measurement to a minimum. Each response set entry was acquired by disturbing all steerer magnets (see Ch. 2.2.3) in a range of $\pm 10\,\mathrm{mA}$ ($\approx 0.03\,\mathrm{mrad}$ for horizontal and $\approx 0.01\,\mathrm{mrad}$ for vertical steerers) and recording the orbit shift. The SCW was turned off during the measurements. The beta function measurements in the quadrupoles were conducted by varying the coil currents of the quadrupoles via the relay cascade by $0.7\,\%$ one quadrupole at a time (see Ch. 2.4.1 for details) and recording the tune shift measured by the kicker-based tune measurement system [43] (see Ch. 2.2.4). After determining the change in quadrupole strength via the i2k conversion script [12] from the coil currents, the uncoupled average horizontal and vertical beta functions in the quadrupoles were calculated according to Eq. (2.23). The measurement was repeated three times. A scaled dispersion at all BPMs was measured by detuning the RF frequency and measuring the resulting orbit. The quadrupole currents were recorded as well and used to obtain optical function estimates from the model server. The SCW model of the model server was turned off.

11.1.2 Fits with the Response Set Fit Algorithm

The RSFA was developed to calculate optical function estimates from orbit corrections in an online fitting process. To simulate this task, the RSFA was applied to 100 response subsets of size $S = 20$ selected randomly from the larger 1300-entries response set. The subset size was chosen as a trade-off between as small as possible to speed up the availability of the measurement in a possible future online model and as large as necessary to increase the accuracy of the fits. The simulation study presented in Ch. 10.3 suggests a set size of $S = 20$ as a good trade-off. In an online model sourcing the response set from the orbit correction software, the optical function estimates would then be available after 20 sufficiently large orbit corrections. BPM01, BPM06, BPM09, BPM12, BPM19, BPM34, BPM43 and BPM45 were excluded from the analysis presented in the following. Their inclusion increased the standard deviations of the fits. The same BPMs were also commented out in the orbit correction software in user operation when the measurements were conducted. BPM12 has a faulty pickup electrode. The other BPMs are known to suffer from measurement noise. Additionaly, two of the 100 fits were discarded for being obviously diverged ($\beta_{11} < \beta_{21}$ and/or $\beta_{22} < \beta_{12}$).

11.1.3 Results

The comparison of the RSFA fit results to the other optical function measurements is presented in Fig. 11.1. The fit results for the betatron phase in the horizontal plane match the model server calculations very well. In the vertical plane, the match is still good but the slope of the fitted betatron phase is a little smaller than the slope calculated by the model server. The beta function estimates of the RSFA fits and the quadrupole measurements correspond well in both planes but, in the horizontal plane, the model server prediction differs considerably. The difference is most notable around the undulator U250 from $s = 20\,\text{m}$ to $40\,\text{m}$. Here, the RSFA and quadrupole measurement peak at a beta function of around $25\,\text{m}$ to $30\,\text{m}$ while the model server prediction is $< 20\,\text{m}$. This relationship reverses in the remaining part of the storage ring where the model server predicts larger beta function values than both the RSFA and the quadrupole measurement. The vertical beta function calculations of the model server match the RSFA and quadrupole measurement results a lot better. Still, the peaks around the U250 predicted by the model server are significantly larger than the measurement results. In both planes, the measurements indicate an asymmetry of the beta function around the U250 that is not present in the model server calculations. In the north of the storage ring, the asymmetry can be attributed to sextupoles [95]. The asymmetry in the south is still under investigation. It may be a result of quadrupole alignment errors. In terms of dispersion, the model server estimate and the dispersion measurement match decently while the RFSM fit hardly reflects the measurement at all. For small response set sizes, the lacking accuracy of the dispersion fit also appeared in the simulation study (see Fig. 10.4). It can be attributed to the small size of the dispersion term in the fitted BE+d model Eq. (8.3) that is usually in the lower one-digit percentage range of the euclidean norm of a target ORM with good signal-to-noise ratio. The small size makes the term difficult to fit if the noise level increases.
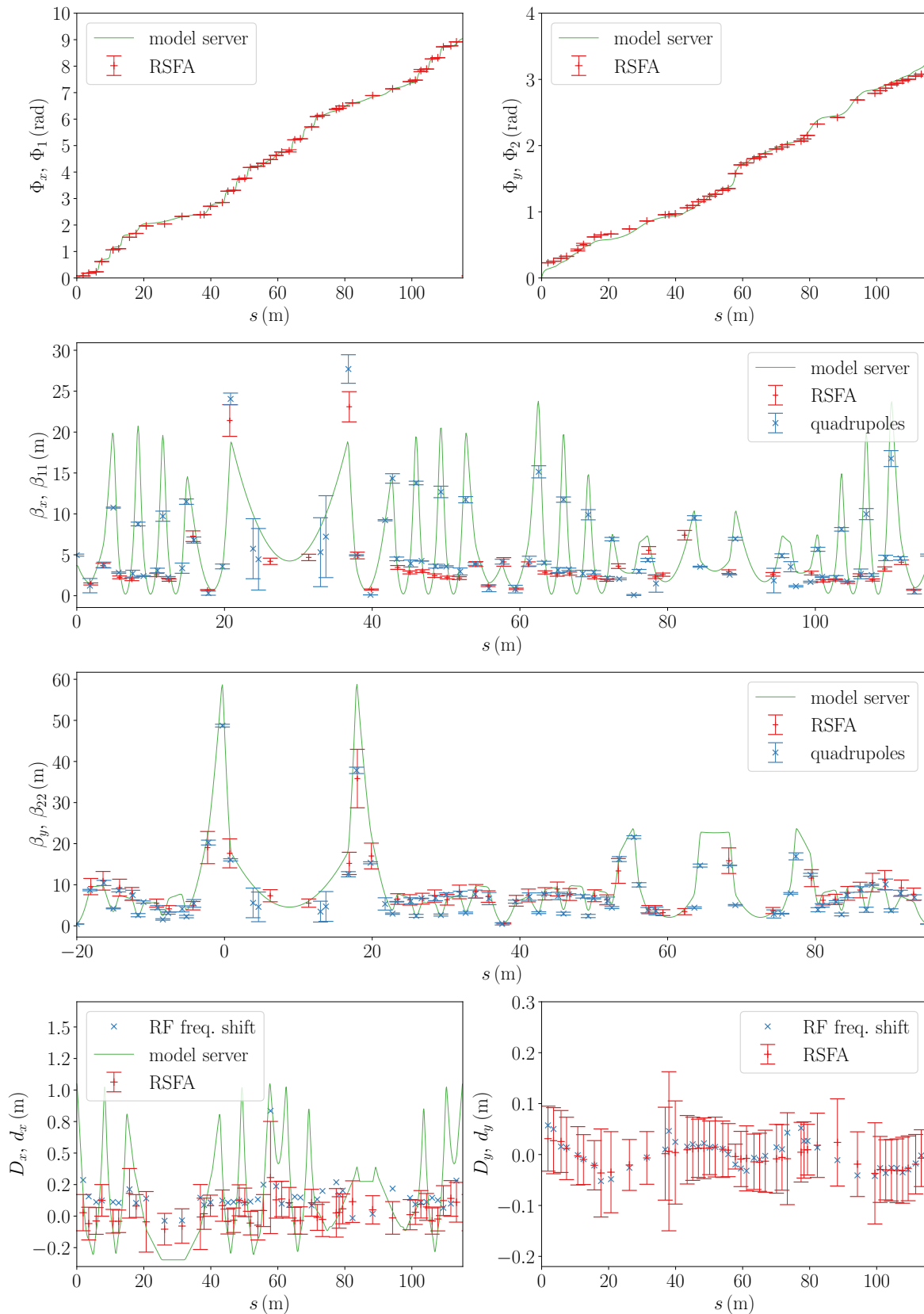
Figure 11.1: Comparison of RSFA fit results and optical function measurements from three other sources (see legends) without the static orbit bump in machine-study optics (see Ch. 2.2.5 for details on operation modes). From top to bottom: betatron phase, beta function and dispersion. The errors are standard deviations calculated from 100 fits for the RSFA and 3 measurements for the quadrupole beta function measurement. The coupled beta function values β_{12} and β_{21} resulting from the RSFA fits are not shown because there is nothing to compare them to.

11.2 SCW Optics Impact

In October 2020, the superconducting asymmetric wiggler (SAW) was replaced with a new wiggler, the SCW [10] (see Ch. 2.2.1 for details). Wigglers can be viewed as concatenations of dipole magnets whose fringe fields affect vertical focusing [66]. The impact of the SCW on the user optics (see Ch. 2.2.5 for details on operation modes) is assessed here by comparing the beta function and betatron phase estimates from RSFA fits of measured ORMs for different SCW field-strength settings.

11.2.1 Measurement

Five ORMs were measured in user optics for SCW field-strength settings of $0\,\mathrm{T}$, $2\,\mathrm{T}$, $4\,\mathrm{T}$, $5.3\,\mathrm{T}$ and $7\,\mathrm{T}$. The tunes were kept constant at $q_x = 0.11$ and $q_y = 0.23$ using the automated tune correction of the storage ring [43] (see Ch. 2.2.4 for details). With each ORM, a dispersion function was recorded as well to validate the corresponding RSFA fit. The orbit correction during the ORM measurement for the largest SCW setting was not optimal due to the vertical steerer strength being insufficient to compensate the kick applied by the wiggler. The kick is a result of the SCW's non-zero magnetic-flux-density integral along the wiggler's axis [96]. The strength of the kick increases with the SCW setting. As the measurement was conducted soon after the wiggler was installed, the vertical steerer magnet meant to correct the kick was not operational yet.

11.2.2 Analysis

The tunes were kept constant during the RSFA fits. BPM01, BPM12 and BPM33 were excluded from the analysis for jittering or not returning a signal. The RSFA betatron phase advance and beta function results for the ORM recorded at the SCW setting $0\,\mathrm{T}$, $\Phi_{mj}^{(0)}$ and $\beta_{mwj}^{(0)}$, are compared to the RSFA betatron phase and beta function results Φ_{mj}^{SCW} and $\beta_{mwj}^{\mathrm{SCW}}$ for the four ORMS recorded at the SCW settings $>0\,\mathrm{T}$ by calculating the betatron phase advance deviations

$$\Delta\Phi_{mj} = \Phi_{mj}^{\mathrm{SCW}} - \Psi_{mj}^{(0)} \tag{11.1}$$

and the beta function deviations

$$\Delta\beta_{mwj} = \beta_{mwj}^{\mathrm{SCW}} - \beta_{mwj}^{(0)} \tag{11.2}$$

at all BPMs. The RSFA fits are validated by comparing their dispersion estimates $\vec{d}_w$ to the measured dispersion values $\vec{D}_w$ via a similarity product

$$a_w = \frac{\vec{D}_w^{\mathrm{T}} \vec{d}_w}{\left\|\vec{D}_w\right\|^2 \cdot \left\|\vec{d}_w\right\|^2} \tag{11.3}$$

for all SCW settings. As mentioned before, the product is 1 if the shapes are the same, -1 if the shapes match but the fitted dispersion is flipped as in $\vec{d}_w \to -\vec{d}_w$ and 0 if the shapes do not match at all.

11.2.3 Results

The betatron phase and beta function results are shown in Fig. 11.2. The changes in the horizontal betatron phase advance are mostly related to noise. This is expected as the SCW should only affect the vertical focusing. The changes in the vertical phase advance are significant and follow a clear trend: the larger the SCW setting, the larger the changes in the vertical betatron phase.

The impact of SCW operation on the horizontal beta function is mostly limited to the northern and southern straight. Although larger SCW settings induce larger changes overall, a clear trend is not recognizable. The horizontal betatron mode seems to pick up some of the vertical focusing changes induced by the wiggler. The vertical beta function incurs large changes that follow a similar trend as the changes in the vertical betatron phase: the larger the SCW setting, the larger the beta function changes. The trend is in line with the changes in betatron phase deviations. The analysis results for the secondary coupled beta functions $\Delta\beta_{21}$ and $\Delta\beta_{12}$ also point to an increase of transverse coupling for larger SCW settings.

The similarity product of the measured dispersion functions and the fitted dispersion values presented in Fig. 11.3 is solely shown to validate the fit results. As the scaled dispersion is the fit parameter that is most susceptible to noise, a good dispersion fit of the RSFA should assert
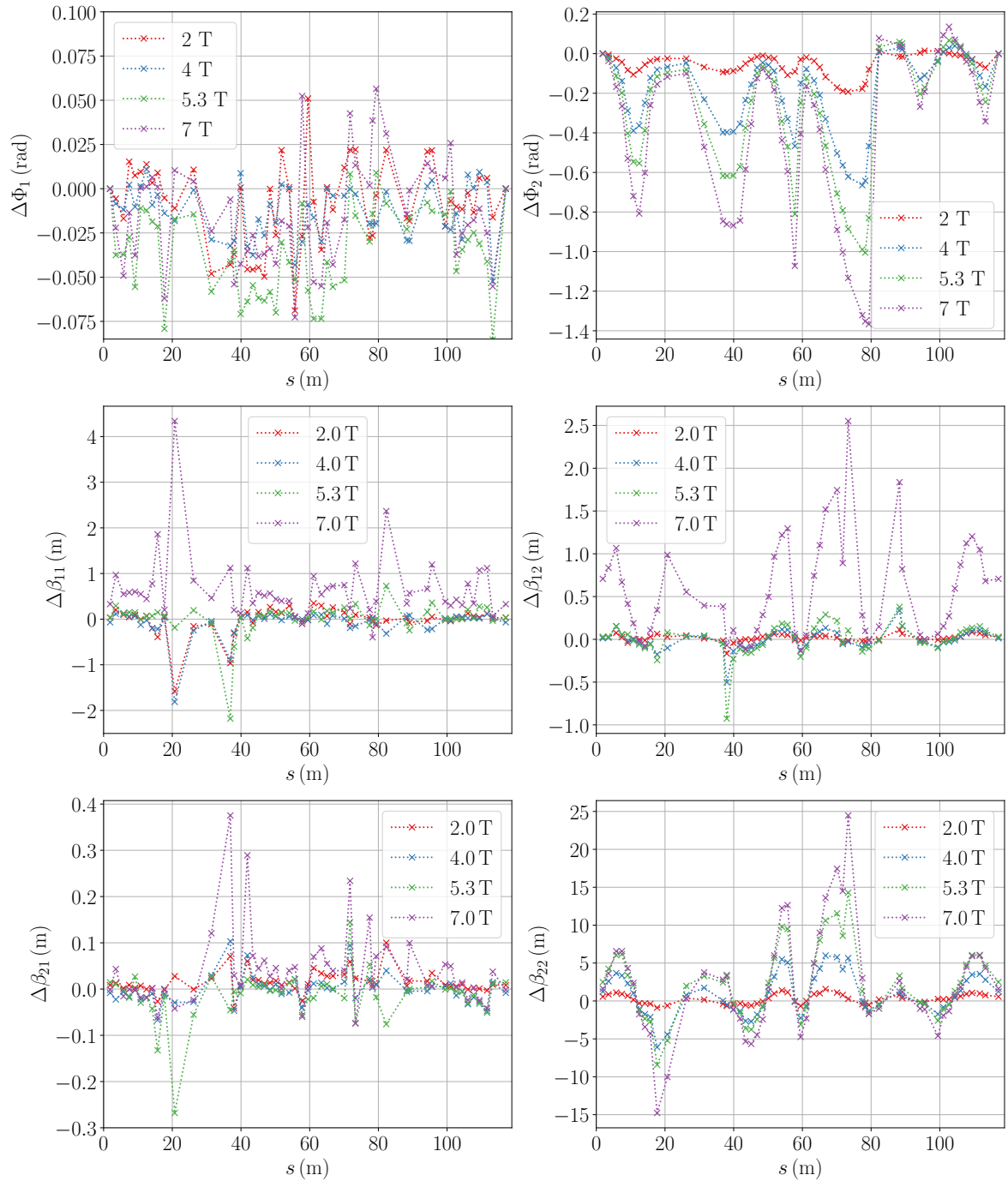
Figure 11.2: Twiss parameter changes in user optics for different SCW field-strength settings. Left and right side: horizontal and vertical quantities. From top to bottom: changes in betatron phase and beta function according to Eq. (11.1) and Eq. (11.2). The wiggler is located between BPM40 and BPM41 at $s \approx 80\,\mathrm{m}$ (see Fig. 2.7).
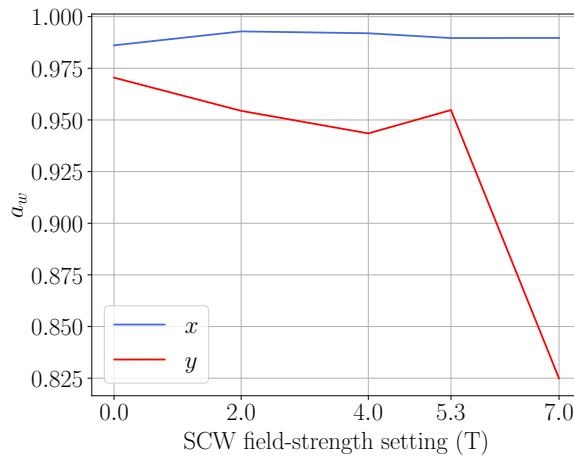
Figure 11.3: Dispersion similarity Eq. (11.3) for all analyzed SCW field-strength settings in user optics.

trustworthiness of its betatron phase and beta function estimates. The similarity products indicate that the dispersion measurement and the RSFA results for the horizontal dispersion are practically the same. The fitted vertical dispersion estimates match the measurements less well. In general, this is to be expected because the vertical dispersion is very small and therefore hard to fit. The only worry seems to be the similarity product for the SCW setting of $7\,\mathrm{T}$ as it is significantly worse than the rest. It is probably a result of the uncorrected orbit (see explanation in Ch. 11.2.1) being affected by non-linearities (sextupoles, BPM readings) and points to a lesser fit quality of the corresponding beta function and betatron phase estimates produced by the RSFA. This shows in the overly large beta function deviations $\Delta\beta_{11}(7\,\mathrm{T})$, $\Delta\beta_{12}(7\,\mathrm{T})$ and $\Delta\beta_{21}(7\,\mathrm{T})$ in Fig. 11.2. The results were not discarded because the vertical betatron phase and beta function estimates $\Delta\Phi_1(7\,\mathrm{T})$ and $\Delta\beta_{11}(7\,\mathrm{T})$ still fit neatly into the trend set by the measurements for the smaller SCW field-strength settings.

12 Conclusion

12.1 Summary

In this work, new methods for low-frequency (slow) orbit and energy correction as well as the feasibility of an online optics model are investigated at DELTA. The bilinear-exponential (BE) model-based online fit could extract Twiss parameters from orbit changes applied by the slow orbit feedback (SOFB) in the future.

A new orbit correction software (see Ch. 5) was implemented, tested and commissioned for routine operation. It automatically switches between a local (most effective steerer magnet) and a global (all steerer magnets) orbit correction method to combine the advantages of both paradigms. With this feature, the new software provides a more stable orbit than the former program commissioned in 2004 with its global-only approach (see Ch. 7). For the necessary calculations, the new software relies on an interior point method (IPM) for constrained convex optimization. The linear equality and inequality constraints accepted by the IPM were used in additional features the old program mostly did not have. These are a software aperture, unique settings for linearly dependent steerer magnets and two methods for energy correction. The first originates from the ESRF and is also used at BESSY II, the MLS and at KARA. It stabilizes the beam energy which is useful to prevent spectra of narrow-banded undulators from drifting during operation. Although the method's implementation was shown to correct beam energy perturbations caused by frequency changes of the radiofrequency (RF) resonator (see Ch. 7.2), the storage ring requires more steerer magnets to use the so-called energy-stabilizing mode to full capacity. The second method for energy correction is new and finds the shortest orbit fitting a given reference. After it was demonstrated to work in a simulation of DELTA under random steerer strength perturbations (see Ch. 6), the orbit-shortening mode was also validated at the real storage ring (see Ch. 7.3). Here, it proved capable of automating part of the switching process between user and machine-study optics (see Ch. 2.2.5 for the optics settings).

An algorithm extracting optics information from data generated in orbit corrections, the response set fit algorithm (RSFA, see Ch. 9), was implemented and tested in simulations as well as measurements. The RSFA takes the idea behind the closed-orbit bilinear-exponential analysis (COBEA) algorithm (see Ch. 8) and generalizes it to new input data. COBEA decomposes orbit response matrices (ORMs) into estimates for the coupled beta functions, betatron phase advances as well as scaled dispersion values at all BPMs by fitting the BE model with dispersion. The RSFA can extract the same quantities from reponse sets (see Ch. 9.1 for details). As these sets could, unlike ORMs, be measured by the orbit correction software when correct-

ing the orbit, the RSFA could provide optical function estimates during operation without a dedicated measurement (BE online model). COBEA and the RSFA were benchmarked in two simulation studies based on an optics model of DELTA (see Ch. 10). In the first study, both algorithms produced good estimates for the coupled beta functions and the coupled betatron phase advances at all BPMs in the presence of strong transverse coupling. In the second study, response sets were simulated and used as input for the RSFA and a two-step approach of a linear ORM fit and consecutive application of COBEA. Here, the RSFA proved superior in producing optical function estimates for small set sizes. The new algorithm was also validated experimentally by comparing its fit results to beta function measurements in quadrupoles, dispersion measurements and model server calculations (see Ch. 11.1). Even for a small amount of input data, it produced reliable Twiss parameter estimates. Finally, the RSFA was used to evaluate the optics impact of the superconducting wiggler, installed in 2020, on the vertical beta function and betatron phase advance (see Ch. 11.2).

12.2 Outlook

The replacement of the steerer magnet's power sources used in the SOFB is investigated at the time of writing. The new power sources will make it possible to build a controller that ramps these steerer magnets coherently with the steerer magnets of the fast orbit feedback (FOFB) [46]. Such a ramp controller will allow to include the fast steerer magnets for orbit corrections in the SOFB and thereby increase the number of horizontal steerer magnets by 16 to 46. If 9 of DELTA's 54 BPMs will additionally be excluded from orbit correction, the number of steerers in the SOFB will be equal to the number of BPMs making the BPM weights superfluent. In this case, the new software's energy-stabilizing mode, which was introduced in Ch. 5.3.1, will work in user operation. Problems could arise from the lower maximum steerer strength of the fast steerer magnets (about 1/10th of the SOFB magnets).

After the RSFA was shown to produce beta function and betatron phase estimates for small response set sizes (see simulation study in Ch. 10.3 and experimental comparison in Ch. 11.1), an actual implementation of a BE online model based on the RSFA that reads response set entries from orbit corrections via the new orbit correction software seems plausible. The online model will provide access to a symbiotic measurement of optical functions when conducting machine studies as long as a sufficient number of orbit corrections are applied. The results presented in this work suggest that reliable Twiss parameter estimates could then be available after as few as 20 corrections.

13 Appendix A: Systems of Equations

13.1 Corrector-Monitor Mapping on Orbit Response Matrices

13.1.1 System of Equations for the Steerer Parameters

A possible substructure of the first system of equations (8.11) required for corrector-monitor (CM) mapping on ORMs is described in the following. Although it differs from the substructure chosen in the description of the COBEA algorithm [13], the resulting system of equations yields the same results. Using the indices m, w, j and k as well as their bounds M, W, J and K explained in Ch. 8.1, the system of equations can be composed of a vector of length WJK

$$\vec{A}^{\mathrm{I}} = (\boldsymbol{a}_1^{\mathrm{I}},\, \boldsymbol{a}_W^{\mathrm{I}})^{\mathrm{T}} \tag{13.1}$$

consisting of $(1 \times JK)$-matrices

$$\boldsymbol{a}_w^{\mathrm{I}} = ((R_{w11} \,\cdots\, R_{w1K}) \,\cdots\, (R_{wJ1} \,\cdots\, R_{wJK})), \tag{13.2}$$

a vector of length MK

$$\vec{C}^{\mathrm{I}} = ((A_{11},\, A_{M1}) \,\cdots\, (A_{1K},\, A_{MK}))^{\mathrm{T}} \tag{13.3}$$

and a $(WJK \times MK)$-matrix

$$\boldsymbol{B}^{\mathrm{I}} = \begin{pmatrix} \boldsymbol{b}_{11}^{\mathrm{I}} \\ \vdots \\ \boldsymbol{b}_{1J}^{\mathrm{I}} \\ \boldsymbol{b}_{W1}^{\mathrm{I}} \\ \vdots \\ \boldsymbol{b}_{WJ}^{\mathrm{I}} \end{pmatrix} \tag{13.4}$$

consisting of $(K \times MK)$-matrices

$$\boldsymbol{b}_{wj}^{\mathrm{I}} = \begin{pmatrix} (Z_{1wj}E_{1j1},\, Z_{Mwj}E_{Mj1}) & & 0 \\ & \ddots & \\ 0 & & (Z_{1wj}E_{1jK},\, Z_{Mwj}E_{MjK}) \end{pmatrix}. \tag{13.5}$$

13.1.2 SYSTEM OF EQUATIONS FOR THE BPM PHASORS

A possible substructure of the second system of equations (8.14) required for CM mapping on ORMs is described in the following. Although it differs from the substructure chosen in the description of the COBEA algorithm [13], it yields the same results. Using the indices m, w, j and k as well as their bounds M, W, J and K explained in Ch. 8.1, the system of equations can be composed of a vector of length WJK

$$\vec{A}^{\mathrm{II}} = \left(\boldsymbol{a}_1^{\mathrm{II}} \;\; \cdots \;\; \boldsymbol{a}_K^{\mathrm{II}} \right)^{\mathrm{T}} \tag{13.6}$$

consisting of $(1 \times WJ)$-matrices

$$\boldsymbol{a}_k^{\mathrm{II}} = ((R_{11k},\, R_{W1k}) \;\; \cdots \;\; (R_{1Jk},\, R_{WJk})), \tag{13.7}$$

a vector of length MWJ

$$\vec{C}^{\mathrm{II}} = ((Z_{111},\, Z_{M11},\, Z_{1W1},\, Z_{MW1}) \cdots (Z_{11J},\, Z_{M1J},\, Z_{1WJ},\, Z_{MWJ}))^{\mathrm{T}} \tag{13.8}$$

and a $(WJK \times MWJ)$-matrix

$$\boldsymbol{B}^{\mathrm{II}} = \begin{pmatrix} \begin{pmatrix} \boldsymbol{b}_{11}^{\mathrm{II}} & & 0 \\ & \ddots & \\ 0 & & \boldsymbol{b}_{1J}^{\mathrm{II}} \end{pmatrix} \\ \vdots \\ \begin{pmatrix} \boldsymbol{b}_{K1}^{\mathrm{II}} & & 0 \\ & \ddots & \\ 0 & & \boldsymbol{b}_{KJ}^{\mathrm{II}} \end{pmatrix} \end{pmatrix} \tag{13.9}$$

consisting of $(W \times M)$-matrices

$$\boldsymbol{b}_{jk}^{\mathrm{II}} = \begin{pmatrix} A_{1k}E_{1jk} & A_{Mk}E_{Mjk} & 0 & 0 \\ 0 & 0 & A_{1k}E_{1jk} & A_{Mk}E_{Mjk} \end{pmatrix}. \tag{13.10}$$

13.2 CORRECTOR-MONITOR MAPPING ON RESPONSE SETS

13.2.1 SYSTEM OF EQUATIONS FOR THE STEERER PARAMETERS

Considering the indices m, w, j and k as well as their bounds M, W, J and K explained in Ch. 8.1 in addition to the index i and its bound I introduced in Ch. 9.1, the first system of equations (9.15) required for CM mapping on response sets comprises a vector of length WJI

$$\vec{\mathcal{A}}^{\text{I}} = \begin{pmatrix} \boldsymbol{a}_1^{\text{I}} & \cdots & \boldsymbol{a}_I^{\text{I}} \end{pmatrix}^{\text{T}} \tag{13.11}$$

consisting of $(1 \times WJ)$ matrices

$$\boldsymbol{a}_i^{\text{I}} = (\mathcal{R}_{11i} \ \cdots \ R_{1Ji}, \ \mathcal{R}_{W1i} \ \cdots \ R_{WJi}), \tag{13.12}$$

a vector of length MK

$$\vec{\mathcal{C}}^{\text{I}} = (A_{11} \ \cdots \ A_{1K}, \ A_{M1} \ \cdots \ A_{MK})^{\text{T}} \tag{13.13}$$

and a $(WJI \times MK)$-matrix

$$\boldsymbol{\mathcal{B}}^{\text{I}} = \begin{pmatrix} \begin{pmatrix} \boldsymbol{b}_{1i}^{\text{I}} \\ \boldsymbol{b}_{Wi}^{\text{I}} \end{pmatrix} \\ \vdots \\ \begin{pmatrix} \boldsymbol{b}_{1I}^{\text{I}} \\ \boldsymbol{b}_{WI}^{\text{I}} \end{pmatrix} \end{pmatrix} \tag{13.14}$$

consisting of $(J \times MK)$-matrices

$$\boldsymbol{b}_{wi}^{\text{I}} = \begin{pmatrix} \theta_{1i}Z_{1w1}E_{111} & \cdots & \theta_{Ki}Z_{1w1}E_{11K}, \ \theta_{1i}Z_{Mw1}E_{M11} & \cdots & \theta_{Ki}Z_{Mw1}E_{M1K} \\ & & \vdots & & \\ \theta_{1i}Z_{1wJ}E_{1J1} & \cdots & \theta_{Ki}Z_{1wJ}E_{1JK}, \ \theta_{1i}Z_{MwJ}E_{M1J} & \cdots & \theta_{Ki}Z_{MwJ}E_{MJK} \end{pmatrix}. \tag{13.15}$$

13.2.2 SYSTEM OF EQUATIONS FOR THE BPM PHASORS

Considering the indices m, w, j and k as well as their bounds M, W, J and K explained in Ch. 8.1 in addition to the index i and its bound I introduced in Ch. 9.1, the second system of equations (9.18) required for CM mapping on response sets comprises a vector of length WJI

$$\vec{\mathcal{A}}^{\text{II}} = \begin{pmatrix} \boldsymbol{a}_1^{\text{II}} & \cdots & \boldsymbol{a}_I^{\text{II}} \end{pmatrix}^{\text{T}} \tag{13.16}$$

consisting of $(1 \times WJ)$ matrices

$$\boldsymbol{a}_i^{\text{II}} = ((\mathcal{R}_{11i}, \ R_{W1i}) \ \cdots \ (\mathcal{R}_{1Ji}, \ R_{WJi})), \tag{13.17}$$

a vector of length MWJ

$$\vec{\mathcal{C}}^{\mathrm{II}} = ((Z_{111}, Z_{M11}, Z_{1W1}, Z_{MW1}) \cdots (Z_{11J}, Z_{M1J}, Z_{1WJ}, Z_{MWJ}))^{\mathrm{T}} \qquad (13.18)$$

and a $(WJI \times MWJ)$-matrix

$$\mathcal{B}^{\mathrm{II}} = \begin{pmatrix} \begin{pmatrix} \boldsymbol{b}^{\mathrm{II}}_{1i} & & 0 \\ & \ddots & \\ 0 & & \boldsymbol{b}^{\mathrm{II}}_{Ji} \end{pmatrix} \\ \vdots \\ \begin{pmatrix} \boldsymbol{b}^{\mathrm{II}}_{1I} & & 0 \\ & \ddots & \\ 0 & & \boldsymbol{b}^{\mathrm{II}}_{JI} \end{pmatrix} \end{pmatrix} \qquad (13.19)$$

consisting of $(W \times MW)$-matrices

$$\boldsymbol{b}^{\mathrm{II}}_{ji} = \begin{pmatrix} \left(\sum_{k=1}^{K} \theta_{ki} E_{1jk} A_{1k}, \ \sum_{k=1}^{K} \theta_{ki} E_{Mjk} A_{Mk} \right) & 0 \\ 0 & \left(\sum_{k=1}^{K} \theta_{ki} E_{1jk} A_{1k}, \ \sum_{k=1}^{K} \theta_{ki} E_{Mjk} A_{Mk} \right) \end{pmatrix}. \qquad (13.20)$$

14 Appendix B: Analytical Steerer Parameters

The description of the BE model in [13] only includes analytical expressions for the steerer parameters in the uncoupled BE model A_x and A_y. For the coupled BE model Eq. (3.10), analytical representations of the coupled steerer parameters A_m are established without derivation in [62]. In this work, they are used in the calculation of the orbit response matrix (ORM) for the simulation study presented in Ch. 6. After Ch. 3 layed the theoretical foundation, the derivation of the coupled parameters and, based on it, a comparison of the BE model to other orbit response models is presented in the following. Before that, see Ch. 8.1 for an introduction to the parameterization of the discretized BE model including an explanation of the indices m, w, j and k as well as their bounds M, W, J and K.

14.1 Derivation

On the one hand, the 4D closed orbit at a thin steerer magnet $\vec{r}(s_k)$ that deflects the beam by

$$\vec{\theta} = (0,\, \theta_1,\, 0,\, \theta_2)^{\mathrm{T}} \tag{14.1}$$

adheres to Eq. (3.11). Here, θ_w is the kick in each plane w. This was used in the formulation of the transfer map model [67] in Ch. 3.2.2. On the other hand, the closed orbit according to the BE model Eq. (3.10) is a scaled betatron oscillation. This was explained in Ch. 3.2.1. In the BE model, the steerer parameters A_m take the role of (complex) scaling factors. From the ensemble of all possible betatron trajectories, they select the mode amplitudes and the mode start phases of the single betatron trajectory that is closed by the kick and therefore becomes the new closed orbit. At the position of the steerer magnet s_k, the scaled betatron oscillation can be written as

$$\vec{r}(s_k) = \sum_m \Re\left\{ A_m \begin{pmatrix} Z_{m1}(s_k) \\ Z'_{m1}(s_k) \\ Z_{m2}(s_k) \\ Z'_{m2}(s_k) \end{pmatrix} \right\}. \tag{14.2}$$

Inserting this ansatz into Eq. (3.11) and using

$$\sin(\pi q_m) = \frac{1}{2i}\left(e^{i\pi q_m} - e^{-i\pi q_m} \right) \tag{14.3}$$

while absorbing a factor $e^{i\pi q_m}$ into the eigenvector gives a set of W conditions

$$-2i \sum_m \Re \left\{ \begin{matrix} Z_{mw}(s_k) A_m \\ Z'_{mw}(s_k) A_m \end{matrix} \right\} \sin(\pi q_m) = \begin{pmatrix} 0 \\ \theta_w \end{pmatrix}. \tag{14.4}$$

These are further simplified by substituting

$$\hat{A}_m = -i A_m \sin(\pi q_m), \tag{14.5}$$

which results in W spatial conditions

$$2\Re \left\{ Z_{1w}(s_k) \hat{A}_1 \right\} + 2\Re \left\{ Z_{2w}(s_k) \hat{A}_2 \right\} = 0 \tag{14.6}$$

and W momentum conditions

$$2\Re \left\{ Z'_{1w}(s_k) \hat{A}_1 \right\} + 2\Re \left\{ Z'_{2w}(s_k) \hat{A}_2 \right\} = \theta_w. \tag{14.7}$$

Together, the conditions contain M complex unknowns $\hat{A}_m$ with two degrees of freedom for each mode: one degree of freedom corresponds to the real part $\Re\{\hat{A}_m\}$ and one to the imaginary part $\Im\{\hat{A}_m\}$. Thus, the number of equations $2W = 4$ is equal to the number of real unknows $2M = 4$.

14.1.1 System of Equations

The real part of a complex number $z = a + ib$ can be written as $a = 1/2(z + z^*)$. Applying this to the spatial and momentum conditions yields

$$Z_{1wk} \hat{A}_1 + Z^*_{1wk} \hat{A}_1^* + Z_{2wk} \hat{A}_2 + Z^*_{2w} \hat{A}_2^* = 0 \tag{14.8}$$

$$Z'_{1wk} \hat{A}_1 + Z^{*\prime}_{1wk} \hat{A}_1^* + Z'_{2wk} \hat{A}_2 + Z^{*\prime}_{2wk} \hat{A}_2^* = \theta_w. \tag{14.9}$$

Here, the phasors at the position of the steerer magnet $Z_{mw}(s_k)$ have been substituted by $Z_{mw}(s_k) = Z_{mwk}$ to increase the readability. The $\hat{A}_m$ can now be separated from the phasors by reformulating Eq. (14.8) as a system of equations. This is achieved by collecting the phasors in a coefficent matrix

$$\boldsymbol{M} = \begin{pmatrix} Z_{11k} & Z^*_{11k} & Z_{21k} & Z^*_{21k} \\ Z'_{11k} & Z'^*_{11k} & Z'_{21k} & Z'^*_{21k} \\ Z_{12k} & Z^*_{12k} & Z_{22k} & Z^*_{22k} \\ Z'_{12k} & Z'^*_{12k} & Z'_{22k} & Z'^*_{22k} \end{pmatrix}, \tag{14.10}$$

stacking the steerer parameters into a vector

$$\vec{A} = \left(\hat{A}_1, \ \hat{A}_1^*, \ \hat{A}_2, \ \hat{A}_2^* \right)^{\mathrm{T}} \tag{14.11}$$

and rewriting the spatial and momentum conditions as

$$\boldsymbol{M}\vec{A} = \vec{\theta}. \tag{14.12}$$

All complex systems of equations of the form $\boldsymbol{a}\vec{x} = \vec{b}$ can be solved using Cramer's rule [69]. The result is the desired but not-yet normalized analytical expression for the steerer parameters

$$A_m(S_{mwk}) = A_{mk} = \frac{i\sum_w \theta_w S_{mwk}}{\sin(\pi q_m)\det(\boldsymbol{M})}, \tag{14.13}$$

where the complex scalars

$$S_{11k} = \det\begin{pmatrix} Z^*_{11k} & Z_{21k} & Z^*_{21k} \\ Z^*_{12k} & Z_{22k} & Z^*_{22k} \\ Z'^*_{12k} & Z'_{22k} & Z'^*_{22k} \end{pmatrix} \qquad S_{12k} = \det\begin{pmatrix} Z^*_{11k} & Z_{21k} & Z^*_{21k} \\ Z'^*_{11k} & Z'_{21k} & Z'^*_{21k} \\ Z^*_{12k} & Z_{22k} & Z^*_{22k} \end{pmatrix} \tag{14.14}$$

$$S_{21k} = \det\begin{pmatrix} Z_{11k} & Z^*_{11k} & Z^*_{21k} \\ Z_{12k} & Z^*_{12k} & Z^*_{22k} \\ Z'_{12k} & Z'^*_{12k} & Z'^*_{22k} \end{pmatrix} \qquad S_{22k} = \det\begin{pmatrix} Z_{11k} & Z^*_{11k} & Z^*_{21k} \\ Z'_{11k} & Z'^*_{11k} & Z'^*_{21k} \\ Z_{12k} & Z^*_{12k} & Z^*_{22k} \end{pmatrix}. \tag{14.15}$$

encode the amplitudes and phases of the betatron oscillation at the position of the steerer magnet k. Similar to the analytical expressions for the steerer parameters in the uncoupled BE model A_x and A_y given in [13], the coupled steerer parameters Eq. (14.13) only work for thin steerer magnets. The BE model also applies to thick steerer magnets.

14.2 Normalization

After collecting the phasors in vectors

$$\vec{Z}_{mk} = \left(Z_{m1k},\, Z'_{m1k},\, Z_{m2k},\, Z'_{m2k}\right)^{\mathrm{T}}, \tag{14.16}$$

that are equivalent to the eigenvectors of the one-turn transfer map in the position of the steerer magnet $\boldsymbol{T}_{s_k \to s_k}$, the determinant of the coefficient matrix can be written as

$$\det(\mathbf{M}) = \det\left(\left[\vec{Z}_{1k},\, \vec{Z}^*_{1k},\, \vec{Z}_{2k},\, \vec{Z}^*_{2k}\right]\right) \tag{14.17}$$

$$= \det\left(\left[\Re\{\vec{Z}_{1k}\} + i\Im\{\vec{Z}_{1k}\},\, \Re\{\vec{Z}_{1k}\} - i\Im\{\vec{Z}_{1k}\},\, \vec{Z}_{2k},\, \vec{Z}^*_{2k}\right]\right). \tag{14.18}$$

Iteratively applying the associative law in the context of determinants

$$\det\left(\left[\vec{a} + \vec{b}, \vec{c}, \vec{d}\right]\right) = \det\left(\left[\vec{a}, \vec{c}, \vec{d}\right]\right) + \det\left(\left[\vec{b}, \vec{c}, \vec{d}\right]\right) \tag{14.19}$$

to the determinant then yields

$$\det(\mathbf{M}) = \det\left(\left[\Re\left\{\vec{Z}_{1k}\right\}, \Re\left\{\vec{Z}_{1k}\right\} - i\Im\left\{\vec{Z}_{1k}\right\}, \vec{Z}_{2k}, \vec{Z}_{2k}^*\right]\right) \tag{14.20}$$

$$+ \det\left(\left[i\Im\left\{\vec{Z}_{1k}\right\}, \Re\left\{\vec{Z}_{1k}\right\} - i\Im\left\{\vec{Z}_{1k}\right\}, \vec{Z}_{2k}, \vec{Z}_{2k}^*\right]\right) \tag{14.21}$$

$$= \det\left(\left[\Re\left\{\vec{Z}_{1k}\right\}, \Re\left\{\vec{Z}_{1k}\right\}, \vec{Z}_{2k}, \vec{Z}_{2k}^*\right]\right) \tag{14.22}$$

$$+ \det\left(\left[\Re\left\{\vec{Z}_{1k}\right\}, -i\Im\left\{\vec{Z}_{1k}\right\}, \vec{Z}_{2k}, \vec{Z}_{2k}^*\right]\right) \tag{14.23}$$

$$+ \det\left(\left[i\Im\left\{\vec{Z}_{1k}\right\}, \Re\left\{\vec{Z}_{1k}\right\}, \vec{Z}_{2k}, \vec{Z}_{2k}^*\right]\right) \tag{14.24}$$

$$+ \det\left(\left[i\Im\left\{\vec{Z}_{1k}\right\}, -i\Im\left\{\vec{Z}_{1k}\right\}, \vec{Z}_{2k}, \vec{Z}_{2k}^*\right]\right). \tag{14.25}$$

Now, three additional rules for calculations with determinants are considered [69]. Firstly, let λ a complex factor of a column in the matrix of a determinant, then the determinant may be written as

$$\det\left(\left[\lambda\vec{a}, \vec{b}, \vec{c}\right]\right) = \lambda \det\left(\left[\vec{a}, \vec{b}, \vec{c}\right]\right). \tag{14.26}$$

Secondly, switching two columns of a determinant flips its sign. Thirdly, the determinant is zero if any two columns are identical. Applying these rules to the determinant of the coefficient matrix gives

$$\det(\mathbf{M}) = + \det\left(\left[\Re\left\{\vec{Z}_{1k}\right\}, -i\Im\left\{\vec{Z}_{1k}\right\}, \vec{Z}_{2k}, \vec{Z}_{2k}^*\right]\right) \tag{14.27}$$

$$+ \det\left(\left[i\Im\left\{\vec{Z}_{1k}\right\}, \Re\left\{\vec{Z}_{1k}\right\}, \vec{Z}_{2k}, \vec{Z}_{2k}^*\right]\right) \tag{14.28}$$

$$= 2i \det\left(\left[\Re\left\{\vec{Z}_{1k}\right\}, -\Im\left\{\vec{Z}_{1k}\right\}, \vec{Z}_{2k}, \vec{Z}_{2k}^*\right]\right). \tag{14.29}$$

The same procedure is used on the second eigenvector. This yields

$$\det(\mathbf{M}) = - 4 \det\left(\left[\Re\left\{\vec{Z}_{1k}\right\}, -\Im\left\{\vec{Z}_{1k}\right\}, \Re\left\{\vec{Z}_{2k}\right\}, -\Im\left\{\vec{Z}_{2k}\right\}\right]\right). \tag{14.30}$$

Due to the symplecticity of [65]

$$\boldsymbol{\mathcal{M}}(s) = \left[\Re\left\{\vec{Z}_1(s)\right\}, -\Im\left\{\vec{Z}_1(s)\right\}, \Re\left\{\vec{Z}_2(s)\right\}, -\Im\left\{\vec{Z}_2(s)\right\}\right], \tag{14.31}$$

which implies $\det(\boldsymbol{\mathcal{M}}(s)) = 1$, the final results are

$$\det(\boldsymbol{M}) = -4 \tag{14.32}$$

if Eq. (14.13) is calculated from eigenvectors normalized via Eq. (3.3) and

$$\det(\boldsymbol{M}) = -4C_1C_2 = -4\mathcal{C}^{4\mathrm{D}} \tag{14.33}$$

if not. Here, C_m are the generalized Courant-Snyder invariants of the two betatron modes (see Ch. 3.1 for details). Their product can be identified with the volume of the 4D phase space

ellipsoid $\mathcal{C}^{4D}$ created by the supersposition of the phase space ellipses of both modes [65]. A projection of the 4D ellipsoid to a 3D subspace is displayed in Fig. 3.1.

14.3 RELATION TO OTHER MODELS

The BE model Eq. (3.10) [13] with the analytical steerer parameters Eq. (14.13) and the normalization Eq. (14.32) allows to calculate the coupled orbit response in a storage ring in linear approximation from twiss parameters, their longitudinal derivatives and the order of BPMs and steerer magnets along the storage ring.

14.3.1 TRANSFER MAP MODEL

The transfer map model calculates the coupled orbit response in a storage ring in linear approximation from transfer maps. A transfer map $\boldsymbol{T}_{s_1 \to s_2}$ can be factorized into a matrix product [97]

$$\boldsymbol{T}_{s_1 \to s_2} = \boldsymbol{\mathcal{M}}(s_2)\boldsymbol{\mathcal{S}}\boldsymbol{\mathcal{M}}^{-1}(s_1) \tag{14.34}$$

of the eigenvectors Eq. (14.31) of the one-turn maps $\boldsymbol{T}_{s_1 \to s_1}$ and $\boldsymbol{T}_{s_2 \to s_2}$ as well as a rotation matrix

$$\boldsymbol{\mathcal{S}} = \begin{bmatrix} \cos(2\pi q_1) & \sin(2\pi q_1) & 0 & 0 \\ -\sin(2\pi q_1) & \cos(2\pi q_1) & 0 & 0 \\ 0 & 0 & \cos(2\pi q_2) & \sin(2\pi q_2) \\ 0 & 0 & -\sin(2\pi q_2) & \cos(2\pi q_2) \end{bmatrix} \tag{14.35}$$

that depends on the tunes q_w. Replacing the transfer maps in the transfer map model Eq. (3.12) with these matrix products gives an expression for the orbit response at any position s in the storage ring

$$\vec{r}(s) = \boldsymbol{\mathcal{M}}(s)\boldsymbol{\mathcal{S}}\boldsymbol{\mathcal{M}}^{-1}(s_k)\big(1 - \boldsymbol{\mathcal{M}}(s_k)\boldsymbol{\mathcal{S}}\boldsymbol{\mathcal{M}}^{-1}(s_k)\big)^{-1}\vec{\theta} \quad \text{for} \quad s \neq s_k \tag{14.36}$$

that only depends on the eigenvectors of the one-turn maps $\boldsymbol{T}_{s_k \to s_k}$ and $\boldsymbol{T}_{s \to s}$ as well as the tunes. The dependencies of this modified transfer map model are similar to the BE model with analytical steerer parameters. Taking into account that both models are based on the same premise Eq. (3.11) and produce nearly identical results in orbit response simulations [62], it is reasonable to assume that the transfer map model and the BE model with analytical steerer parameters are physically equivalent.

14.3.2 UNCOUPLED ORBIT RESPONSE MODEL

The first mode of a coupled betatron oscillation $m = 1$ can be equivalent to an uncoupled horizontal betatron oscillation (see Fig. 3.2). If that is the case, the horizontal component of the horizontal coupled beta function $\beta_{11}(s)$ can be identified with the uncoupled horizontal

beta function $\beta_x(s) = \beta_{11}(s)$ and the coupled betatron phase $\Phi_1(s)$ can be identified with the uncoupled horizontal betatron phase $\Phi_x(s) = \Phi_1(s)$. The eigenvector components Z_{12k} and Z_{21k}, their derivatives Z'_{12k} and Z'_{21k} and their complex conjugates in the coefficient matrices Eq. (14.14) are then zero. Under consideration of normalized eigenvectors fulfilling Eq. (3.3), the analytical expression of the steerer parameters simplifies to

$$A_1 = \frac{i}{\sin(\pi q_1)} \frac{\theta_1 \det\begin{pmatrix} Z^*_{11k} & 0 & 0 \\ 0 & Z_{22k} & Z^*_{22k} \\ 0 & Z'_{22k} & Z'^*_{22k} \end{pmatrix} + \theta_2 \det\begin{pmatrix} Z^*_{11k} & 0 & 0 \\ Z'^*_{11k} & 0 & 0 \\ 0 & Z_{22k} & Z^*_{22k} \end{pmatrix}}{-4} \tag{14.37}$$

$$= \frac{i}{\sin(\pi q_1)} \frac{\theta_1 Z^*_{11k}}{-4} \det\begin{pmatrix} Z_{22k} & Z^*_{22k} \\ Z'_{22k} & Z'^*_{22k} \end{pmatrix}. \tag{14.38}$$

The phasor in the determinant Z_{22k} and its derivative Z'_{22k} are identified with the uncoupled vertical phasor Z_{yk} and its derivative Z'_{yk} resulting in

$$\det\begin{pmatrix} Z_{22k} & Z^*_{22k} \\ Z'_{22k} & Z'^*_{22k} \end{pmatrix} = \det\begin{pmatrix} Z_{yk} & Z^*_{yk} \\ Z'_{yk} & Z'^*_{yk} \end{pmatrix} = \det\left(\begin{bmatrix} \vec{Z}_y, \vec{Z}^*_y \end{bmatrix}\right) = \det(\boldsymbol{M}_y). \tag{14.39}$$

Here, $\boldsymbol{M}_y$ is a (2×2)-matrix of the vertical 2D eigenvector $\vec{Z}_y$ and its complex conjugate $\vec{Z}^*_y$, a decoupled version of the 4D eigenvector matrix $\boldsymbol{M}$ defined in Eq. (14.10). By reusing the refomulation of the 4D determinant $\det(\boldsymbol{M})$ up to Eq. (14.27), the determinant of the 2D eigenvector matrix can be expressed as

$$\det(\boldsymbol{M}_y) = \det\left(\begin{bmatrix} \vec{Z}_y, \vec{Z}^*_y \end{bmatrix}\right) = 2i \det\left(\begin{bmatrix} \Re\{\vec{Z}_y\}, -\Im\{\vec{Z}^*_y\} \end{bmatrix}\right) = 2i \det(\boldsymbol{\mathcal{M}}_y) = 2i, \tag{14.40}$$

where $\boldsymbol{\mathcal{M}}_y$ is a symplectic matrix according to Eq. (14.31). The steerer parameter therefore is

$$Z_1 = \frac{i}{\sin(\pi q_1)} \frac{\theta_1 Z^*_{11k} \det(\boldsymbol{M}_y)}{-4} \tag{14.41}$$

$$= \frac{\theta_1 Z^*_{11k}}{2 \sin(\pi q_1)}. \tag{14.42}$$

The coupled beta function, the phase and the tune in the steerer parameters can then be identified with their decoupled counterparts resulting in

$$A_1 = \frac{\theta_1 \sqrt{\beta_{11}(s_k)} e^{-i\Phi_1(s_k)}}{2 \sin(\pi q_1)} \tag{14.43}$$

$$= \frac{\theta_x \sqrt{\beta_x(s_k)} e^{-i\Phi_x(s_k)}}{2 \sin(\pi q_x)} \tag{14.44}$$

which is the same as the steerer parameter in the uncoupled BE model derived in [13]. There, it is used to relate the uncoupled BE model to the horizontal orbit response model

$$x(s) = \frac{\theta_x \sqrt{\beta_x(s)\beta_x(s_k)}}{2\sin(\pi q_x)} \cos(|\Phi_x(s) - \Phi_x(s_k)| - \pi q_x) \tag{14.45}$$

which is widely known in accelerator physics [14][66][97]. A similar argument holds in the vertical plane.

Bibliography

[1] F. R. Elder et al., *Radiation from Electrons in a Synchrotron*, Phys. Rev. 71, pp. 829–830 (1947).

[2] J. Larmor, *A Dynamical Theory of the Electric and Luminiferous Medium*, Phil. Trans. R. Soc. Lond. 185, pp. 719–822 (1894).

[3] J. C. Maxwell, *A Dynamical Theory of the Electromagnetic Field*, Phil. Trans. R. Soc. Lond. 155, pp. 459–512 (1865).

[4] D. Iwanenko and I. Pomeranchuk, *On the Maximal Energy Attainable in a Betatron*, Phys. Rev. 65, p. 343 (1944).

[5] W. C. Röntgen, *Über eine neue Art von Strahlen*, Sitzungsberichte der physikalisch-medizinischen Gesellschaft zu Würzburg, pp. 132–146 (1895).

[6] C. J. Bocchetta, *Review of Orbit Control*, Proc. 6th European Particle Accelerator Conference, Stockholm, Sweden, pp. 28–32 (1998).

[7] E. D. Courant and H. S. Snyder, *Theory of the Alternatig Gradient Synchrotron*, Annals of Physics 281, pp. 360–408 (2000).

[8] D. W. Kerst and R. Serber, *Electronic Orbits in the Induction Accelerator*, Phys. Rev. 60, pp. 53–58 (1941).

[9] E. D. Courant, H. S. Snyder, and M. S. Livingston, *The Strong-Focusing Synchroton — A New High Energy Accelerator*, Phys. Rev. 88, pp. 1190–1196 (1952).

[10] N. A. Mezentsev et al., *Superconducting 7 Tesla Wiggler for Delta Synchrotron Radiation Source*, Proc. Russian Particle Accelerator Conference, Protvino, Russia, pp. 410–413 (2018).

[11] M. Tolan et al., *DELTA: Synchrotron light in nordrhein-westfalen*, Synchrotron Radiation News 16, pp. 9–11 (2003).

[12] M. Grewe, *Orbitkorrektur am Speicherring DELTA*, Dissertation, TU Dortmund University (2005).

[13] B. Riemann, *The Bilinear-Exponential Closed-Orbit Model and its Application to Storage Ring Beam Diagnostics*, Dissertation, TU Dortmund University (2016).

[14] K. Wille, *The Physics of Particle Accelarators*, Oxford University Press (2000).

[15] A. Glassl, *Optiksimulation an DELTA*, master's thesis, TU Dortmund University (2018).

[16] D. W. Kerst, *Acceleration of Electrons by Magnetic Induction*, Phys. Rev. 58, p. 841 (1940).

[17] M. Beckmann and V. Ziemann, *How well do we know the circumference of a storage ring?*, Nucl. Instrum. Methods in Physics Research A 771, pp. 115–120 (2015).

[18] T. Schulte-Eickhoff, DELTA, TU Dortmund University, private communication (2021).

[19] K. Wille, *Initial Experience with DELTA*, Proc. 5th European Particle Accelerator Conference, Barcelona, Spain, pp. 950–953 (1996).

[20] A. Jankowiak et al., *Reconstruction of the 75 MeV Linac of the DELTA Synchrotron-Radiation-Facility*, Proc. 7th European Particle Accelerator Conference, Vienna, Austria, pp. 634–636 (2000).

[21] D. Schirmer, *Synchrotron Radiation Sources at DELTA*, DELTA Int. Rep. 001-05, DELTA (2009).

[22] U. Berges et al., *Status of the Dortmund Electron Test Accelerator Facility*, Proc. 6th European Particle Accelerator Conference, Stockholm, Sweden, pp. 611–613 (1998).

[23] F. Marhauser et al., *HOM Damped 500 MHz Cavity Design for 3rd Generation SR Sources*, Proc. 19th Particle Accelerator Conference, Chicago, USA, pp. 846–848 (2001).

[24] P. Hartmann et al., *First Experience with DELTA's Upgraded RF System*, Proc. 23rd Annual Meeting of European RF Groups, Oxford, UK (2019).

[25] D. Nölle et al., *First lasing of the FELICITA I FEL at DELTA*, Nucl. Instrum. Methods in Physics Research A 445, pp. 128–133 (2000).

[26] H. Huck et al., *Coherent Harmonic Generation at the DELTA Storage Ring*, Proc. 33rd Free Electron Laser Conference, Shanghai, China, pp. 5–8 (2011).

[27] S. Khan et al., *Generation of Ultrashort and Coherent Synchrotron Radiation Pulses at DELTA*, Synchrotron Radiation News 26, pp. 25–29 (2013).

[28] A. Meyer auf der Heide et al., *Progress towards an EEHG-Based Short-Pulse Source at DELTA*, Proc. 8th International. Particle Accelerator Conference, Copenhagen, Denmark, pp. 2582–2585 (2017).

[29] P. Ungelenk et al., *Continuously tunable narrowband pulses in the THz gap from laser-modulated electron bunches in a storage ring*, Phys. Rev. Accel. Beams 20, pp. 1–12 in 020706 (2017).

[30] M. Negrazus and A. Peters, *SAW - A Superconducting Asymmetric Multipole Wiggler at the DELTA Storage Ring*, Proc. 5th European Particle Accelerator Conference, Barcelona, Spain, pp. 2576–2578 (1996).

[31] A. J. Kozubal et al., *Run-Time Environment and Application Tools for the Ground Test Accelerator Control System*, Nucl. Instrum. Methods in Physics Research A 293, pp. 288–291 (1990).

[32] D. Schirmer, *Entwicklung von Strahloptiken für den Testspeicherring DELTA auf Basis der Triplett-Struktur*, Diplomarbeit, TU Dortmund University (1989).

[33] T. Roy, *Optimierung des DELTA-Speicherringes für den Betrieb des neuen supraleiten-den Wigglermagneten*, Diplomarbeit, TU Dortmund University (1999).

[34] D. Schirmer, DELTA, TU Dortmund University, private communication (2020).

[35] B. Sawadski, DELTA, TU Dortmund University, private communication (2021).

[36] D. Zimoch, *Implementierung eines Orbitkorrektursystems an der Synchrotronstrahlungsquelle DELTA*, Dissertation, TU Dortmund University (2002).

[37] A. Jankowiak, *Strahldiagnose und Closed-Orbit-Charakterisierung mit HF-Strahllagemonitoren am Beispiel der Synchrotronstrahlungsquelle DELTA*, Dissertation, TU Dortmund University (1999).

[38] P. Hartmann, DELTA, TU Dortmund University, private communication (2020).

[39] Bergoz Instrumentation, France, *Multiplexed Beam Position Monitor User's Manual*, Rev. 1.5.4 (1998).

[40] esd-electronics system design GmbH, Germany, *CAN-CAI812 Hardware-Handbuch*, CAN-CAI812 Hardware Rev. 2.0 (1993).

[41] Instrumentation Technologies, Slovenia, *Libera Electron User Manual*, 3rd ed. (1998).

[42] A. Kosicek, *Libera Electron Beam Position Processor*, Proc. 21st Particle Accelerator Conference, Knoxville, USA, pp. 4284–4286 (2005).

[43] P. Hartmann et al., *Kicker Based Tune Measurement for DELTA*, Proc. 8th European Workshop on Beam Diagnostics and Instrumentation for Particle Accelerators, Venice, Italy, pp. 277–279 (2007).

[44] G. Blokesch, M. Negrazus, and K. Wille, *A slotted-pipe kicker for high-current storage rings*, Nucl. Instrum. Methods in Physics Research A 338, pp. 151–155 (1994).

[45] R. W. Cottle and Mukund N. Thapa, *Linear and Nonlinear Optimization*, Springer Nature (2017).

[46] P. Hartmann et al., *Fast Orbit Feedback for DELTA*, Proc. 11st International Workshop on Personal Computers and Particle Accelerator Controls, Campinas, Brazil, pp. 123–125 (2016).

[47] M. Grewe et al., *SVD Based Orbit Correction Including Corrector Limitations at DELTA*, Proc. 9th European Particle Accelerator Conference, Lucerne, Switzerland, pp. 2568–2570 (2004).

[48] D. Schirmer, *Orbit Correction with Machine Learning Techniques at the Sychrotron Light Source DELTA*, Proc. 17th International Conference on Accelerator and Large Experimental Physics Control Systems, New York, USA, pp. 1426–1430 (2019).

[49] L. Farvacque, *Automated Beam Position Control in the ESRF Storage Ring*, Proc. Workshop on Automated Beam Steering and Shaping, Geneva, Switzerland (1998).

[50] S. Kötter, *Introducing two Energy-Correction Schemes at DELTA*, Proc. 12th International Particle Accelerator Conference, Campinas, Brazil, pp. 740–743 (2021).

[51] S. Kötter et al., *Evaluation of an Interior Point Method Specialized in Solving Constrained Convex Optimization Problems for Orbit Correction at the Electron Storage Ring at DELTA*, Proc. 9th International Particle Accelerator Conference, Vancouver, Canada, pp. 3507–3509 (2018).

[52] B. Büsing et al., *Optics Studies on the Operation of a New Wiggler and Bunch Shortening at DELTA Storage Ring*, Proc. 12th International Particle Accelerator Conference, Campinas, Brazil, pp. 2772–2774 (2021).

[53] D. Schirmer and A. Althaus, *Integration of a Model Server into the Control System of the Sychrotron Light Source DELTA*, Proc. 17th International Conference on Accelerator and Large Experimental Physics Control Systems, New York, USA, pp. 1421–1425 (2019).

[54] I. Agapov et al., *OCELOT: A software framework for synchrotron light source and FEL studies*, Nucl. Instrum. Methods in Physics Research A 768, pp. 151–156 (2014).

[55] R. Molo, *Towards Echo-Enabled Harmonic Generation at FLASH1 and DELTA*, Dissertation, TU Dortmund University (2017).

[56] S. Hilbrich, *Studies of the DELTA Lattice in View of a Future Short-Pulse Facility based on Echo-Enabled Harmonic Generation*, master's thesis, TU Dortmund University (2015).

[57] B. Riemann et al., *COBEA - Optical Parameters from Response Matrices without Knowledge of Magnet Strengths*, Proc. 8th International Particle Accelerator Conference, Copenhagen, Denmark, pp. 676–679 (2017).

[58] J. Safranek, *Experimental determination of storage ring optics using orbit response measurements*, Nucl. Instrum. Methods in Physics Research A 388, pp. 27–36 (1997).

[59] B. Riemann et al., *Validating the COBEA Algorithm at the DELTA Storage Ring*, Proc. 9th International Particle Accelerator Conference, Vancouver, Canada, pp. 4851–4854 (2018).

[60] S. Kötter, B. Riemann, and T. Weis, *Status of the Development of a BE-Model-Based Program for Orbit Correction at the Electron Storage Ring DELTA*, Proc. 8th International Particle Accelerator Conference, Copenhagen, Denmark, pp. 673–675 (2017).

[61] S. Kötter and T. Weis, *Towards an Adaptive Orbit-Response-Matrix Model for Twiss-Parameter Diagnostics and Orbit Correction at DELTA*, Proc. 8th International Beam Instrumentation Conference, Malmö, Sweden, pp. 485–489 (2019).

[62] S. Kötter, *Analytical Description of the Steerer Parameters in the Bilinear-Exponential Model at DELTA*, Proc. 12th International Particle Accelerator Conference, Campinas, Brazil, pp. 737–739 (2021).

[63] D. A. Edwards and L. C. Teng, *Parametrization of Linear Coupled Motion in Periodic Systems*, IEEE Transactions on Nuclear Science 20, pp. 885–888 (1973).

[64] H. Mais and G. Ripken, *Theory of Coupled Synchro-Betatron Oscillations*, DESY Int. Rep. 5, Deutsches Elektronen-Synchrotron (1982).

[65] V. A. Lebedev and S. A. Bogacz, *Betatron motion with coupling of horizontal and vertical degrees of freedom*, Journal of Instrumentation 5, pp. 1–24 in P10010 (2010).

[66] H. Wiedemann, *Particle Accelerator Physics*, Springer (2007).

[67] V. Ziemann, *Response matrices in strongly coupled storage rings with a radio-frequency system constraining the revolution time*, Phys. Rev. ST Accel. Beams 18, pp. 1–4 in 054001 (2014).

[68] W. J. Corbett et al., *Debugging Real Accelerators*, Particle Accelerators 58, pp. 193–200 (1997).

[69] I. N. Bronstein, K. A. Semendyayev, G. Musiol, and H. Mühlig, *Handbook of Mathematics*, Spinger (2015).

[70] A. G. Akritas and G. I. Malaschonok, *Applications of singular-value decomposition (SVD)*, Mathematics and Computers in Simulation 67, pp. 15–31 (2004).

[71] S. L. Campbell, *Generalized Inverses of Linear Transformations*, Society for Industrial and Applied Mathematics, Philadelphia (1979).

[72] B. Autin and Y. Marti, *Closed Orbit Correction of A.G. Machines Using a Small Number of Magnets*, CERN Int. Rep., European Organization for Nuclear Research (1973).

[73] S. Sra, S. Nowozin, and S. J. Wright, *Optimization for Machine Learning*, MIT Press (2011).

[74] M. S. Lobo et al., *Applications of second-order cone programming*, Linear Algebra and its Applications 284, pp. 193–228 (1998).

[75] A. Ben-Tal and A. Nemirovski, *Lectures on Modern Convex Optimization: Analysis, Algorithms, Engineering Applications*, Society for Industrial and Applied Mathematics & Mathematical Programming Society, Philadelphia (2001).

[76] M. S. Andersen, J. Dahl, and L. Vandenberghe, *CVXOPT: A Python Package for Convex Optimization*, URL: `www.cvxopt.org` [accessed: 2022].

[77] L. Vandenberghe, *The CVXOPT linear and quadratic cone program solvers*, CVXOPT ver. 1.2.2 (2010).

[78] G. Schmidt, DELTA, TU Dortmund University, private communication (2022).

[79] A. Zupanc et al., *Orbit Correction with Frequency in Java*, Proc. 4th International Workshop on Personal Computers and Particle Accelerator Controls, Frascati, Italy (2002).

[80] R. Müller, Helmholtz-Zentrum Berlin, private communication (2021).

[81] S. Marsching et al., *Commissioning of a new Beam-Position Monitoring System at ANKA*, Proc. 3rd International Particle Accelerator Conference, New Orleans, USA, pp. 825–827 (2012).

[82] D. Einfeld et al., *Commissioning of the ANKA Storage Ring*, Proc. 7th European Particle Accelerator Conference, Vienna, Austria, pp. 277–279 (2000).

[83] European Laboratory for Particle Physics, *The MAD-X Program*, Version 5.08.00 (2022).

[84] K. Fuchsberger and Y. I. Levinsen, *PyMad - Integration of MADX in Python*, Proc. 2nd International Particle Accelerator Conference, San Sebastian, Spain, pp. 2289–2291 (2011).

[85] M. Borland (Advanced Photon Source), *User's Manual for elegant*, Program Version 2021.4 (2021).

[86] É. Forest, F. Schmidt, and E. McIntosh, *Introduction to the Polymorphic Tracking Code*, CERN Int. Rep., European Organization for Nuclear Research (2002).

[87] A. Ropert, *Beam Position Stability at the ESRF*, Proc. Orbit Correction and Analysis in Circular Accelerators Workshop, New York, USA, pp. 69–76 (1994).

[88] M. Böge et al., *Fast closed orbit control in the SLS storage ring*, Proc. 18th Particle Accelerator Conference, New York, USA, pp. 1129–1131 (1999).

[89] K. Balewski, *Comissioning of PETRA III*, Proc. 1st International Particle Accelerator Conference, Kyoto, Japan, pp. 1280–1284 (2010).

[90] R. H. Byrd, L. Peihuang, and J. Nocedal, *A Limited-Memory Algorithm for Bound-Constrained Optimization*, MCS–P404-1293, Argonne National Laboratory (1996).

[91] P. Virtanen et al., *SciPy 1.0: fundamental algorithms for scientific computing in Python*, Nature Methods 17, pp. 261–272 (2020).

[92] D. Kingma and J. Ba, *Adam: A Method for Stochastic Optimization*, Proc. 3rd International Conference on Learning Representations, San Diego, USA, pp. 1–15 in arXiv:1412.6980 (2015).

[93] M. Abadi et al., *TensorFlow: Large-Scale Machine Learning on Heterogeneous Systems*, URL: www.tensorflow.org [accessed: 2022].

[94] F. Schmidt, *MAD-X PTC Integration*, Proc. 21st Particle Accelerator Conference, Knoxville, USA, pp. 1272–1774 (2005).

[95] B. Büsing, DELTA, TU Dortmund University, private communication (2022).

[96] D. Schirmer, DELTA, TU Dortmund University, private communication (2022).

[97] A. W. Chao, K. H. Mess, M. Tigner, and F. Zimmermann, *Handbook of Accelerator Physics and Egineering*, World Scientific Publishing (2013).

15 ACKNOWLEDGEMENTS

First of all, I express my gratitude to Prof. Dr. Thomas Weis (†2021) for accepting me as his doctoral student and his continuous support even when he fell ill. May he rest in peace.

Secondly, I am grateful to Prof. Dr. Shaukat Khan for accepting me into his work group and reviewing this work when Mr. Weis could not do so anymore. He treated me as his own doctoral student. I also thank Prof. Dr. Andreas Jankowiak who became the second reviewer.

My former colleague Bernard Riemann helped me through many dark times by showing interest in my work when few others would. Apart from that, he was my go-to knowledge source for all beam dynamics questions and proof-read parts of this work. I will be forever thankful to him.

Carsten Mai made me acquainted with the social aspects of science: the workshops and visits to other facilities as well as the community behind it all. He also had my back at DELTA. I am grateful to him for both.

Tanja Shulte-Eickhoff and I had many great conversations about literally anything. She also listened to me when I was depressed. For this, and her help in survey questions, I thank her deeply.

I am thankful to Dr. Detlev Schirmer for the interesting orbit correction discussions we had and for proof-reading the first chapters of this work.

I also thank my former colleagues Benedikt Büsing, André Althaus, Dennis Rohde, Benjamin Isbarn and Arjun Radha Krishnan. "Optics Consulting Büsing" was a great source of optics knowledge and provided me with some tricks as to how to operate DELTA. André, Dennis and Benjamin supported me with their computer knowledge time and time again throughout the years. Arjun and I just had some great home-cooked dinners while I wrote this dissertation during the COVID19 pandemic. Thank you for the company!

In addition to that, I express my gratitude to all the other scientists and technicians at DELTA who helped and supported me in various ways throughout my dissertation.

Last but not least, I am grateful to my mother and my father. Without them, this work would not have been possible. My mother supported me emotionally and financially throughout my life. My father (†1997), a physicist and also radiologist, sowed and then fueled my interest in science long ago. Thank you both! Rest in peace, Dad.